DISCONTINUOUS PRECIPITATION IN COPPER COBALT ALLOYS

By

ALEKSANDRA PEROVIC, B.Sc.,M.Sc.

A Thesis

Submitted to the School of Graduate Studies

in Partial Fulfilment of the Requirements

for the Degree

Doctor of Philosophy

McMaster University

March 1979

DISCONTINUOUS PRECIPITATION IN COPPER COBALT ALLOYS

Dedicated to my Mother

DOCTOR OF PHILOSOPHY
(Metallurgy and Materials Science)

McMASTER UNIVERSITY
Hamilton, Ontario

TITLE: Discontinuous precipitation in Copper Cobalt Alloys

AUTHOR: Aleksandra Perovic, B.Sc. (University of Belgrade, Yugoslavia)

M.Sc. (University of Belgrade, Yugoslavia)

SUPERVISOR: Professor G. R. Purdy

NUMBER OF PAGES: xviii, 171

ABSTRACT

This thesis is concerned with the cooperative growth problem of the discontinuous precipitation reaction of rod-like particles and their subsequent spheroidization into rows. Previous theories are examined, and the details of a model for the transformation, which assumes the existence of local equilibrium between the product phases, are derived. The steady state diffusion equation is solved under the assumption of boundary diffusion controlled growth in the case of rod symmetry. The available kinetic data and auxiliary information are used to test the model. The results are consistent with the premise that a boundary friction term determines the rate of interface migration. The electron microscopy is used to determine the precipitate morphology and their size and distribution. The results are interpreted in the light of existing knowledge and concepts especially developed for the purpose of this investigation.

ACKNOWLEDGEMENTS

I am indebted to my supervisor, Dr. G. R. Purdy for suggesting the topic of research treated here and for his continuing guidance, help and encouragement throughout the course of this work. It is a pleasure to express my sincere gratitude to Dr. J. S. Kirkaldy and Dr. J. D. Embury for their advice and stimulating conversations throughout the duration of this program; to Dr. J. A. Morrison for serving on my Ph.D. Committee and Dr. Z. V. Kovarik for helpful discussions.

I am also grateful to Mrs. H. Kennelly for rapidly and accurately typing this thesis and to Mr. T. Bryner for his work on the photographs.

Thanks are also extended to many of the faculty, technical staff and graduate students.

The financial support of the National Research Council of Canada is gratefully acknowledged.

TABLE OF CONTENTS

LIST OF TABLES

FIGURE CAPTIONS

INTRODUCTION AND SCOPE

This work was undertaken to elucidate the mechanism of formation of columnar arrays of the fine Co particles found in certain Cu-Co alloys.

The row morphology characteristic of these alloys will be explained in terms of the spheroidization of previously formed rod-like particles. The cause of the discontinuous reaction in this system will be explored in the light of an analysis of the various driving forces acting on the reaction front.

The present work is thus intended to contribute to our experimental and theoretical knowledge of discontinuous precipitation reactions.

CHAPTER 1

LITERATURE SURVEY

1.1 Row Precipitation

Precipitate arrays believed to be associated with moving interfaces have been reported in certain alloy steel systems[1-7], in aluminum-copper alloys[8], in silicon-copper alloys[9], in aluminum-zirconium alloys[10-13], as well as in niobium-containing austenitic stainless steel[14,15]. In addition aligned cobalt particles have been observed in some copper-cobalt alloys[16,17] and these arrays resemble to some extent those formed in the systems noted above.

The periodic arrays of alloy carbide precipitates found in low alloy steels have been associated with facetted interfaces joining austenite and ferrite of special orientation relationships[18,19]. This is usually referred to as interphase precipitation. Figure 1 shows the interphase precipitates of CrC phase while Figure 2 is a schematic representation of the mechanism of nucleation and growth of carbides on the γ/α interface. The reaction is explained in terms of precipitation on immobile facets, with subsequent overgrowth by mobile steps. Aaronson[20] has proposed that the growth of ferrite from a parent austenite grain often occurs by the lateral movement of small ledges or steps along the

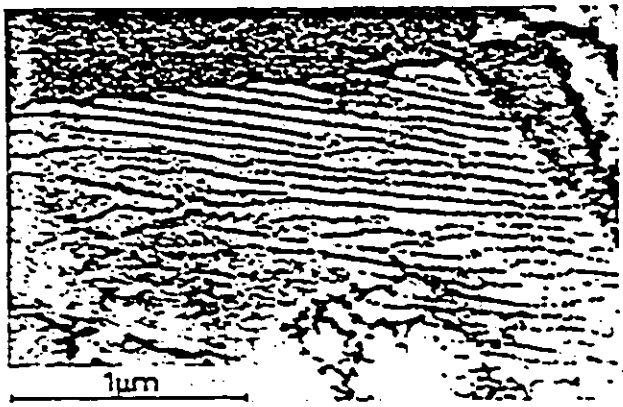

Figure 1. Interphase precipitates in alloy steels, after Campbell and Honeycombe[3].

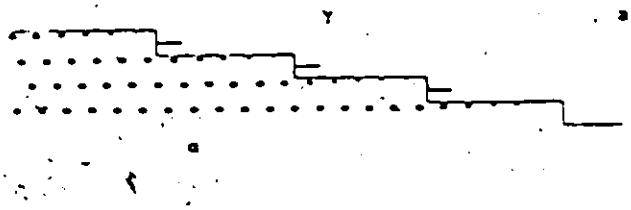

Figure 2. Schematic representation of the mechanism of nucleation and growth of interphase precipitates after Honeycombe[6].

coherent faces, the steps being short lengths of incoherent boundary. It is believed that the ferrite interfaces associated with interphase precipitation grow predominantly by ledge migration in such a way that nucleation occurs at the planar boundary while the ledge itself is free from precipitate.

The repeated precipitation of NbC particles in stainless steels[14,15] and of copper particles in a silicon matrix[9] has been explained in terms of dislocation climb due to a local vacancy depletion or supersaturation created by precipitate growth while, in the case of θ' in the Al-Cu alloys[8], the driving force for dislocation climb is approximately independent of the precipitation process and is due to a supersaturation of quenched-in vacancies. The sketches in Figure 3 outline the principle of the repeated nucleation model on a climbing dislocation, while Figure 4 represents the observed θ' colony microstructure. The mechanism of repeated precipitation on the climbing dislocations is explained as a consequence of heterogeneous nucleation in the stress fields of the moving dislocations during quenching. The dislocation climb rate is slow enough to permit nucleation, but sufficiently rapid to avoid pinning by the newly-formed precipitates. The precipitates grow by a subsequent volume diffusional process. (The line tension forces oppose colony growth).

There is a further possibility that solute transport along the moving dislocation contributes to precipitate growth

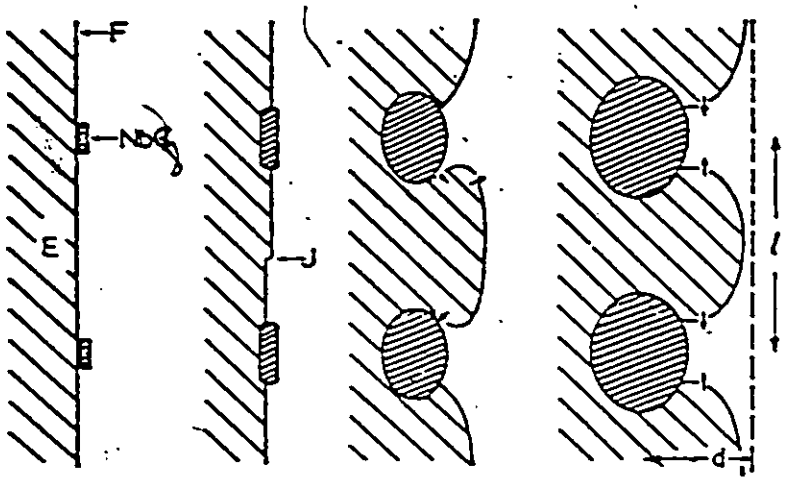

Figure 3. Model for repeated nucleation of particles or a climbing dislocation after Nes and Washburn[9].

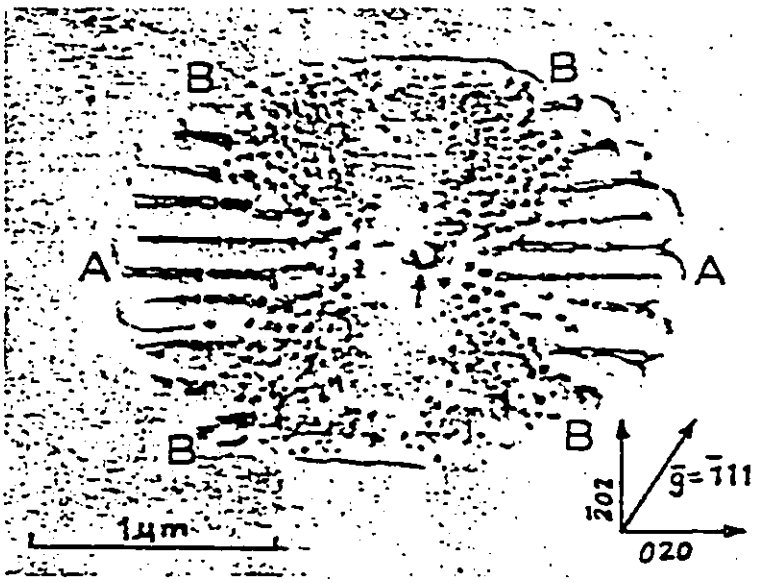

Figure 4. Observed θ' and colony microstructure, after Headley and Hren[8].

and increases the velocity of the sweeping dislocation through a thermodynamic force resulting from a free energy step at the dislocation, but this has not been explored or even articulated in the literature.

The presence of columnar arrays of Co spherical particles in Cu-Co alloys has been reported by Kreye and Hornbogen[16], who suggest (in a figure caption) that the columns form as "coagulations" of rods. Figure 5 shows their result. This suggestion, here interpreted as the Rayleigh instability of rods formed by cellular precipitation, will be expanded and critically analyzed in subsequent chapters. At this point Figure 6 is given to represent schematically the consequence of rod instability. Phillips[17] attempted to explain the same structure by precipitation on dislocations emitted from the grain boundary during quenching. He encountered difficulties because the particles were not lined up along intersections of common slip planes. He further ruled out spinoidal decomposition since directions other than <100> were observed.

1.2 Discontinuous precipitation

Discontinuous (known also as "cellular") precipitation[21] is a solid-state phase transformation resulting in a decomposition of a supersaturated phase, α_0, into a structurally identical phase, α, that is partially depleted of solute, and a new phase, β. The adjective "discontinuous" refers to the composition of the matrix lattice, which may change discontinuous-

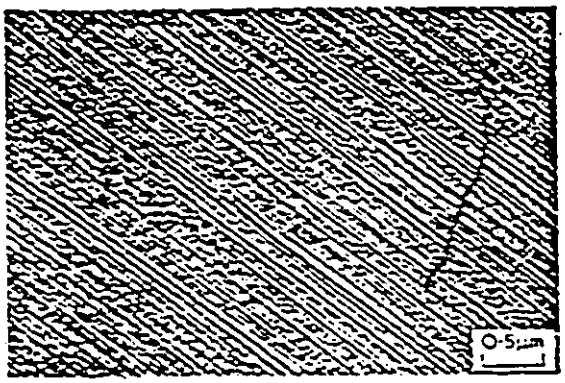

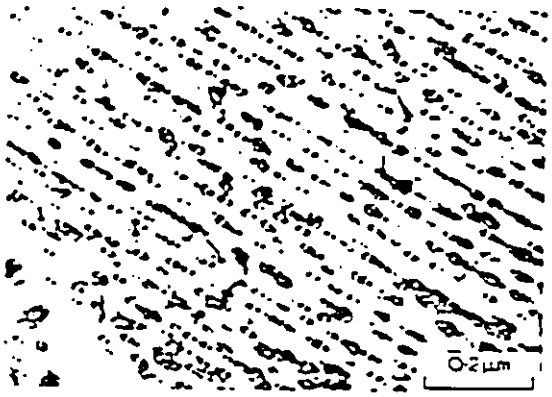

Figure 5. Columnar arrays of Co spherical particles in Cu-Co alloys, after Kreye and Hornbogen[6].

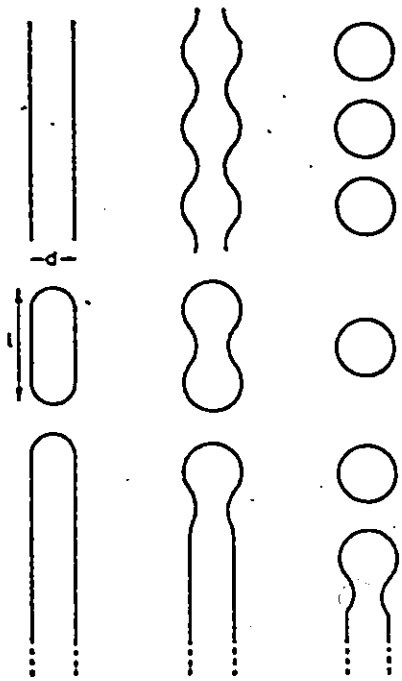

Figure 6. Schematic representation of various modes of spheroidization of cylindrical particles after McLean[62].

ly across the reaction front dividing the supersaturated phase from its depleted counterpart. The terms recrystallization and grain boundary reaction have also been used and relate to other typical features of this reaction: it leads to the formation of lamellar or rod morphologies with an associated change in matrix orientation which occurs at the moving grain boundary.

The process usually results in the formation of an equilibrium precipitate, either incoherent or semicoherent with the matrix, sometimes exhibiting a single crystallographic orientation relation. A supersaturated solution may decompose directly to a cellular precipitate, but more often cellular precipitation follows the formation of metastable precipitates generally distributed within the parent solution.

Although not as common as "continuous" precipitation, cellular precipitation phenomena are not at all rare and have been studied in numerous alloy systems, including some of considerable commercial importance. As with all precipitation processes, the effect of cellular precipitation on mechanical, physical, and chemical properties is usually very marked.

The main problems of interest in this mode of transformation are:

i) How does the initiation of discontinuous precipitation occur?

ii) What is the mechanism of the growth?

iii) What (generalized) forces act on the reaction front?

iv) What are the criteria for determining which systems will exhibit the cellular mode of precipitation?

There are further problems concerning the spacing - approximately constant for a given set of growth conditions - as well as the mechanism of multiplication of lamellae or rods to keep the spacing constant.

There have been many attempts to answer these questions, although at present there is no consensus as to the correct answer.

a) Initation of cellular reaction

The initiation of the cellular reaction is closely related to the nucleation process itself. When a heterogeneous nucleation process is considered, it is usually assumed that the heterogeneity (such as the grain boundary) is stationary. After nucleation, the kinetic process must follow the formation of the heterogeneously formed nuclei, i.e. the grain boundary must start moving. But how a stationary grain boundary begins to move depends on its interaction with its precipitates. Tu and Turnbull[22] propose that the driving force for initial grain boundary movement arises from the difference between the surface energies of the interfaces of a precipitated particle to the two matrix grains. This interfacial energy difference is caused by the morphology of the grain boundary precipitate which, in the Sb-Sn system, is disc-like in shape and exhibits fixed crystallographic orientation and habit relationships with the matrix.

Aaronson and Aaron[23] extended these concepts to include other morphologies and emphasized the importance of formation of the minimum energy nucleus shape assuming that an energy cusp facet appears at only one orientation of the interphase boundary. They proposed that the initial driving force was due to balancing of the interfacial energies at the three phase junctions among the grain boundary and the semicoherent and disordered areas of an interphase boundary. Based upon these considerations, it was noted that under certain circumstances the grain boundary was forced to bow toward the nuclei it joins favouring the formation of grain boundary allotriomorphs. Bowing of the boundary away from the nuclei, on the other hand, was reasoned to favour the cellular reaction. Both deductions are based on the view that the requirement of continuity between neighbouring junctions produces a departure of the grain boundary dihedral angle at these junctions, sufficiently far from its equilibrium value so that a driving force is provided for breakaway from the junctions. These results apply, however, only when the facet energy is greater than half of a disordered grain boundary.

In the above treatments, the initiation of discontinuous precipitation is the consequence of the interaction of the stationary grain boundary with precipitates in their early stage of formation i.e. in the nucleation stage.

Fournelle and Clark[24] propose that the grain boundary motion is due to the surface tension forces responsible for ordinary grain growth. The discontinuous precipitates form from

initially unoccupied grain boundaries by the boundary bowing out between simultaneously forming allotriomorphs. As the boundary bows, it depletes the region behind it of solute by solute partitioning in the advance α/α_0 interface. Crystallographic relationships between initial allotriomorphs and adjacent grains would then have a minimal influence on cellular structure.

Meyrick[25] proposed that, for alloys in which the solute tends to segregate at grain boundaries, thereby reducing the grain boundary energy, a dimunition in the segregated population due to precipitation can provide an initial driving force for the boundary to migrate.

Lange and Purdy[26] considered a special case where extensive fine scale grain boundary precipitation preceded cellular precipitation and attributed the initial grain boundary displacement to the interaction of the boundary with coarsening precipitates. Their observations showed that the cellular precipitation reaction in Fe-Zn alloys is preceded by the nucleation, growth, and coarsening of a grain boundary phase. The coarsening process itself was thought to cause the displacements of the grain boundary through the abrupt release of portions of the grain boundary into regions of large and increasing supersaturation.

b) Nucleation and multiplication of lammellae

The nucleation process of discontinuous precipitation is still the subject of controversy, i.e.: Is there a single

nucleus which propagates by branching or are there several nuclei of each phase at the grain boundary which grow together to give a cooperative cellular morphology?

Two types of mechanism, branching and independent nucleation, have been proposed for the multiplication of lamellae. Hillert[27] has shown that the morphology of pearlite can be explained by a branching mechanism and he demonstrated conclusively that the carbide in the pearlitic structure was completely interconnected. However, in the cellular reactions, the orientations and habit relations appear in some cases to be more closely adhered to than in the pearlite transformation. For this reason, branching may be more difficult in the cellular than in the pearlite transformation.

In the cellular reaction, a mechanism for independent nucleation of lamellae is based on the proposed mechanism for the initiation of the reaction by Tu and Turnbull[22]. Whenever the local interlamellar spacing becomes sufficiently large, a recess develops, providing an ideal site for the nucleation of a new β lamella by virtue of a set of planes that produces a particularly low α-β interfacial free energy. Sundquist[28] gave a quantitative theory of recess development. In addition, this author believes that the same basic nucleation mechanism is probably operative in pearlite reactions also, although the physics of recess development is somewhat different.

In those systems not exhibiting definite crystallographic relationships with the matrix, branching of the lamellae has

been observed, as well as independent nucleation[29,30].

After reviewing the basic phenomenology of cellular precipitation initiation, we will turn to the steady-state growth problem.

c) The growth theories of cellular precipitation

A number of theories for growth of cellular precipitates have been developed in the past; most notably by Turnbull[31], Cahn[32], Hillert[33,34], Shapiro and Kirkaldy[35], Sulonen[36], and Sundquist[28]. All these theories deal with the forces acting on the moving grain boundary during cellular precipitation thereby determining grain boundary shape and velocity at any given value of interlamellar spacing. Hence, the basic problem in cellular precipitation reaction is that of evaluating the forces acting on the α-α_0 grain boundary under the conditions present during reaction. Hillert and Lagneborg[37] have noted that at least four possible origins for driving forces for the grain boundary migration exist in the literature:

i) Plastic deformation causes grain boundary migration if the temperature is sufficiently high and results in recrystallization[38].

ii) A particle that nucleates at a grain boundary may often have a close orientation relationship to one of the two matrix grains and the surface energies may then favour the growth of this grain in contact with the particle[39].

iii) The concentration gradient in a depleted zone gives rise to coherency stresses if the lattice parameter varies with the alloy content. This may provide a driving force for the migration of a boundary into the stressed region[36].

iv) A driving force may be supplied thermodynamically if the grain boundary migration is sufficiently rapid to make the concentration profile so steep that there is a deviation from local equilibrium between the grain boundary material and the retracting grain.

This latter point has been explored in detail by Hillert[33,40], who maintains that the local driving force for grain boundary migration may be supplied thermodynamically. Turnbull[22] and Cahn[32] treated the growth process without considering the nature of the local force actually acting on the grain boundary. As a consequence, their treatments give no indication of why discontinuous precipitation occurs. Cahn[32] simply assumed that the grain boundary will move with a rate proportional to the available free energy, without considering by what mechanism part of this energy could be transformed into a force. Kirkaldy[41] and Shapiro[42] developed the suggestion that there is a chemical driving force acting on the growth of both new phases provided by the existence of a metastable miscibility gap so that the reaction can be treated as an eutectoid (monotectoid) transformation. However, suitable miscibility gaps may not exist in all cases.

Sulonen[36] introduced the idea of formation of coherency stresses in front of the interface which gives rise to a driving force for interface migration. The grain boundary precipitates initially are formed at the grain boundary and as they grow a zone, impoverished in solute, is formed ahead of the solid solution/cell interface as a result of rapid grain boundary diffusion acting in combination with volume diffusion. This zone, the thickness of which may vary from some interatomic distances upwards, is subjected to tensile or compressive lattice misfit stresses depending on the sign of change of lattice dimensions in the formation of the zone. It is the lattice strain energy that gives rise to the driving force of the interface migration in discontinuous precipitation because there is no counterpart in the form of strain energy term in the growing grain.

Cahn[32] developed a description of diffusion during cellular reaction on the assumptions that lattice diffusion is negligible compared with grain boundary diffusion so that the cell cannot segregate to equilibrium composition for any non-zero growth rate. With the above assumption, and approximating the shape of the boundary as planar, Cahn found the steady-state solution for the moving grain boundary diffusion equation of the form:

$$D_b \delta \frac{d^2 C_b}{dz^2} + v(C_o - C_p) = 0, \qquad (1)$$

to be:

$$\frac{C-C_0}{C_1-C_0} = \frac{\cosh\, z\,\sqrt{A}/S}{\cosh\sqrt{A}/2}\,, \qquad (2)$$

where $A = vS^2/KD_b\cdot\delta$, C_0 is the solute content of the parent grain, and $C_1 \equiv C_p$ is the solute content of the growing lamella at its sides, z is the coordinate in the direction of diffusion in the boundary, S is the width of the lamella, v is the velocity of the boundary, K is the equilibrium distribution coefficient of the solute between the boundary and the growing grain, D_b is the diffusivity and δ is the width of the boundary.

Several attempts have been made to extend Cahn's treatment in order to take into account the non-planar shape of the boundary and the effect of capillarity.

Hillert[43] used the following equation for the forces acting on the grain boundary:

$$\frac{\gamma}{\rho} = \frac{\Delta G_m}{V_m} - \frac{v}{M}\,, \qquad (3)$$

so that the radius of curvature, ρ at any point on the advancing interface is such that all the forces balance one other, and γ is the specific surface free energy of a grain boundary. By knowing the composition along the interface and neglecting the term v/M, the shape of the advancing front was calculated by using the relation between ρ and the shape of lamella in the form:

$$\frac{1}{\rho} = - \frac{d^2y}{dz^2} \Big/ \left[1 + \left(\frac{dy}{dz}\right)^2\right]^{3/2} , \qquad (4)$$

where y is the coordinate in the growth direction of lamella and z is the coordinate parallel to the advancing interface. Figure 7 shows the result for discontinuous reactions. It should be noted that the interface shape determined in this way is rather flat, thus justifying the assumption used in deriving the concentration profile.

The most detailed treatment of the interface shape has been presented by Sundquist[28] and is based upon two equations. Using ℓ as a measure of the distance along the curved boundary, Sundquist formulated the following equation for the boundary diffusion:

$$KD_b\delta \cdot dc/d\ell = \int_{\ell}^{L} v(c_0 - c)\, d\ell , \qquad (5)$$

where L is the value of ℓ in the middle of the specimen and v is the migration rate of the boundary in the direction of the normal. The balance of forces at the boundary yields the second equation:

$$\Delta G_m = \frac{vV_m}{M} - \gamma V_m \frac{d\theta}{d\ell} \qquad (6)$$

where θ is the angle between the macroscopic growth direction and the local normal of the boundary. The last term is due to capillarity and it has a decisive influence in the case of discontinuous precipitation, as can be seen from Figure 8 in

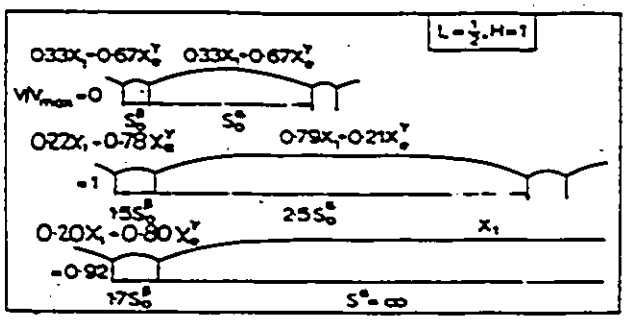

Figure 7. Shape of interface of discontinuous precipitation as a function of spacing and growth rate, after Hillert[33].

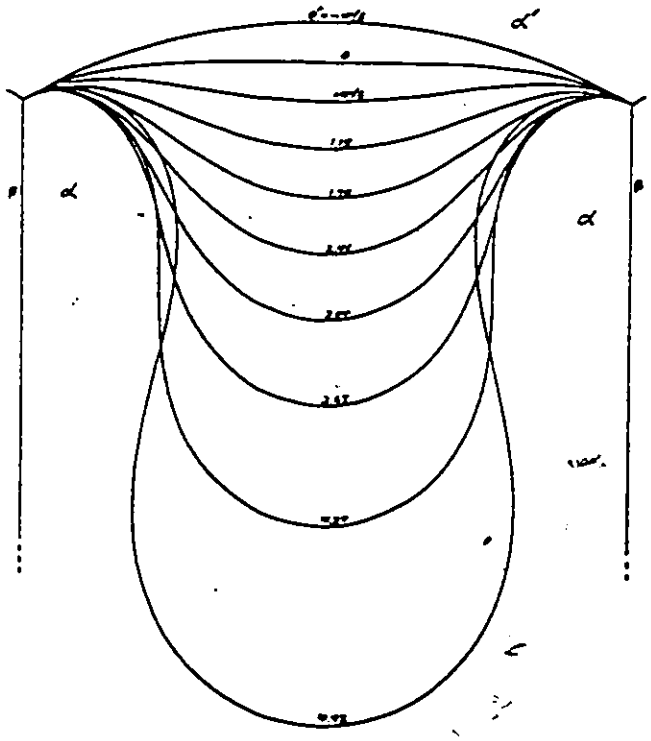

Figure 8. Computed grain boundaries shapes for various values of capillarity factor, $d\theta/d\ell$, after Sundquist[28].

which the computed shapes of the grain boundary are plotted for various values of $d\theta/d\ell$.

Hillert[43] has recently reviewed the growth theories for the lamellar eutectoid transformations from a free energy point of view, considering that the total free energy available to drive the reaction is divided into several parts. He then applied a similar treatment to discontinuous precipitation assuming that the grain boundary material can be considered a separate phase with its own free energy curve, as represented in Figure 9. However, it should be noted that grain boundaries are non-equilibrium defects, and the equilibrium between a grain boundary and crystal is a constrained equilibrium. One must note that the equilibrium concentration in the boundary is determined by a parallel-tangent construction based on the composition of the matrix since it is assumed that the number of atoms in the boundary is constant. The driving free energy for the growth of the new α grain is identified with some fraction of the free energy which would be lost due to volume diffusion if certain mechanism did not interfere. Two mechanisms were considered, one depending upon the sluggishness of volume diffusion and the other depending upon coherency stresses in the parent grain. These will be discussed separately.

By assuming ideal or dilute solution behaviour, Hillert obtained a simplified formula for the total driving force for the complete reaction:

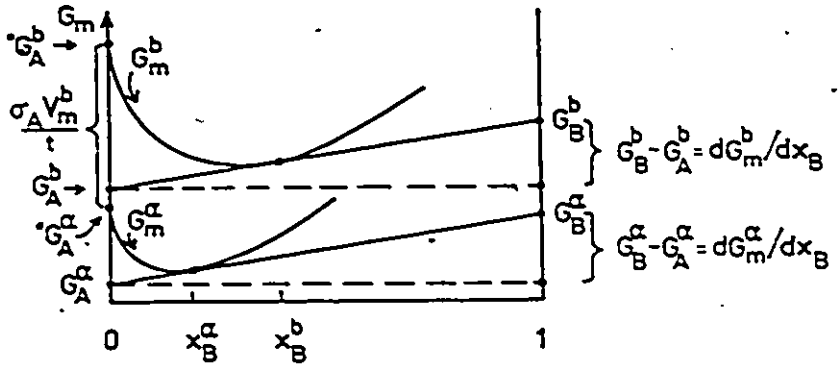

Figure 9. Free energy diagram showing the equilibrium between the boundary phase and the matrix, after Hillert[34].

$$\Delta G^{total} = \frac{RT}{V_m} \frac{(C_e - C_o)^2}{2C_o} \qquad (7)$$

as shown in Figure 10. The total free energy available in a transformation cannot, in general, be used to overcome the pressure difference at the curved surface but some free energy will be used to overcome friction and some free energy will be needed for diffusion. Hence, of the total free energy available for complete transformation, the quantity ΔG^{diff} is used up by the diffusion process as shown in Figure 11 and is estimated as:

$$\Delta G^{diff.} = \frac{RT}{V_m} \frac{(C_i - C_o)^2}{2C_o} . \qquad (8)$$

Regarding the grain boundary as a thin film of a special phase with a free energy curve such that equilibrium with a parent grain is established, Hillert used the pair of parallel tangents to construct the free-energy diagrams in the cases of the interface at rest (Figure 12) and slowly moving (Figure 13), with corresponding concentration profiles assuming chemical equilibrium to be established locally at each side of the boundary. The formation of concentration profiles in the parent phase ahead of an advancing interface gives rise to diffusion. The height of the concentration profiles in Figure 14 should be independent of the growth rate as long as there is a local equilibrium established at the interface. The free energy dissipation due to diffusion in the spike should also be independent of the growth rate and

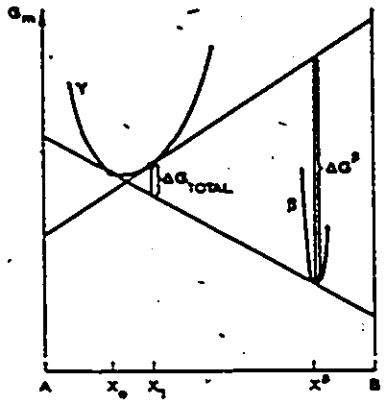

Figure 10. Free energy diagram for precipitation of β, after Hillert[33].

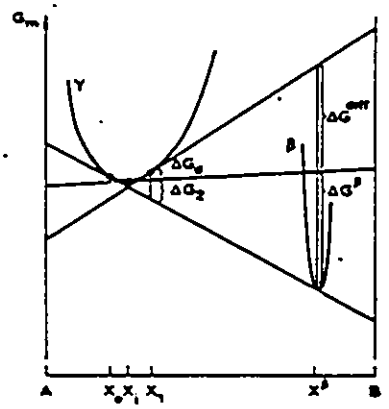

Figure 11. Free energy diagram for diffusion and precipitation of β, after Hillert[33].

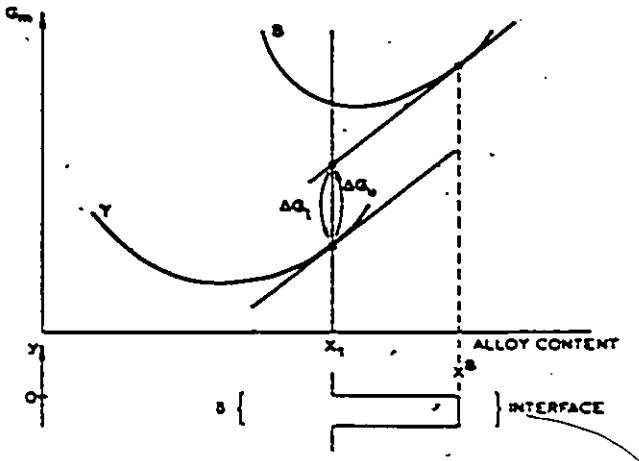

Figure 12. Free-energy diagram for interface at rest, after Hillert[33].

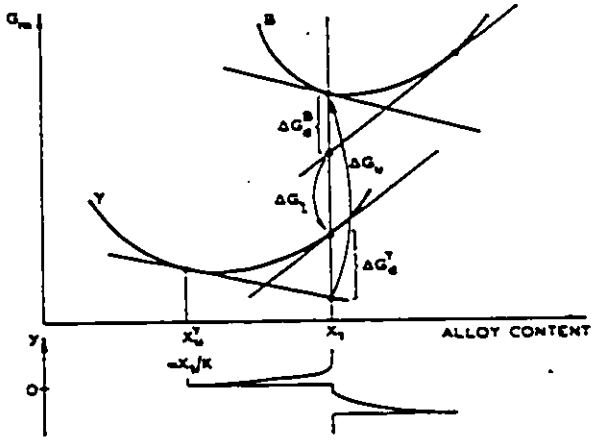

Figure 13. Free energy diagram for slowly moving boundary, after Hillert[33].

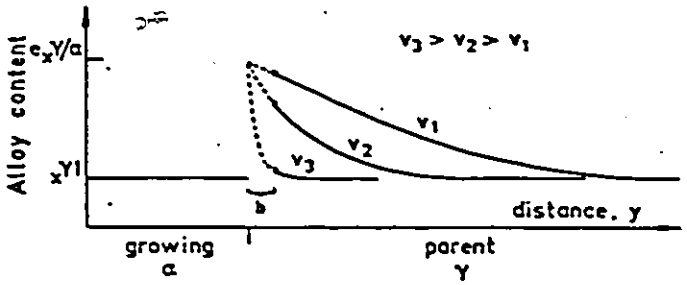

Figure 14. The formation of solute spike in the parent phase ahead of an advancing interface, after Hillert [40].

given by equation (7). The shape of the spike is described approximately by:

$$C-C_o = (C_e-C_o)\exp[-vy/D_v] \quad . \qquad (9)$$

However, at high velocities, the concentration profiles may become so narrow that they only exist mathematically. In that case, local equilibrium is no longer established at the interface. Hillert suggested treatment of such cases by simply assuming that the highest value actually existing in the spike is the value of some small atomic distance, b, from the interface. ($b \equiv \delta/4$, where δ is the width of the grain boundary.) The free energy diagram in such a case is shown in Figure 15. The effect on the free energy loss due to diffusion will be decreased by a factor $\exp(-vb/2D_v)$. As the diffusional loss of free energy decreases, there will be more driving force left to move the interface:

$$\Delta G = [\Delta G^{tot} - \Delta G^{diff}\exp(-vb/2D_v)V_m] \quad . \qquad (10)$$

Thus, a fraction of of ΔG^{diff} will not be spent on diffusion but give rise to a force($\equiv f\ \Delta G^{diff}/V_m$) which can be used to move the grain boundary in discontinuous precipitation, in those situations where volume diffusion is slow in comparison with the growth rate.

The possibility that coherency stresses give rise to a driving force for grain boundary movement has been suggested by Sulonen[36] and treated analytically by Hillert[43]. The

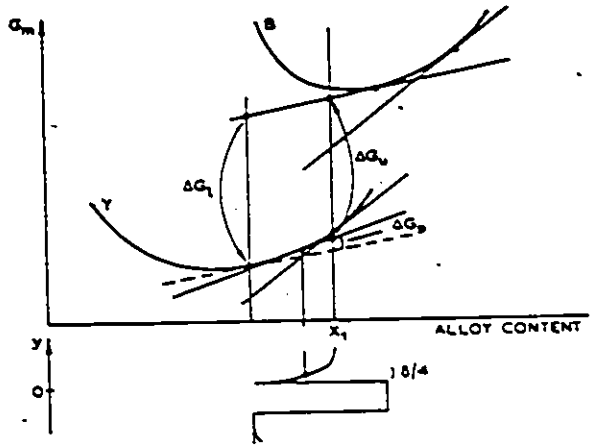

Figure 15. Free energy diagram for the grain boundary in discontinuous precipitation with deviation from local equilibrium, after Hillert[33].

composition of the coherent layer built up in front of the grain boundary due to a steep concentration gradient has been calculated by assuming local equilibrium between a grain boundary phase and a parent grain. The coherency stresses decrease the concentration differences within the parent grain and thus decrease the free energy loss due to volume diffusion and the difference will act as a driving force for the movement of the grain boundary (Figure 16). In Hillert's treatment, the driving free energy due to coherency stresses was not directly derived from elastic energy but was obtained directly through the effect of the coherent layer on the composition.

All theories of discontinuous precipitation assume the grain boundary diffusivity to be constant during the grain boundary motion. However, the structure and the structure-sensitive properties of moving solid-solid interfaces need not be the same as for their static counterparts. Indeed, a treatment due to Cahn[44] suggests that a variation of migration mechanism with driving force is generally to be expected.

Hillert and Purdy[45], in a recent publication, proved experimentally the existence of a chemical force, and showed that diffusivities for static and moving boundaries differ by about four orders of magnitude. These authors conclude that such a large discrepancy cannot be explained by errors in the experiments or evaluations but instead mean that properties of a grain boundary are quite different when it is stationary

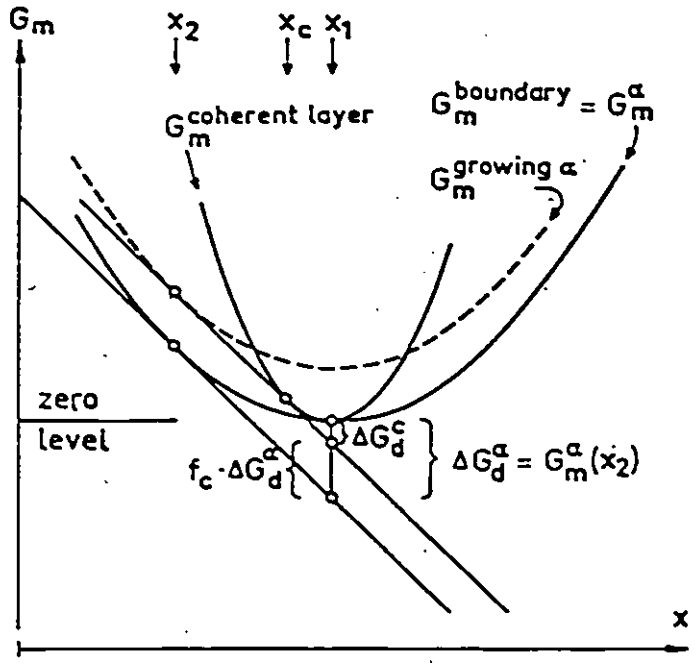

Figure 16. Free energy diagram illustrating the effect of coherency stresses in the parent grain on the driving force for boundary movement, after Hillert[43].

from when it is moving. A similar result was recently obtained by Smimoda et al[91].

1.3 Some Thermodynamic and Kinetic Aspects of Nucleation in Solids

a) Preamble

The cellular reaction starts at the imperfections, particularly at disordered grain boundaries where individual nuclei form and begin to grow synchronously in lamellar form led by the migrating grain boundary. The interaction of the grain boundary with its precipitates in the nucleation stage of the reaction is thought to be responsible in some systems for the start of movement of the grain boundary in the absence of plastic deformation and grain growth. The maintenance of the minimum energy nucleus shape under the assumption of local equilibrium of the interfacial forces at the junctions between the grain boundary and nucleus may lead to the grain boundary movement and development of cellular morphology.

b) Nucleation in solids

Russell[46] has recently reviewed nucleation in solids. All nucleation theories require that the critical nucleus shape be such as to minimize surface free energy since the critical nucleus is in unstable equilibrium with the matrix. The geometrical shape giving the minimum total surface energy for a particle of fixed volume is usually determined by the Gibbs-Wulff[47,48] construction. This construction, however, applies only to isolated particles and may not simply be used to de-

termine the equilibrium forms of particles located on interfaces or other structural singularities.

A formulation of surface thermodynamics recently developed by Cahn and Hoffman[49,50] presents a substantial contribution to the nucleation phenomenon, particularly regarding equilibrium at curved surfaces, equilibrium at intersections of planar surfaces, faceting of originally planar surfaces and equilibrium forms of particles on grain boundaries.

The treatment is in terms of a vector $\vec{\xi}$, defined by

$$\vec{\xi} = \vec{\nabla}(r\gamma), \qquad (11)$$

where r is the magnitude of the position vector, $r\vec{n}$, and $\vec{n}$ is the unit normal. The vector $\vec{\xi}$ has the property that its component normal to a physical surface is equal to γ and the off-normal component of $\vec{\xi}$ is a torque, which tends to rotate the surface into a lower energy orientation. The other property of the $\vec{\xi}$ vector is that, at each point along a line of intersection between three or more surfaces, the sum of $\vec{\xi}$ vectors for the surfaces involved must equal zero. This property, in some cases, also allows a very easy determination of the equilibrium form for particles which are located on planar interfaces and extend into the adjoining grains. This construction is illustrated in Figure 17. The equilibrium particle shape is geometrically similar to the region of $\vec{\xi}$-plot overlap.

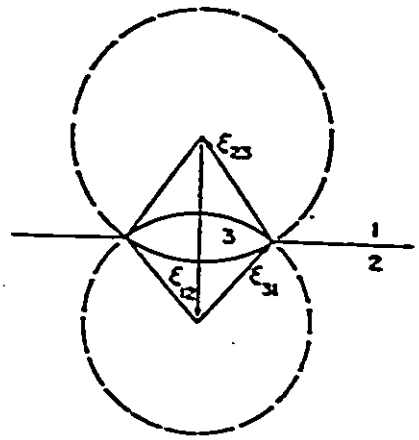

Figure 17. Illustration of the Gibbs-Wulff construction for the equilibrium form of a particle located on a grain boundary, after Cahn and Hoffman[50].

In another paper by Russell[51], the kinetics of heterogeneous nucleation is considered concerning the incubation times and frequency factors. It is concluded that the incubation time is proportional to the square of the critical nucleus volume divided by the frequency factor and the free energy of critical nucleus formation, and it is shown that an energetically favorable reaction possibly may not occur if another reaction with a smaller incubation time intervenes.

A procedure for determining the frequency factor and incubation time was recently developed using the principle of microscopic reversibility[52,53]. It consists of identifying the critical nucleus, inferring the mechanism of decay, and then calculating the rate with which atoms may leave the nucleus without so enriching the surroundings that the cluster becomes supercritical. This rate gives the frequency factor and permits calculation of the incubation time.

The frequency factor is found to be proportional to a boundary diffusivity, while the derived incubation times involved diffusivities, driving forces, surface tensions and contact angles, and followed the general relationship:

$$\tau \propto \frac{kT\, n_k^2}{\Delta G_k^o\, \beta_k} \quad . \qquad (12)$$

The existence of an incubation time is one reason why the reaction with the highest steady-state nucleation rate need not dominate, i.e. if two reactions are considered, $\beta \rightarrow \alpha$ and $\beta \rightarrow \gamma$, then:

$$\frac{J_\alpha(t)}{J_\gamma(t)} = \frac{J^s_\alpha}{J^s_\gamma} \exp\left(\frac{\tau_\gamma - \tau_\alpha}{t}\right) . \qquad (13)$$

Even in the case where J^s_α is greater than J^s_γ, it is still quite possible that nucleation of α could involve volume diffusion, while nucleation of γ involves only boundary diffusion; or formation of α might involve a much larger critical nucleus size. Both cases give a greater incubation time for nucleation of α.

1.4 Growth Kinetics in Precipitation Reactions

a) Preamble

Grain boundary precipitation is an important process during the discontinuous reaction in most systems exhibiting cellular morphology and during the formation of a sequence of precipitate phases in alloys undergoing aging reactions[54,55]. In considering nucleation at the grain boundary, the critical nucleus shape is assumed to be the equilibrium shape, which is normally a very good approximation. However, the growth morphology, which is controlled by kinetic considerations, will usually differ from the critical nucleus morphology.

b) Growth of grain boundary precipitates

The diffusion-controlled migration rate of an interface[56] is generally described by the equation:

$$v = - \frac{D_{eff.} \nabla C_n}{(C_\beta - C_\alpha)} , \qquad (14)$$

where ∇C_n is the concentration gradient normal to the interface and C_β and C_α are the equilibrium interface concentrations. The form of this equation depends on the solution of the appropriate diffusion equation with interface concentrations given by the local chemical equilibrium condition. Interface mobility, whatever its value, plays no part in determining this rate. The migration rate for a planar interface is given by a parabolic law:

$$v = \text{const.}\sqrt{\frac{D}{t}} \quad . \qquad (15)$$

Zener[59] published analytical and graphical solutions for planar and spherical growth from supersaturated solid solutions.

In discussion of specific growth forms, grain boundary allotriomorphs will be chosen.

Grain boundary allotriomorphs are precipitate crystals which have nucleated at, and grown preferentially along grain boundaries in the parent phase. Once nucleation has set the orientation relationship, the lengthening of the grain boundary precipitate proceeds by growth along the boundary and by concurrent thickening. The shape is now determined by kinetic, rather than equilibrium factors. The recent work of Aaron and Aaronson[58], and of Brailsford and Aaron[59] has demonstrated the important role of interface diffusion in the substitutional grain boundary precipitation reaction. These workers have

invoked a "collector plate" mechanism, in which solute diffuses to the grain boundary from the bulk parent phase, then along the grain boundary to the precipitate, and along the precipitate matrix interface (Figure 18). The rate-controlling process was taken to be the volume diffusion process and concentration of solute at the edge of the allotriomorph was given by the Gibbs-Thomson expression, as modified by Hillert[60], and the concentration of the solute in the grain boundary was taken everywhere the same on the assumption of very rapid grain boundary diffusion. It was concluded that the relative rates of grain-boundary, volume, and phase-boundary diffusion would determine the aspect ratio of such precipitates. A relatively low rate of phase boundary transport would favour the formation of fast-spreading thin films at the boundaries while volume diffusion would play a greater part in the thickening of such films. In a recent paper, Aaronson et al.[61], derived the growth kinetics of the thickening of the oblate ellipsoidal shape particle including the contribution of all existing interphase boundary diffusivities particularly appropriate in substitutional solutions. They concluded that the relative penetrations of particles precipitated at interphase boundaries into the phases forming these boundaries during growth will often lead to a particle morphology quite different from that obtained during nucleation.

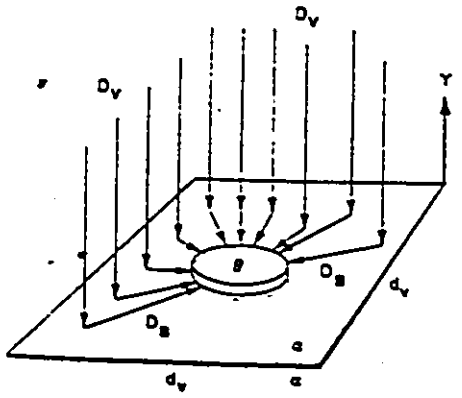

Figure 18. Schematic of right-angled "collector plate" mechanism for lengthening of allotriomorphs, after Bradford and Aaron[59]

CHAPTER 2

MODEL FOR FORMATION OF COLUMNAR ARRAYS OF Co PARTICLES IN Cu-Co ALLOYS

2.1 Preamble

The Cu-Co alloy system has been chosen as a simple binary system exhibiting discontinuous precipitation. One of the main problems addressed in this thesis is to determine the mechanism of formation of columns of spherical Co precipitates at migrating boundaries. The mechanisms envisaged fall into two main classes: those which involve steady-state discontinuous precipitation and subsequent instability of the rod microstructure, and those which require repeated nucleation on the moving boundaries. The non-steady model of repeated nucleation will be given in the discussion section only since it has been discarded in the case of Cu-Co alloys. It may find application, however, in other alloying systems.

2.2 The Theory of Rod Instability

A rod instability phenomenon is associated with energy reduction due to shape changes[62]. In this case, the interfacial energy provides a driving force for the instability whereas the rate of development of the instability is governed by the kinetic processes which operate in a given case and can generally be written as:

$$r^n = r_o^n + \alpha G t \qquad (16)$$

where r_o is the value of the initial radius at time t=0, t is time and G is a parameter characterizing the kinetics of the appropriate mass transport mode, α is a dimensionless constant which depends on the geometry of the unstable phase and the exponent n takes the following integral values depending on the mechanism controlling the kinetics of the process:

n=1 → viscous or plastic flow

n=2 → interface reaction

n=3 → volume diffusion

n=4 → interface diffusion.

There are two modes of shape instability of the rods recognized in the literature; one for the infinite rods and one for finite rods. However, the final result of a row of spherical particles replacing the original rod is similar in both modes, the main difference being the rate of spheroidization which is much faster in the case of rods of finite length than in the case of infinite rods.

Lord Rayleigh[63] showed that a cylindrical column of liquid will break down to a row of spherical drops due to capillary forces, whose effect is to render the infinite cylinder an unstable form and to favour its disintegration into detached masses whose aggregate surface is less than that of the cylinder. The model of instability is assumed to depend

on the small displacements to which a system is subjected, and without which the position of equilibrium, however metastable, could not be departed from. Hence,if the rod geometry were perfectly uniform there would be no driving force for diffusion transport. Therefore, the infinitesimal longitudinal perturbations along the axis of a rod are assumed to be sinusoidal variations resulting in a variation of the principle radii of curvature. After calculating the potential energy due to the capillary force (ie. surface of the liquid) and the kinetic energy of the motion of a sinusoidal variation, Lord Rayleigh derived the law of instability for a given perturbation of wave length λ saying that,if $\lambda > 2\bar{u}r_o$,then the surface is smaller after displacement than before and the system is unstable with respect to it. In addition, the kinetics of the reaction,where volume diffusion inside the cylinder was considered, gives another criterion for the ratio of wave length to radius of the initial unperturbed rod,which leads most rapidly to the disintegration of the cylinder, such that $\lambda_{max} = 9.02\ r_o$.

Nichols and Mullins[64] and Cline[65] have independently extended Lord Rayleigh's analysis of the growth of shape perturbations on an infinitely long cylinder to account for various mass transport mechanisms that can occur in the solid state.

Nichols and Mullins[64] expanded the theory for the spheroidization of rod-shaped precipitates by including sur-

face (interface) diffusion and volume diffusion inside and outside of the particle. In the case of surface diffusion, their result shows that, for wavelengths greater than $\lambda_o = 2\bar{u}r_o$, a cylinder becomes unstable (as previously shown by Lord Rayleigh), i.e., a perturbation with wavelength greater than $2\bar{u}r_o$ will spontaneously increase in amplitude and so become more pronounced with increasing time. Those perturbations corresponding to maximum growth rate with $\lambda_{max} = 2\bar{u}\sqrt{2}\ r_o$, once developed by chance fluctuations, will continue to increase in magnitude until the cylinder actually breaks up into a line of particles with spacing nearly λ_{max}.

In the case of volume diffusion taking place inside the particle, their result for zero growth rate was exactly the same, $\lambda_o = 2\bar{u}r_o$, as in the surface diffusion case, but the maximum growth rate was obtained for the wavelengths corresponding to the value of $\lambda_{max} = 9.02\ r_o$ (as in the case of Lord Rayleigh's treatment).

Finally, in the case of external volume diffusion, λ_o being again $2\bar{u}r_o$, the maximum instability of a cylinder with $\lambda_{max} = 12.96\ r_o$ was obtained. It should be noted that this wavelength is $\sim$ 1.5 times greater than the corresponding wavelengths for both surface diffusion and internal volume diffusion.

Cline[65] included the effect of volume diffusion of the surrounding rods in calculating the diffusion equation

for mass transport. The rate of growth of the sinusoidal perturbation is found to be proportional to the solubility in the matrix, the diffusivity, the surface tension and inversely proportional to the cube of the unperturbed radius r_o given by:

$$\frac{dr}{dt} = \frac{A_k \Delta_k \cos kz}{r_o^3} , \qquad (17)$$

where

$$A_k = \frac{C_\beta \; D \; V_\alpha \; \gamma}{(C_\alpha - C_\beta) RT} \; \psi(k, \frac{S}{r_o}) .$$

Also, the velocity of the interface depends on the wavelength of the instability and on the ratio of the spacing between the rods to the rod radius, S/r_o.

Thus, the results of all these analyses are reducible to two characteristic wavelengths, namely λ_o and λ_{max}. For any longitudinal perturbation of wavelength $\lambda_o = 2\bar{u}r_o$, the cylinder is stable ie. such perturbations decay with time; for $\lambda > \lambda_o$, the cylinder is unstable, ie. such perturbations increase in amplitude with time. For a wavelength λ_{max} the rate at which perturbation develops reaches a maximum value. Thus, for an actual case in which long cylinder break up due to the chance development of fluctuations, one would expect the spacing between the resulting spheroidal particles to coincide closely with λ_{max}. $\lambda_{max} = 2\bar{u}\sqrt{2}\, r_o = 8.89\, r_o$, $9.02\, r_o$ and $12.96\, r_o$ depending upon whether surface (interfacial)

diffusion, internal volume diffusion or external volume diffusion has taken place, respectively.

However, all these treatments assumed cylinders of infinite length, thus ignoring end-effects. But the bulging of the end of the rod produces a prominent perturbation and allows simultaneous shortening of the rod leading to the spheroidization of semi-infinite or finite rods.

Nichols and Mullins[66] and Nichols[67] have analyzed in detail the spheroidization of rods of both semi-infinite rod and finite length when surface diffusion is dominant. The significant length of a semi-infinite rod consumed per spheroidization obviously implies the existence of a critical length of rod above which spheroidization occurs and below which it does not. As the characteristic parameter, the aspect ratio (i.e. length/diameter) of the rod was used to show that, when the aspect ratio is < 7.2, shape relaxation to a single sphere is produced; otherwise spheroidization into a row of spheres should occur.

The mechanism of the shape evolution for a rod then depends on the initial aspect ratio. This criterion can be understood in terms of the characteristic wavelength $\lambda_o = 2\bar{u}r_o = 6.28\ r_o$. For example, if the aspect ratio is less than 7.2 but greater than $6.28\ r_o$ then there is sufficient length available for a wavelength greater than λ_o to develop, so that the two ends of a rod shape particle bulge and recede causing neck

formation in the middle of the rod to occur. But, as this occurs, the two ends recede leaving now less available length between the maxima in the bulges, i.e. less than λ_o. Thus, in this case, the end effects due to the finite rod length make it impossible for $\lambda > \lambda_o$, and the rod is stable, eventually at long times approaching the final spherical shape. This stabilization process is further enhanced by the fact that the average radius is itself increasing.

In the case of the aspect ratio greater than critical (7.2), the greater length of the rod allows the waist to develop until spheroidization results and two particles are formed.

Furthermore, the characteristic time τ for the detachment of a spherical drop from the end of a cylinder of radius r_o may be expressed as

$$r_o^n = \alpha G \tau \ , \qquad (18)$$

where r_o is the initial radius of the rod at time t=0, and n = 2,3,4 depending on which of the kinetic processes among interface reaction, volume diffusion or interface diffusion, respectively, is a dominant one.

The kinetics in the case of a finite rod, is, in addition, dependent on the aspect ratio and, in general, shorter than for infinite rod, as may be seen from Figure 19.

Now we will apply the treatment of spheroidization of rod structure given above to the case of Cu-Co alloys provided

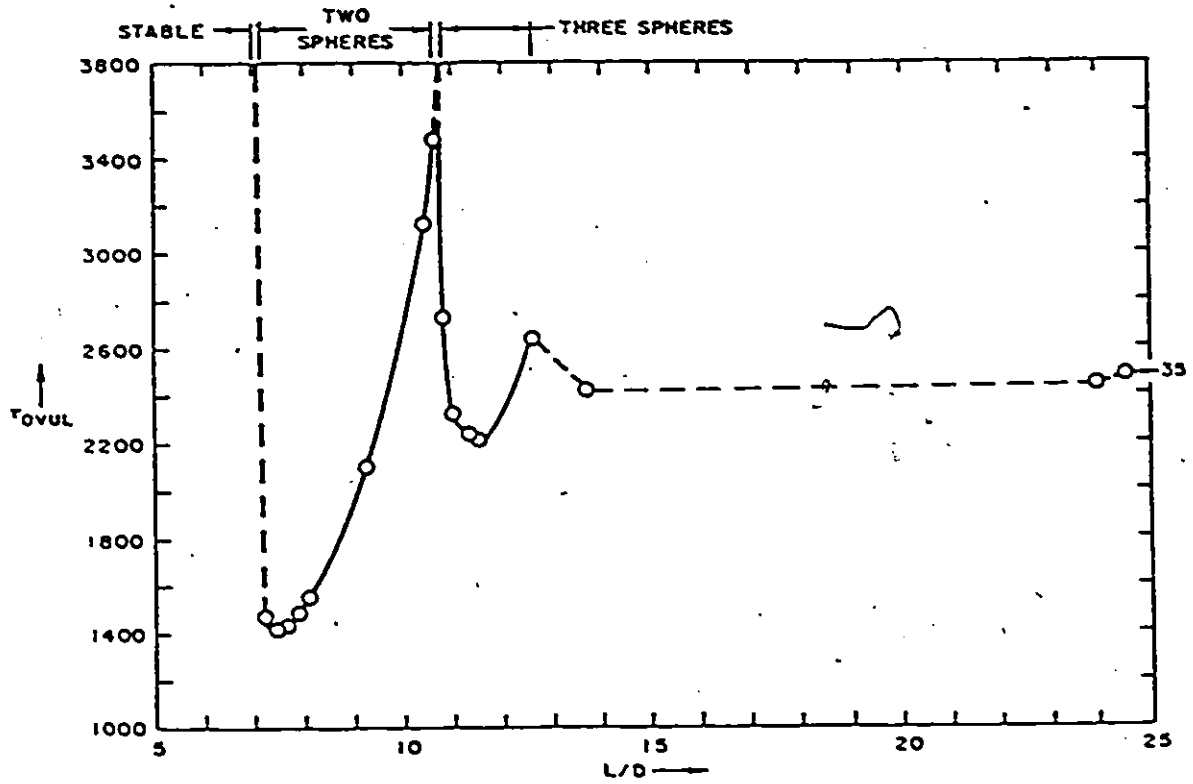

Figure 19. Ovulation time versus aspect ratio, after Nichols[67]

that the coherent rod-like precipitates are formed during the ageing treatment. This suggestion has been given already by Kreye and Hornbogen[16] in a figure caption. Therefore, the model of row formation of Co particles as a consequence of rod instability has been explored in the present study in detail.

An analysis was performed based on a transformation of a unit volume of material containing spherical particles arranged in columnar arrays (rows) of spacing S between rows and of spacing λ between particles in a row, to rod particles of the same spacing S between rods but of a radius different from that of the spherical particles assuming constant volume of particle phase. In this way, we were able to define the regime of values for the radius of spherical particles in rows and the distance between them λ , for which the rod→row transformation mode is possible on a purely energetic basis. The result of this calculation is plotted in Figure 20, as the radius of row particles r, versus distance between them in the row, λ. A straight line is obtained representing equal surface area per unit volume for both kinds of spatial arrangement of precipitates. For all combinations of values of r and λ corresponding to points lying above this curve, rod → row transformation is possible.

After defining these conditions, another parameter associated with spatial distribution of the particles, the volume fraction, was included. Figure 21 represents the changes of volume fraction V_f versus radius of row particles r for a

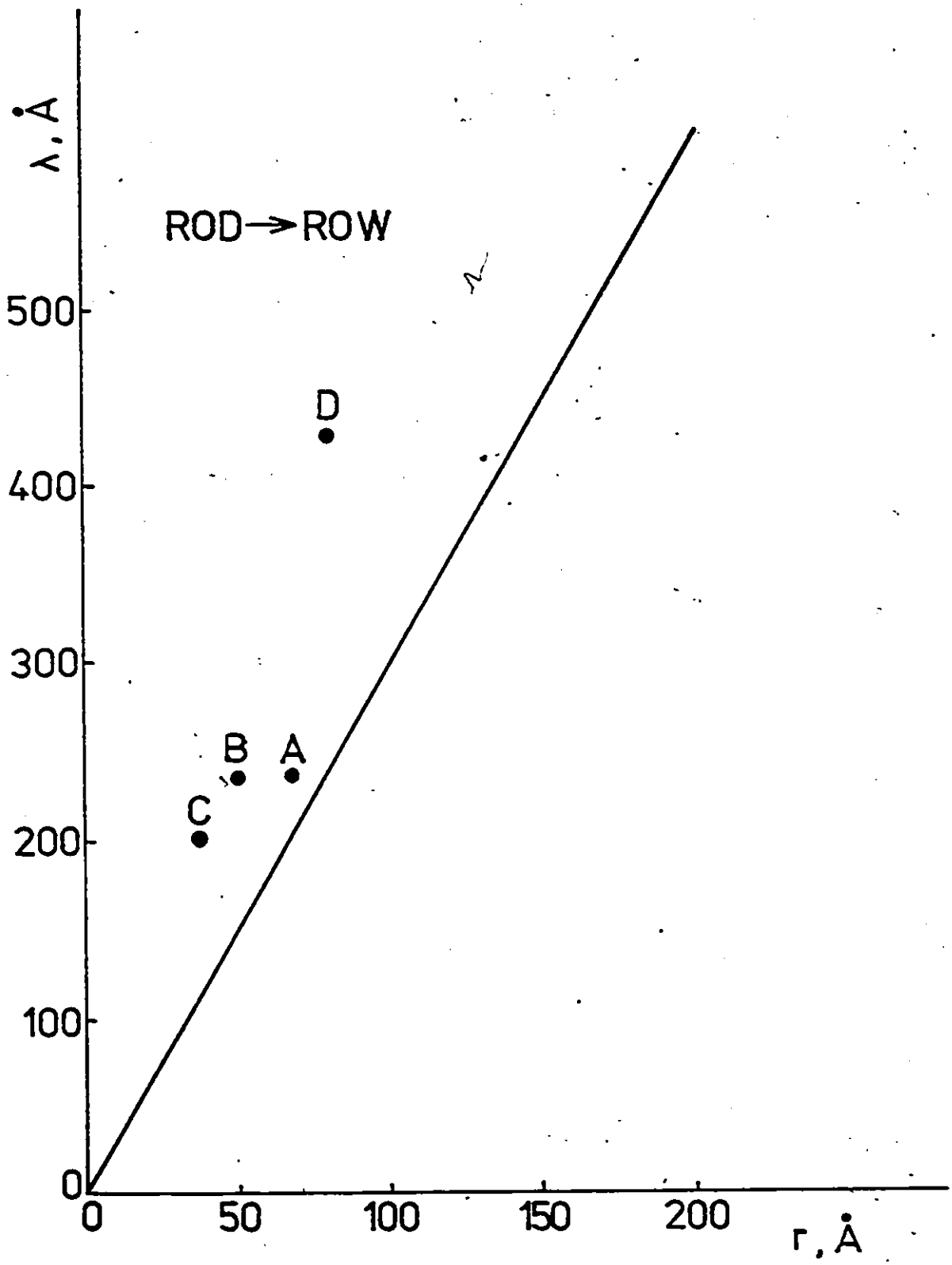

Figure 20. Computed values of radii of spherical particles in rows and the distance between them for which rod→ row transformation is possible.

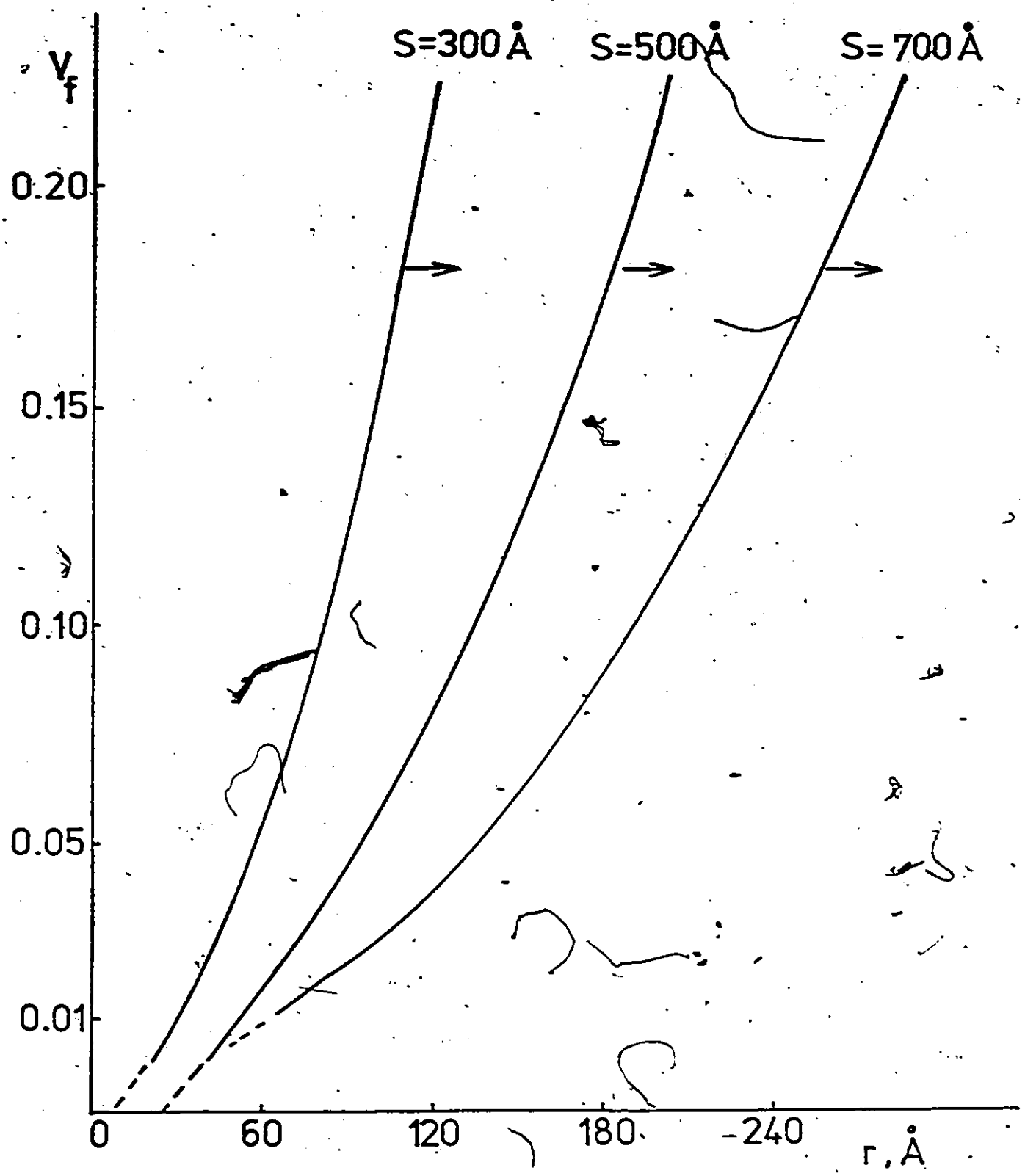

Figure 21. Computed values of volume fractions and radii of spherical particles in rows for which rod→row transformation is possible

given value of S. This graph shows an exponential behaviour of volume fraction versus particle radius indicating the possible range of volume fractions for a given radius of spherical precipitates for which rod instability could occur. As before, it is clear that all combinations of volume fraction and radius of particles in rows above the curve of equal surface areas cannot lead to rod spheroidization.

Since it is difficult to detect experimentally the existence of precursor rods under many thermomechanical histories, this analysis will serve as a simple preliminary test for the rod instability model. The kinetics of the reaction can further be analyzed through the times τ and t needed for spheroidization of rod particles of given radius (equations 17 and 18) which together with the thermodynamic conditions give a complete test of the feasibility of the proposed model for rod instability in Cu-Co alloy system.

CHAPTER 3

EXPERIMENTAL PROCEDURE AND TECHNIQUES

3.1 The Cu-Co Alloy System

The Cu-Co alloy system has been chosen because the continuous precipitation behaviour of these alloys is well known[68-71] and discontinuous precipitation[17] has been found as well.

The phase diagram of Cu-Co system[72] is shown in Figure 22. Copper dissolves about 5.6 at % (5.2 wt %) of cobalt at 1110°C and the solubility decreases to 1.30 at 800°C, 0.76 at 700°C and 0.54 at T at 650°C. Aging of a supersaturated solid solution at these temperatures results in precipitation of an f.c.c. cobalt-rich phase containing about 10% of copper in solution, which is very resistant to transformation. The precipitates are coherent and spherical with associated elastic strain fields since the entire mismatch between unequal size lattices of f.c.c. cobalt and copper is often accommodated elastically.

In addition to its simplicity as a binary alloy, Cu-Co has advantages for investigation by electron microscopy (the technique used in this study for observation of microscopic aspects of precipitation reaction). Cu-Co alloys have been thoroughly investigated by electron microscopy and the

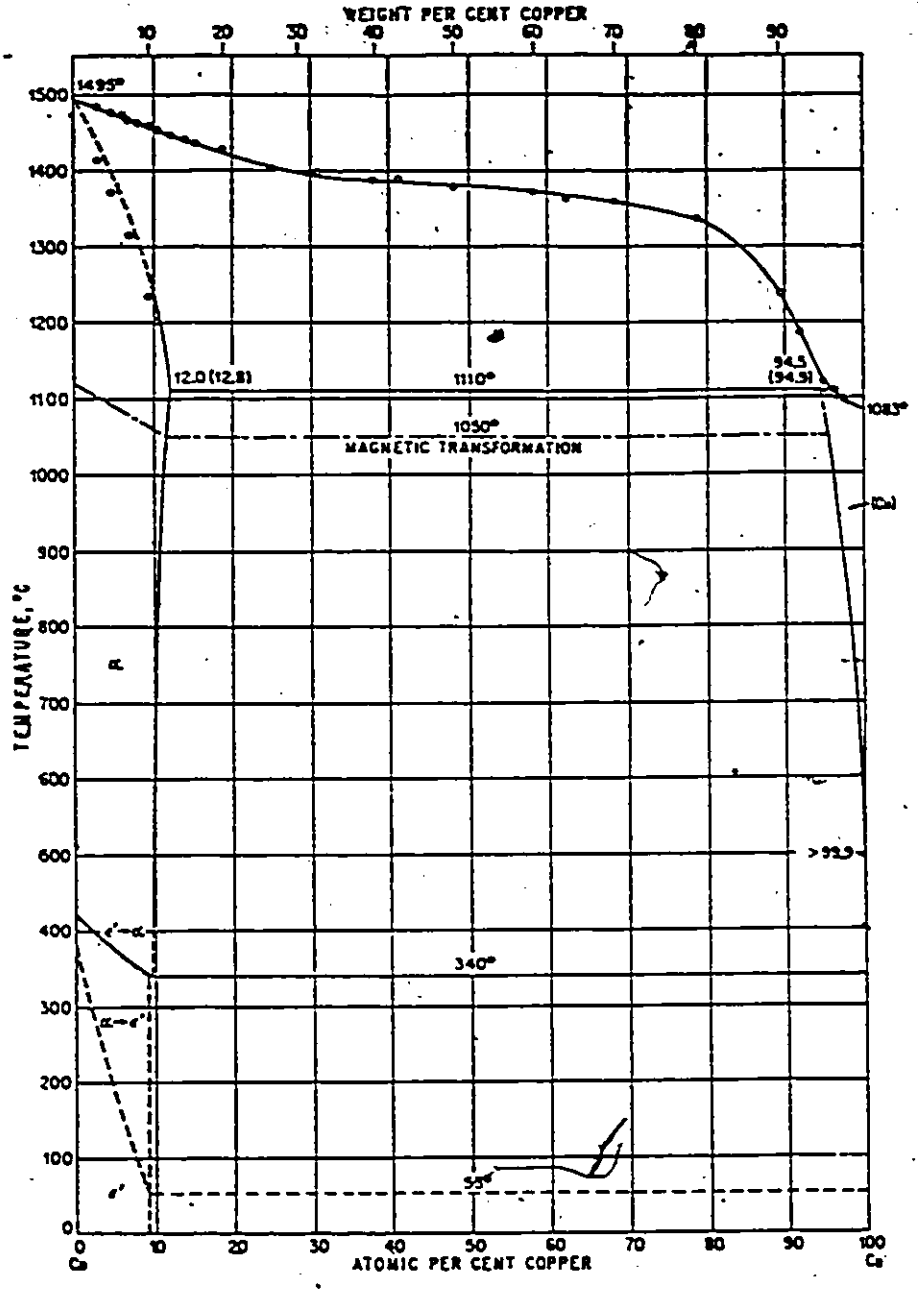

Figure 22. Phase diagram of Cu-Co system, after Hansen[72].

theory of diffraction contrast due to coherency strains is well established[73-76].

In this particular system, the contrast appears as a pair of lobes approximately symmetrically placed about a line of no contrast. The contrast is visible only when one or more sets of lattice planes diffracts strongly; it disappears as the foil is tilted away from this orientation. This specific type of contrast has been interpreted as due to the elastic distortions of the matrix around the coherent particle. Phillips and Livingston[73] were able to calculate the main contrast effects observed experimentally from the kinematical theory of diffraction while Ashby and Brown[74,75] have made a dynamical calculation which enables additional effects to be predicted. The precipitate remains coherent up to about 600 Å diameter after which complete loss of coherency occurs and is marked by an absence of strain fields and the presence of prominent moiré patterns. This usually happens in all samples after prolonged aging[76].

Finally, there exist in the literature[77,78] data on the diffusion coefficients of cobalt in a copper matrix as well as on the measurements of lattice parameter changes with changes in composition[71].

3.2 Preparation of Alloys

The materials used in preparation of the Cu-Co alloys were copper, (OFHC) and electrolytic-grade cobalt.

The copper and cobalt were cut and weighed to give ingots of about 100 gr., after which the alloys were melted in an argon-arc furnace.

3.3 Specimen Preparation

The ingots were cold rolled to sheets useful for further preparation of the specimen to be used for transmission electron microscopy studies. These specimens were then homogenized in evacuated quartz tubes at the temperatures of solid solutions of particular alloys. Solid solution treatments consisted of one hour at particular temperature (i.e. 700°C, 860°C, 960°C and 1060°C for alloys containing 0.90 wt % of Co, 1.5 wt % Co, 2.82 wt % Co and 3.5 wt % Co, respectively). The homogenized solid solution specimens were then deformed about 50% by rolling at room temperature in order to obtain a fine grained material. A small grain size is essential for electron metallography if there is to be a high probability that the grain boundaries lie in an electron-transparent region.

The deformed samples were re-homogenized at the respective homogenization temperatures used before rolling. The time of homogenization was 2 minutes. Such a short time was chosen to prevent grain growth but to allow the annihilation of the dislocations introduced by rolling. In this way, a fine grained dislocation-free structure was obtained.

3.4 Precipitation Heat Treatment

The apparatus for the precipitation treatments must allow:

a) Heating of the sample to the desired temperature as quickly as possible;

b) holding the sample at temperature, with little oxidation (especially important for thin sheet specimens); and

c) quenching the sample to preserve as many features as possible.

Two types of furnace were used to meet these requirements. Since a high growth rate was expected, and only short precipitation times were needed, either a stirred $BaCl_2$,KCl and NaCl salt bath was used for the temperature range from 620°C to 800°C, or stirred $NaNO_3$ and KNO_3 salt bath was used for the temperature range from 400°C to 600°C. A chromel-alumel thermocouple was used attached to the specimen with a manually operated potentiometer to measure the temperatures accurately. The samples were quenched into water. They emerged with an oxide scale which could usually be removed by chemical means. The salt pots were used for precipitation times of 2 min, 5 min and 10 minutes.

For longer heating periods (above 30 minutes),the specimens were sealed in Pyrex tubing in a vacuum and aged in a horizontal furnace, inserted into the hot zone and then water quenched. For lower temperatures (below 500°C),a lead bath was used and the specimens had to be protected from copper

dissolution in lead by holding the samples during the aging in a stainless steel tube.

One set of experiments was performed with deformation of the samples prior to heat treatment. The samples, after solution treatment, were cold rolled at room temperature. The amount of deformation ranged between 10% and 50%.

In addition, an alloy was prepared containing about 50% Co; the ingot was homogenized at 1000°C and deformed about 50% by rolling at room temperature prior to an equilibration treatment for three days at 900°C. This alloy was then examined in order to estimate the relative free energies of incoherent Co-Cu and Cu-Cu boundaries.

3.5 Optical Microscopy

a) Surface preparation

Sheet specimens were used for light microscopy. These specimens were not mounted and prepared by standard metallographic techniques but were simply chemically polished using the following chemical solution at 70°C:

50 parts HNO_3

25 parts orthophosphoric acid

25 parts acetic acid.

b) Technique of measurement

A Carl Zeiss optical microscope was used for investigation of the sample and photography. Measurements of grain size were made by using micrographs. The linear intercept

statistical method[79] was used for measurements of grain diameters. Figure 23 represents a typical specimen used in this study.

3.6 Electron Microscopy

a) Thin foil preparation

Sheet samples of about 1 mm thickness were prethinned chemically to about 0.1 mm using the method described in the previous section. The thinned samples were punched to give 3 mm diameter discs to fit the electron microscope specimen holder.

The disc specimens were electrothinned using the two-jet technique (in a Streuers' "Tenupol"). The electrolyte contained one part of orthophosphoric acid to two parts of water. A voltage of 20 V[80] gave satisfactory specimens. The samples were rinsed with methanol. After drying, the specimens were dropped into the electron microscope specimen holder.

b) Microscope operation

A Phillips 300 electron microscope operating at 100 kV with a tiltable specimen holder was used in this study. The magnification was calibrated from a series of photographs of a carbon replica of a diffraction grating. The rotation was determined as a function of magnification setting using these photographs and pairs of microscopy and diffraction photographs.

Figure 23. Grain size structure in Cu-Co system investigated (80 x)

Transmission electron micrographs were recorded along with selected area diffraction patterns, in order to permit determination of the foil orientation as well as of the diffraction conditions responsible for the contrast effects in the micrographs. Dark field and weak beam techniques were employed in order to reveal the shape and size of precipitates.

c) The determination of particle size and spacings

Figure 24 shows schematically the two main types of contrast effects about a coherent spherical particle. It will be seen that, in order to determine the correct diameter of a particle, the distance "D" should be measured. The average particle size was determined from measurements on as many particles as seen in a given area, usually 20 to 30 particles, at a magnification of about 40000, by using the eye magnified lens with an eyepiece scaled grid. The standard deviation was about 15%

The two characterizing spacings, between the particles in a row and rows themselves, were measured from the micrographs as well. The major error of the measurements is expected to be involved in the average measured spacings due to the variation in the spacings. The proper spacing to be measured was chosen from those micrographs representing the rows of particles normal to the grain boundary interface; otherwise, the obliqueness would give higher or lower values of measured spacings. Another problem in spacing measurement comes from the three-dimensional sections of projected rods

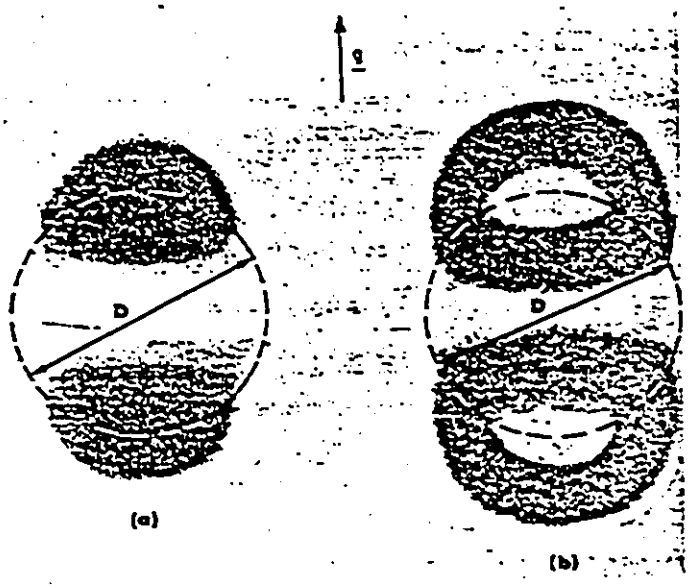

Figure 24. Schematic representation of calculated diffraction contrast produced by a coherent spherical particle, after Phillips and Livingston[73]

in the micrographs. However, the thickness effect is reduced by choosing micrographs with regularity in S, and those in which projection effects could be taken into account. Otherwise the true spacing is expected to be ∿ 1.5 the apparent spacing.

d) Determination of volume fraction

In order to determine the volume fraction of precipitates, the foil thickness was required. The foil thickness was measured by the method of extinction thickness fringes[81]. The associated diffraction pattern was required also. The effective thickness so measured showed about a 30% overestimate if no effect of extinction distance was taken into account. The foil thickness so determined was 986±250 Å.

The volume fraction was determined by determining the number and size of the particles in a given micrograph for a known sample thickness.

CHAPTER 4

RESULTS

4.1 Preamble

The aim of this work was the investigation of the columnar microstructure occurring discontinuously at grain boundaries. Four copper-cobalt alloys of different composition (0.90 wt % Co, 1.52 wt % Co, 2.82 wt % Co and 3.57 % Co) were aged at different temperatures ranging from just below the solvus temperature down to 400°C after homogenization in the solid solution range for one hour. Some alloys were given cold work prior to heat treatment. In addition, an alloy of 50-50 wt % Cu-Co was treated in such a way as to give equilibrated structures in order to estimate the relative interfacial energies of Cu-Co interfaces.

Discontinuous precipitation was found to occur under all conditions, in the form of either rod particles or spherical particles aligned in rows normal to grain boundaries. Cold work was not required for discontinuous precipitation as was thought to be the case by Kreye and Hornbogen[16] and, when present, it did not significantly effect either the morphology or kinetics of discontinuous precipitation.

The main features of the microstructures observed are:

i) spherical coherent particles of the Co phase arranged in columns normal to the advancing interface with a regular distance S between the columns as well as a distance λ between the particles in a column;

ii) rod-like coherent particles with a regular interrod spacing S;

(iii) bumpy rods; and

(iv) the copious general precipitates in front of the moving boundary with or without precipitate free zones at the boundary.

Results will be presented in terms of representative electron micrographs, each one representing a set of about ten micrographs of similar microstructures in a thin foil. The discontinuous mode of precipitation did not occur at all, or even most, grain boundaries but was localized at a few grain boundaries in most specimens.

Before presenting the results obtained a brief discussion on contrast phenomena will be given. It will concern the contrast effects coming from coherent particles of two kinds: spherical particles aligned in a column and rod-like particles.

A particular type of diffraction contrast is associated with the spherical Co particles in dilute Cu-Co alloys, due to their spherically symmetrical strain fields. The image resembles a pair of lobes symmetrically placed about a line of no contrast and its width, defined by a fractional intensity

variation with respect to background, was found to depend principally on the dimensionless variable $\varepsilon \vec{g} r^3/\xi_g^2$ where ε is the elastic strain, $\vec{g}$ is the operating reflection, r is the radius of the particle and ξ_g is the extinction distance. The intensity is given in Figure 25[74]. Therefore, by calculating ε from a given mismatch of Co particles with the Cu matrix, measuring the particle radius from the micrograph, finding $\vec{g}$ from the associated difraction pattern and computing ξ_g for the operating reflection $\vec{g}$, it is possible to obtain an estimate of the image width. If the particles are aligned in a row, one can estimate the minimum distance between the particles of a given radius at which the images will not overlap. For example, by using the (111) operating reflection for which ξ_g is 222 Å, the 50% image width is calculated to be 180 Å for a particle radius of 70 Å. Therefore, the particles in a row should be 180 Å apart in order to avoid overlapping of the strain fields. However, with closer interparticle distances, and for similar diffraction, superposition of the images is expected[89]. This overlapping of the strain fields can contribute to the complexity of the image, especially in the case where the operating reflection is normal to the column (row) axis. The image can then have the appearance of a bumpy rod, in which case it will be difficult to distinguish between rows and rods. However, the overlapping of images where $\vec{g}$ is parallel to the row axis will maintain the lines of no

contrast for each particle, therefore making possible the distinction of the "row" microstructures. Hence, whenever there was difficulty in distinguishing whether rods or spherical particles aligned in rows were present, micrographs taken with the operating ($\vec{g}$) vector parallel to the column axis were used.

In the case of rod-like particles with the coherent particle-matrix interface along the rod axis, the matrix contrast will be given by two parallel contrast lines with the line of no contrast between them. By analogy with a thick-walled tube under internal pressure[10], the displacement in the matrix at great distances r from the rod is found to be $u_{rr} = k/r$ where k is a constant. With the rods lying parallel to the foil surface, the matrix contrast will depend on the operating reflection $\vec{g}$ in the following way: when $\vec{g}$ is at right angles to the rod, $\vec{g}\cdot u = 0$ in the column passing through the particle at right angles to the foil. Also, $u \to 0$ when $r \to = \infty$. Between these limits, $\vec{r}\cdot\vec{g} \neq 0$. Thus the contrast is 0 when $r = 0$, goes through a maximum on each side of the rod and dies off with increasing distance r from the rod. When $\vec{g}$ is parallel to the rod, $\vec{g}\cdot\vec{u} = 0$ for all $\vec{r}$'s and no matrix contrast should be present. If the rods make a certain angle with an operating reflection or with the foil surface, the observed contrast is rather more complicated. A "bumpy" rod would be observed under conditions where $\vec{g}$ reflection is at some angle to the rod. Figure 26 is a schematic representation of the influence of the operating $\vec{g}$ vector on the contrast of

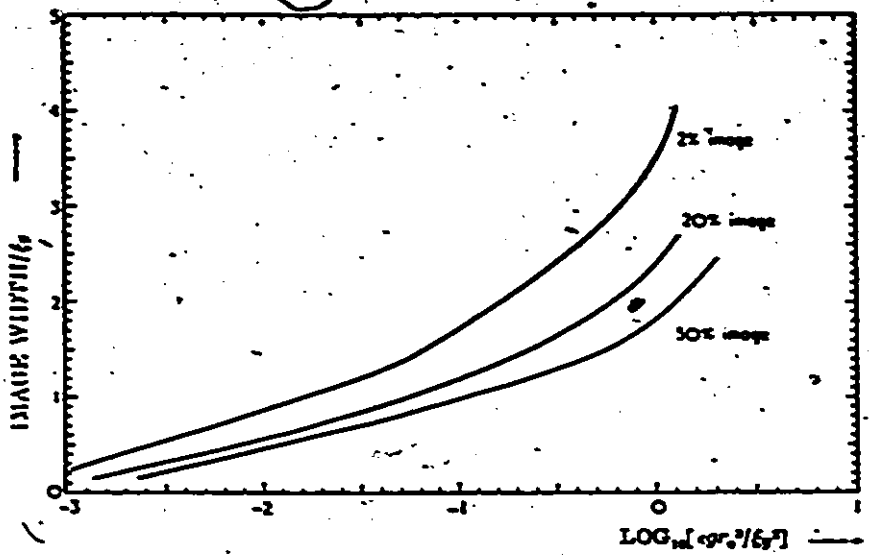

Figure 25. Variation of image width with ε, $\vec{g}$, r_0 and ξ_g after Ashby and Brown[79]

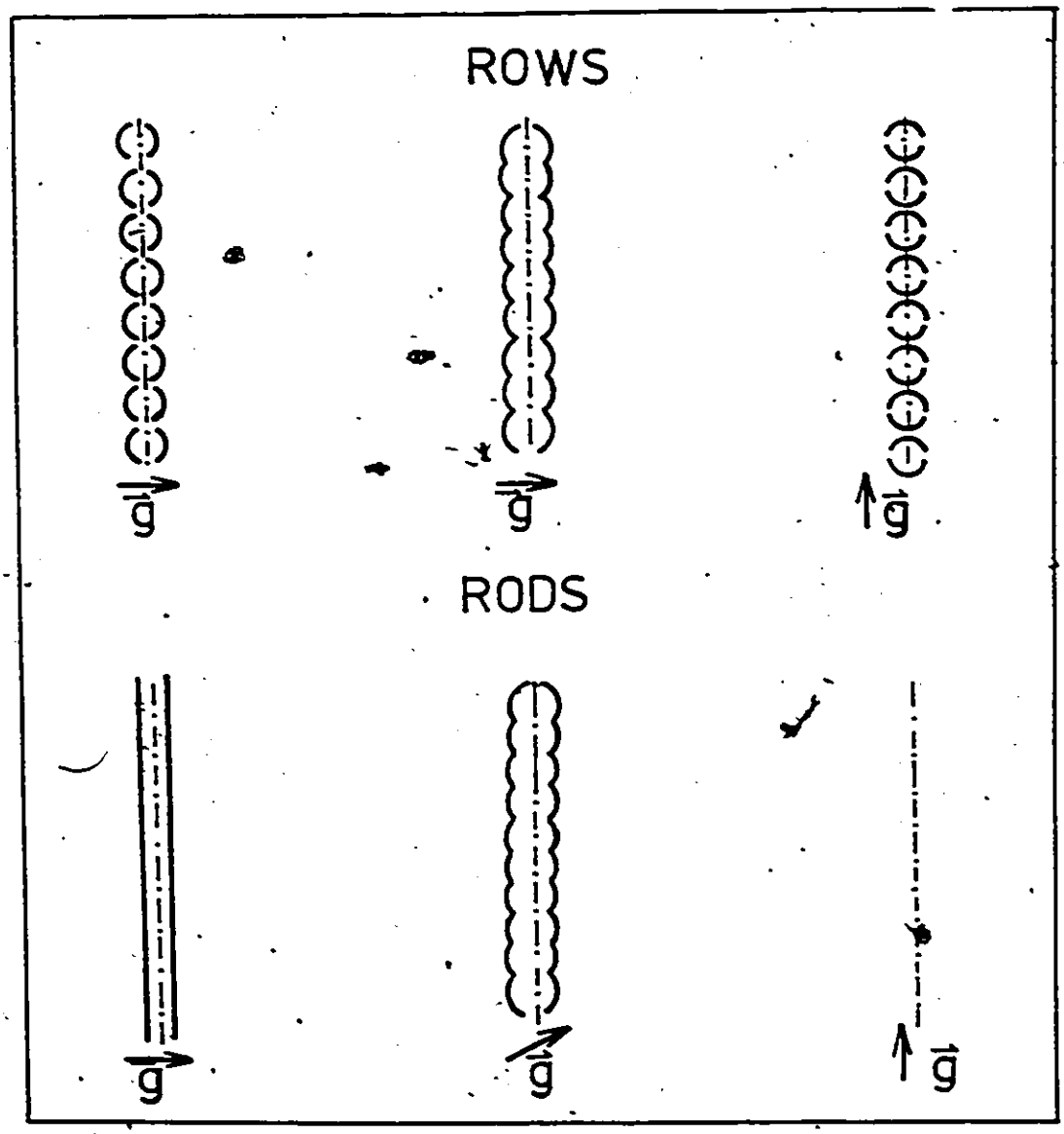

Figure 26. Schematic representation of the influence of operating $\vec{g}$ vector on the contrast of coherent rows and rods.

coherent rows and rods.

Therefore, we conclude that a complicated but similar contrast effect could be obtained from spherical coherent particles aligned in a row and from rod-like coherent particles under some condition of operating $\vec{g}$ vector and foil orientation. In order to interpret these microstructures, the condition of $\vec{g}$ parallel to the column axis was chosen.

There is an additional fact aiding in distinguishing the rod microstructure from rows, and that is the effect of precipitate etching during electropolishing. The shapes of the holes resulting from particle etching are perhaps the best evidence for their morphology since there is no elastic strain contrast effect associated with them. Figures 27-30 represent the various contrast effects of rows and rods due to different conditions of operating reflection as discussed above.

4.2 Experimental Evidence

The experimental results will be presented in terms of two main kinds of morphology; columnar array of aligned spherical particles, and coherent rods. Some microstructures of a 50-50 wt % Cu-Co alloy, treated to facilitate the estimation of the relative free energies of Cu-Co and Cu-Cu interfaces, will also be presented.

In the following only the main features of the observed microstructures will be pointed out in the text, while the details of each micrograph will be given in the caption.

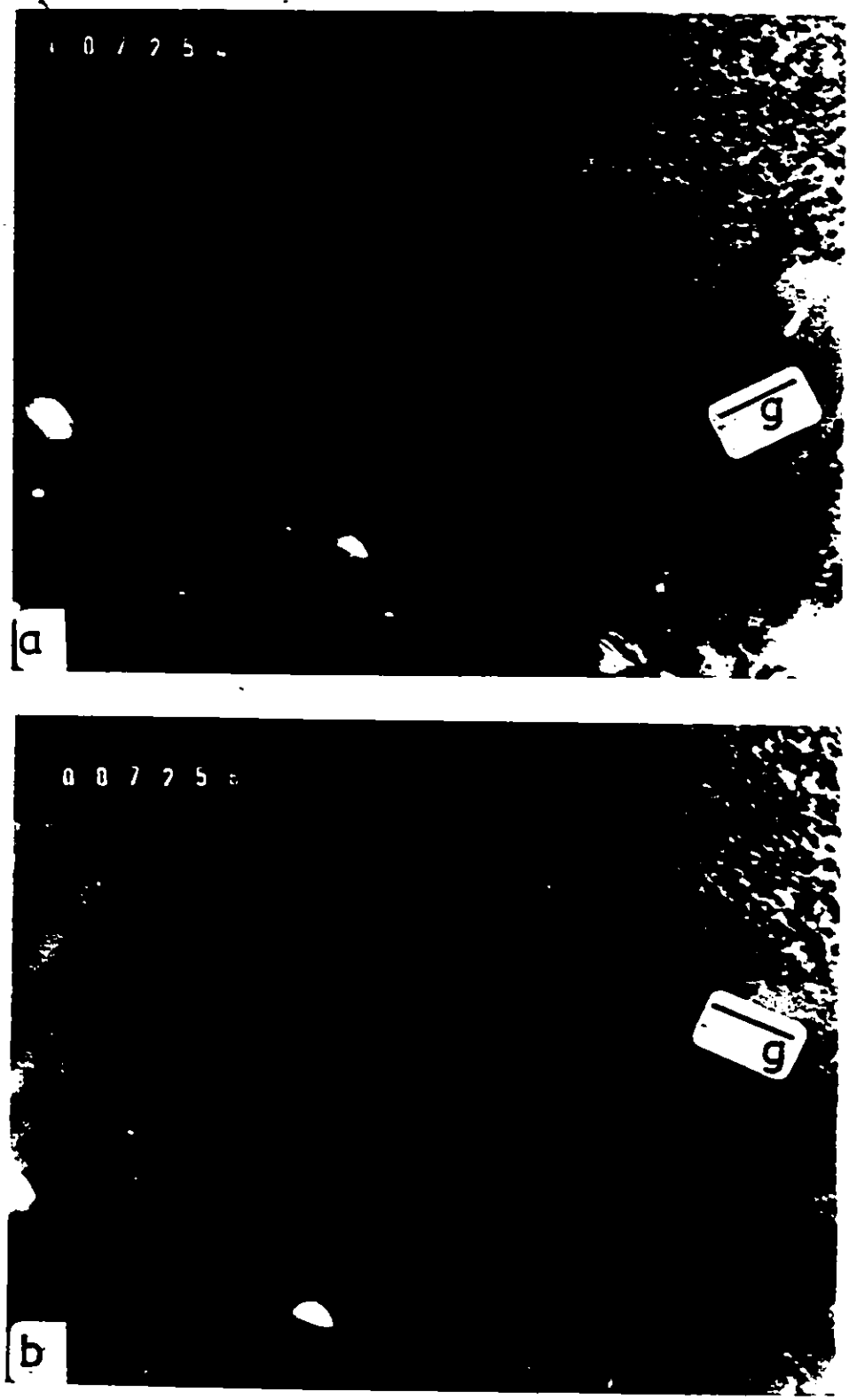

Figure 27. Cu-2.82 wt % Co; 700°, 10 min. a) $\bar{g}$ about 30° to column axis shows a complex contrast (65000×) b) $\bar{g}$ normal to column axis shows distinct particles (65000×)

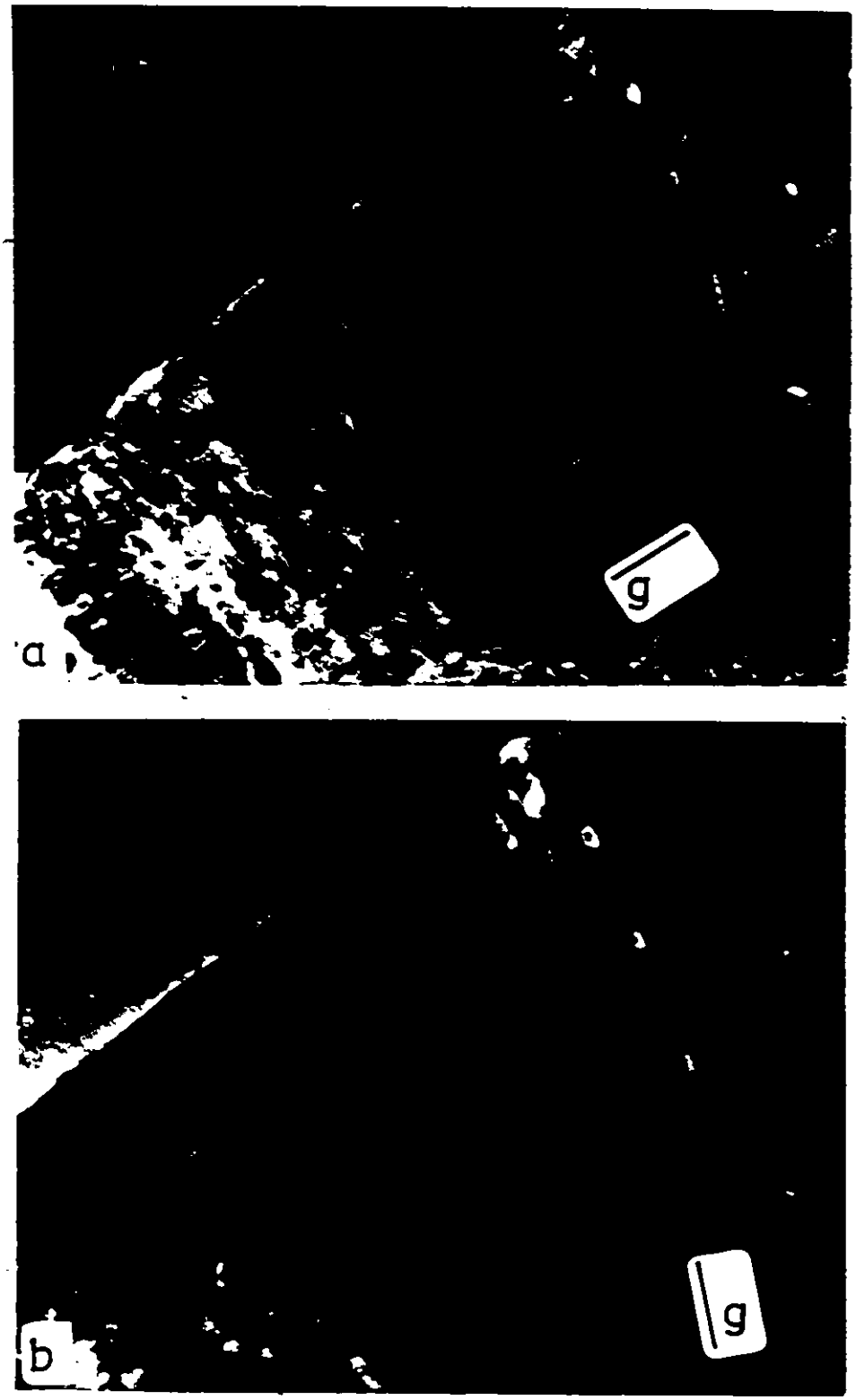

Figure 28. Cu-1.52 wt % Co; 670°, 10 min.. a) $\vec{g}$ normal to column axis shows rods and rows of particles co-existing together (61000x), b) $\vec{g}$ almost parallel to column axis does not reveal rods; PFZ is seen in front of the boundary (71000x).

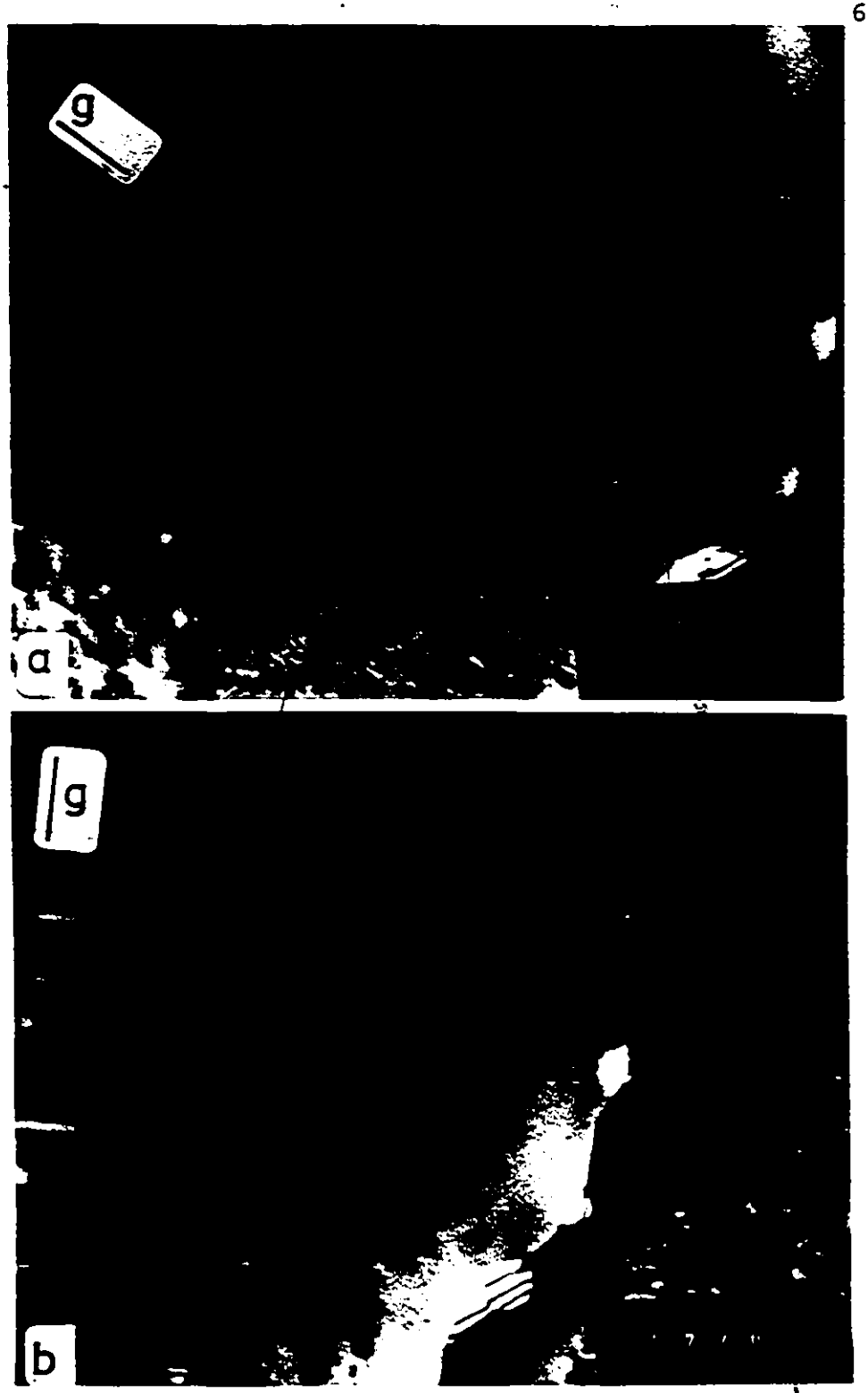

Figure 29. Cu-2.82 wt % Co; 760°C, 100 min. a) $\vec{g}$ at 50° to rod axis shows bumpy rods while etched out rods show thickness fringes contrast (there is no line of no contrast) (51000×). b) $\vec{g}$ at 90° to rod axis shows typical two parallel black line of contrast about line of no contrast while etched out particles appear as white rods. There is PFZ on both sides of the boundary, due to the growth of incoherent grain boundry particles (51000×)

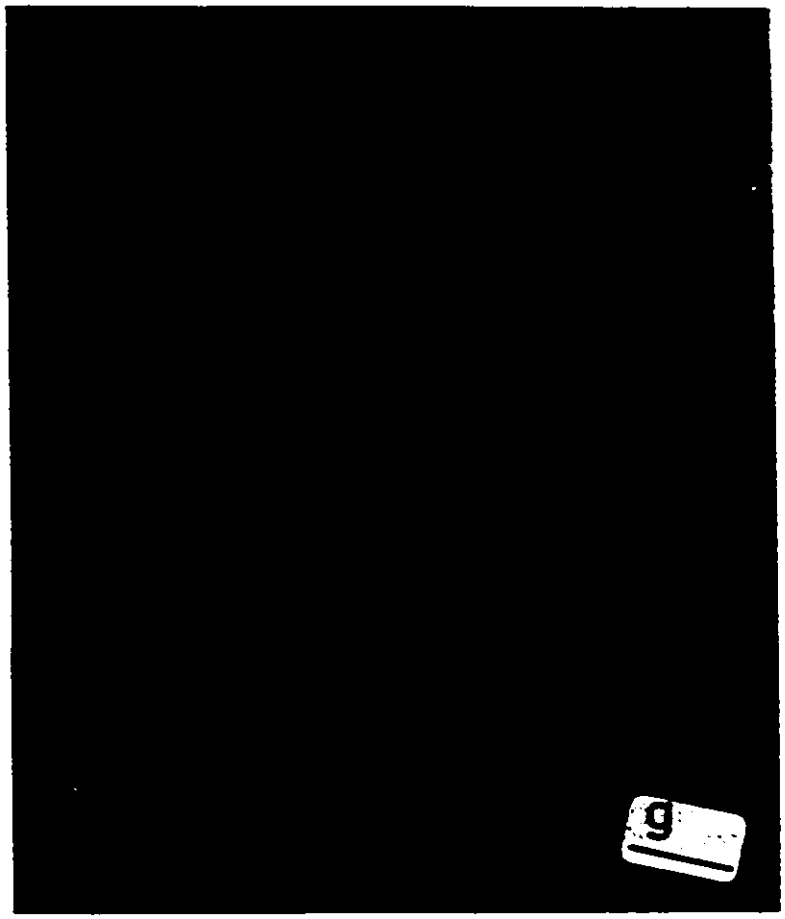

Figure 30. Cu-1.52 wt % Co;450°C, 25 min. Rod particles are seen at the bottom where g is normal to the rod axis, while at the top where g makes some angle to the rod axis, rods appear with bumpy contrast. Homogeneously nucleated particles are seen to be in contact with the grain boundary. (68400x).

Micrographs 31-40 all show isolated spherical coherent particles arranged in rows behind the reaction front. The colonies of particles are normal to the grain boundary. The region transformed into rows of particles always shows the same contrast as the region behind it, indicating that the reaction occurs through simple migration of pre-existing boundaries. In any one region, boundaries generally appeared to move in only one direction. Some microstructures (Figures 35 36 and 38) showed a precipitate free zone (PFZ) in front of the reaction front. This PFZ could originate either from a volume diffusion component in the reaction or from the cessation of boundary motion prior to quenching. It is a characteristic feature for microstructures observed at higher temperatures. At lower temperatures, the advancing front was observed to be in contact with the matrix particles, thus indicating the predominant effect of the grain boundary diffusion process (Figure 33). Figures 31 and 32 have a further interesting feature: the aligned structure terminates at a facetted boundary, suggesting that a high-energy disordered grain boundary "dropped" into a low-energy orientation during growth.

The rod-like particles are seen in Figures 41-51. The rods are visible as a parallel double-line contrast. A few dislocations were sometimes found in the discontinuity transformed region. They could have come from the incoherent grain boundary as it moved forward. Diffraction patterns showed no systematic twin or coincident site lattice orientation relationships for the

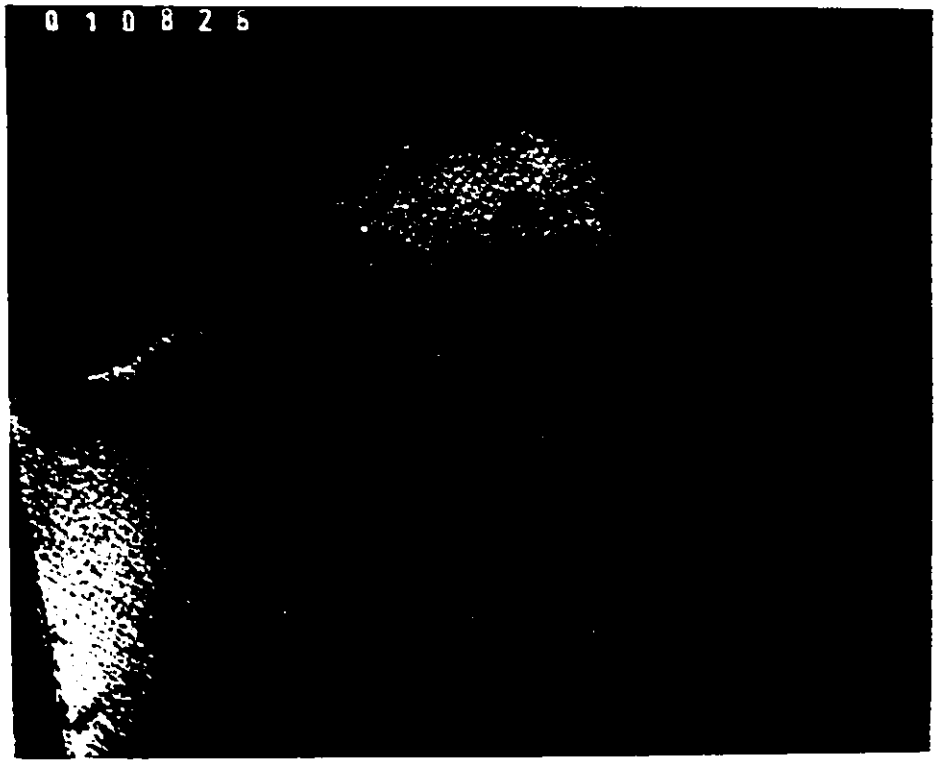

Figure 31. Cu-1.52 wt % Co; 600°C, 2 min. Rows of fine particles are visible. Aligned structure terminates at facetted boundary marked with an arrow. (41250x).

Figure 32. Cu-1.52 wt % Co; 600°C, 2 min. a) Three grains of rows of fine particles are seen. At A and B the row structure terminates (1100000×). b) The same area as a) with different tilting (110000×)

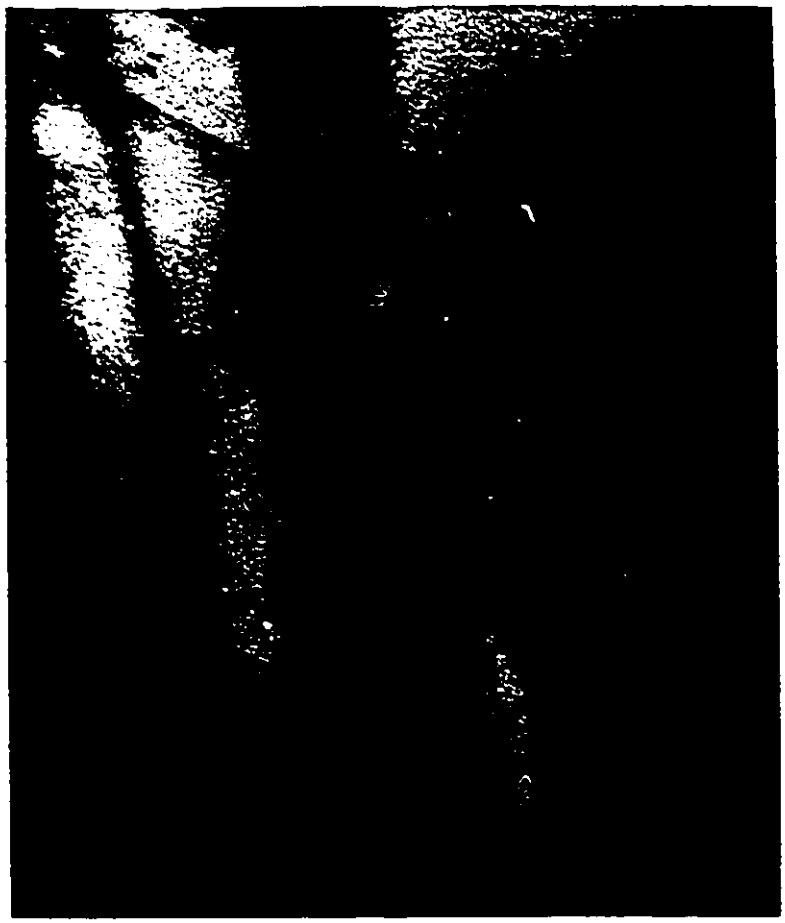

Figure 33. Cu-1.52 wt. % Co; 600°C, 2 min. Fine particles aligned in rows are visible. The grain boundary is straight and in contact with homogeneously nucleated particles in front of it. (53250x).

Figure 34. Cu-1.52 wt % Co; 750°C, 2 min. Fine particles aligned in rows are present. The inclined grain boundary in contact with rows enables us to differentiate between true spacing and apparent spacing (53250×).

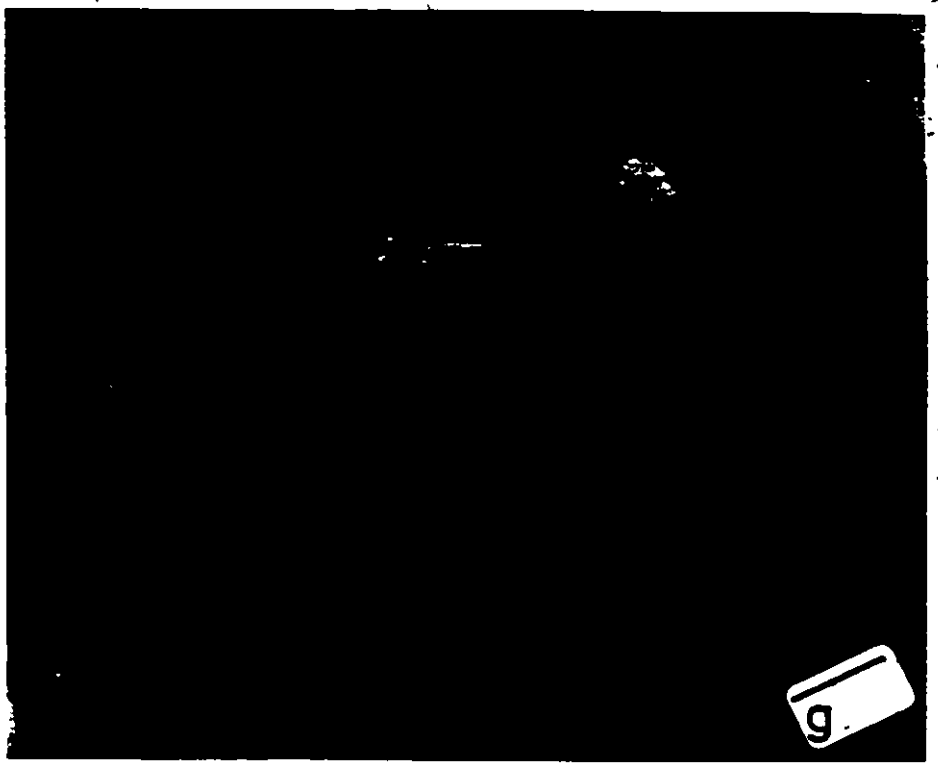

Figure 35. Cu-1.52 wt % Co; 670°C, 10 min. Rows of spherical coherent particles and PFZ are visible (119000×).

Figure 36. Cu-1.52 wt % Co; 700°C, 10 min. Rows of spherical particles with PFZ in front of the grain boundary are present (63750×).

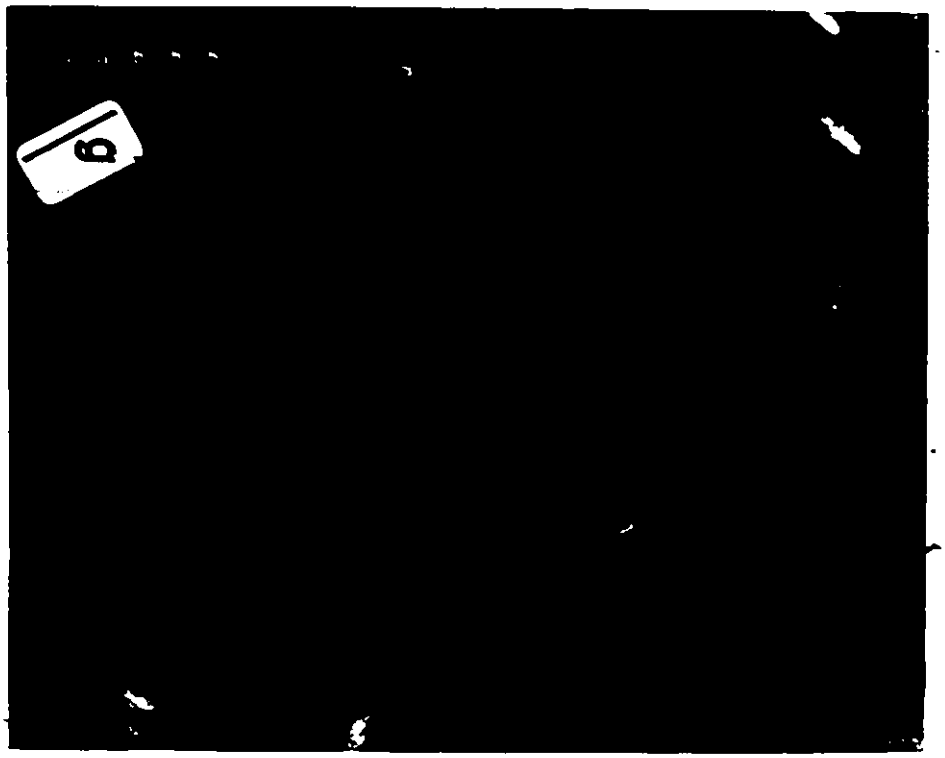

Figure 37: Cu-1.52 wt % Co; 700°C, 10 min. Aligned coherent particles in rows are present (53250×).

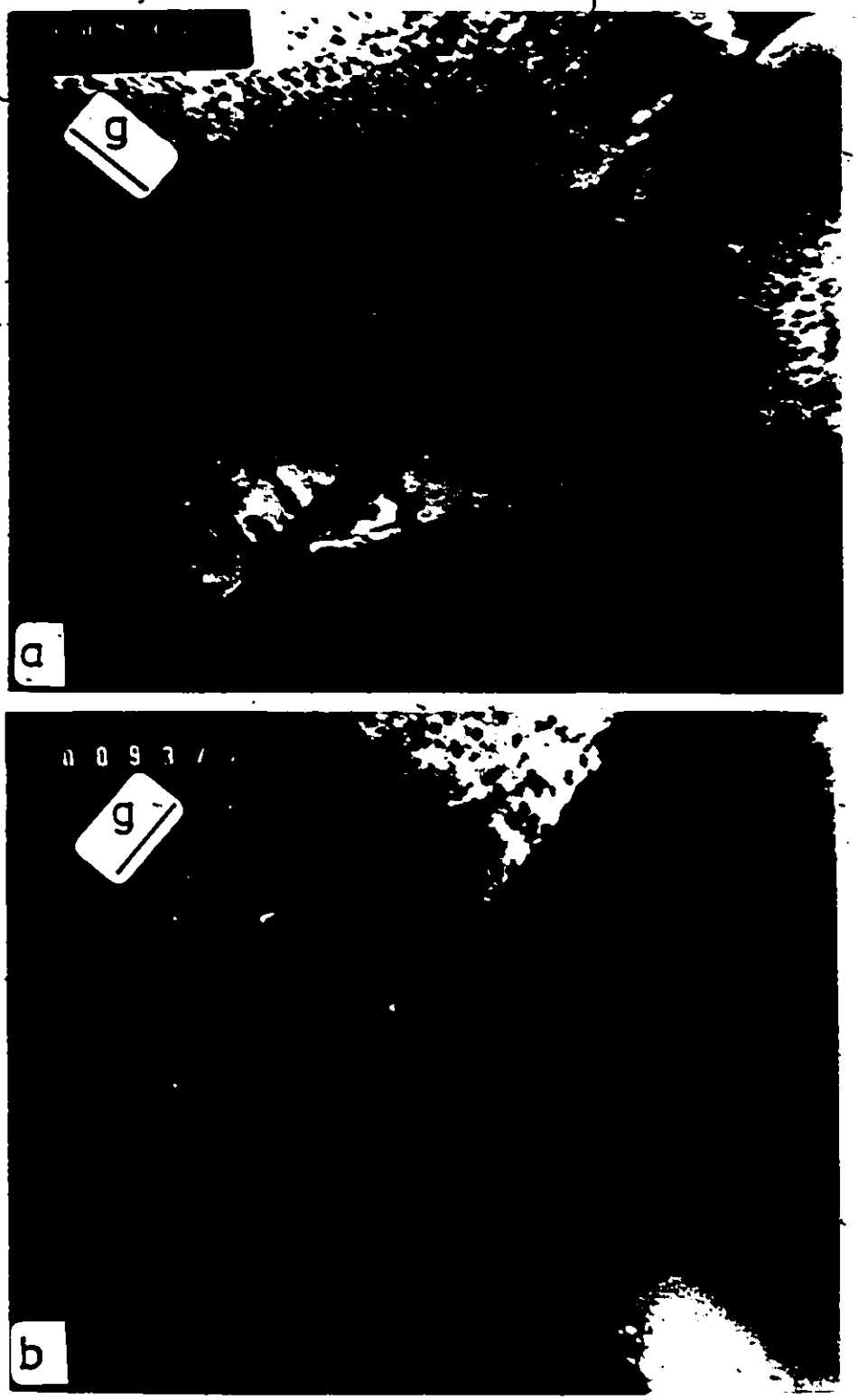

Figure 38. Cu-1.52 wt % Co; 750°C, 2 min. a) Row of particles with g parallel to row axis (65000×), b) the same area as a) with g normal to row axis (65000×)

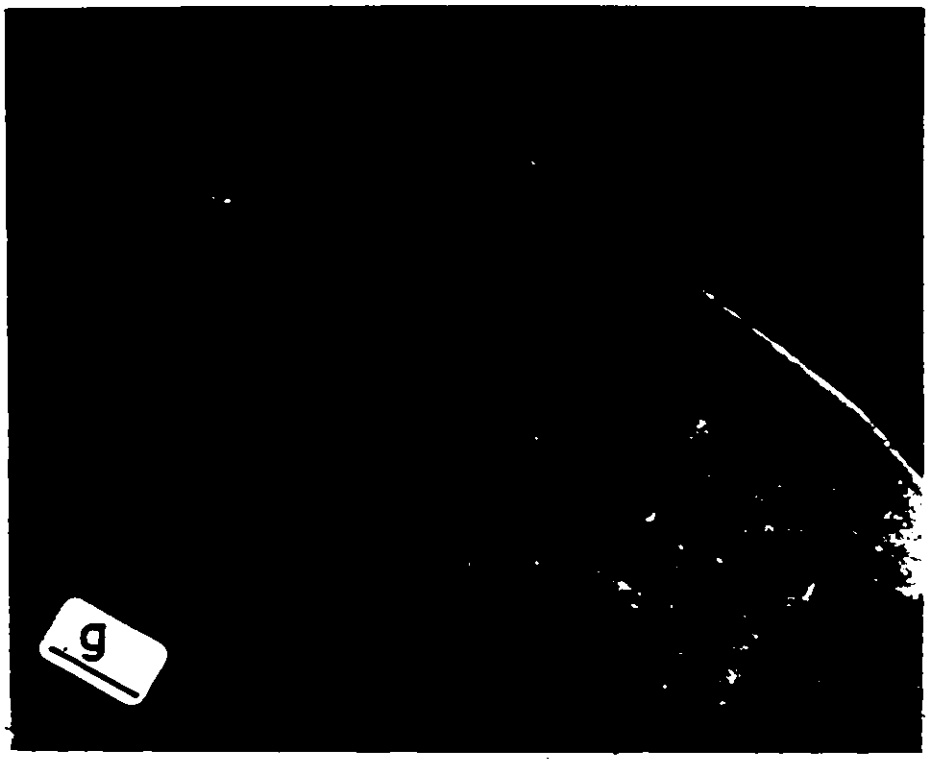

Figure 39. Cu-1.52 wt % Co, 750°C, 5 min. Coherent spherical particles in rows (53250·).

Figure 46 Cu-2.82 wt % Co; 750°C, 5 min. A large transformed area of rows of fine particles. Two grains transformed into rows are meeting (53250×).

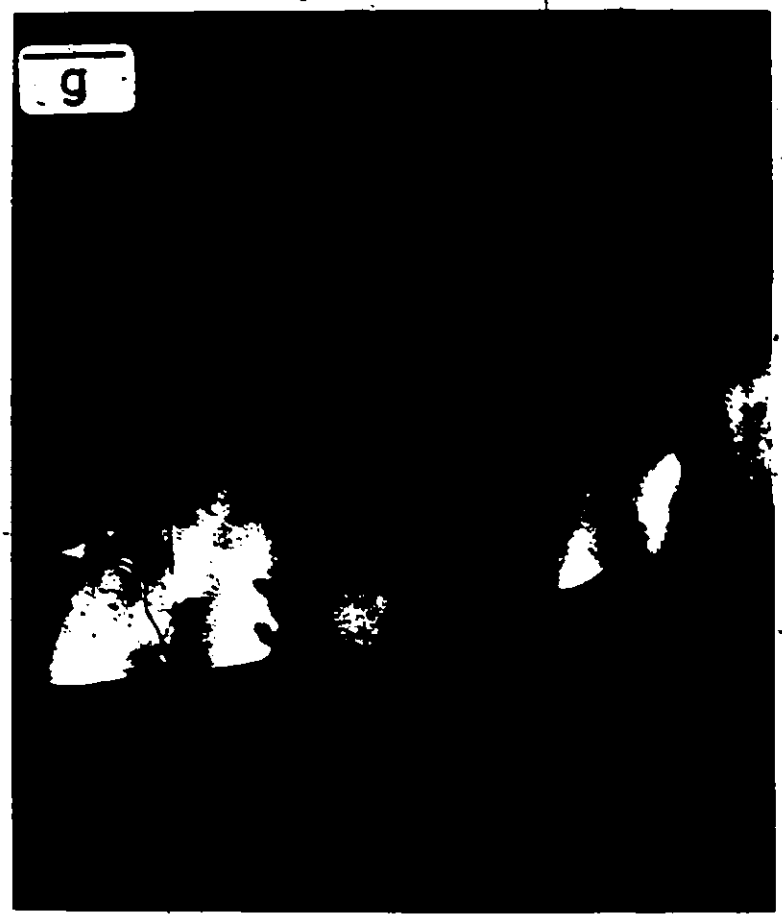

Figure 41. Cu-1.52 wt % Co; 450°C, 25 min. Coherent rod particles are visible (×200K).

Figure 42. Cu-1.52 wt % Co; 500°C, 2 min., coherent rod particles visible as two parallel lines about a line of no contrast (94500×).

Figure 43. Cu-1.52 wt % Co; 450°C, 25 min. Coherent rods and homogeneously nucleated particles in contact with the grain boundary are present (10500×).

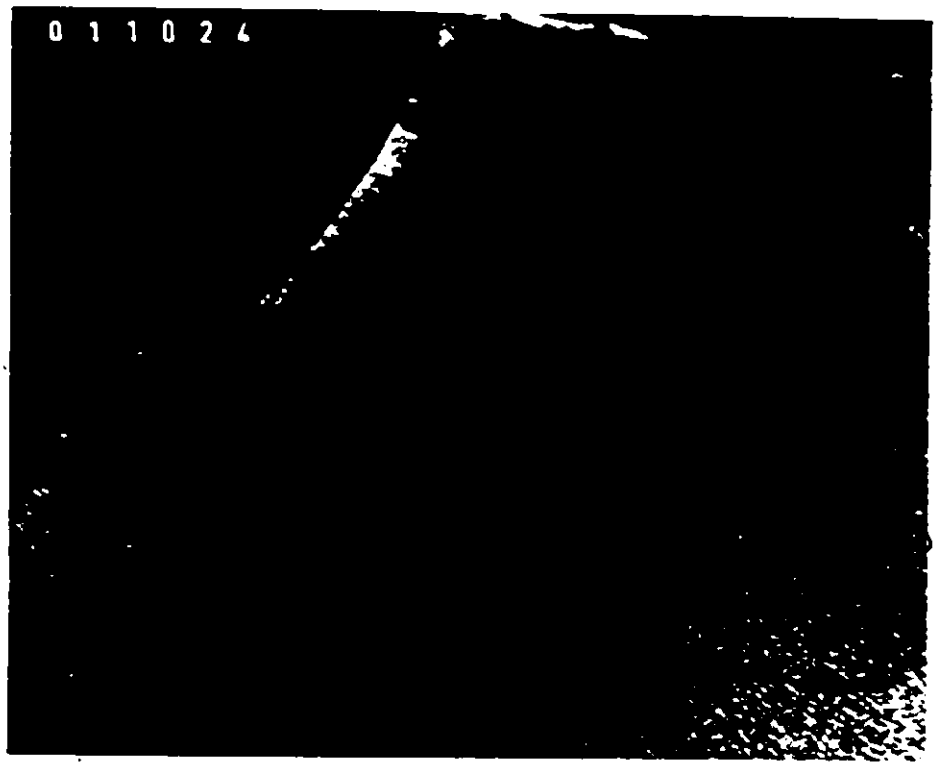

Figure 44. Cu-1.52 wt % Co; 600°C, 2 min. Coherent rods with nomogeneous - particles in contact with the boundary probably stop the growth of rods (¢1250·).

Figure 46. Cu-1.52 wt % Co, 600°C, 2 min. Coherent rods and homogeneous particles in contact with the grain boundary are present (41250×).

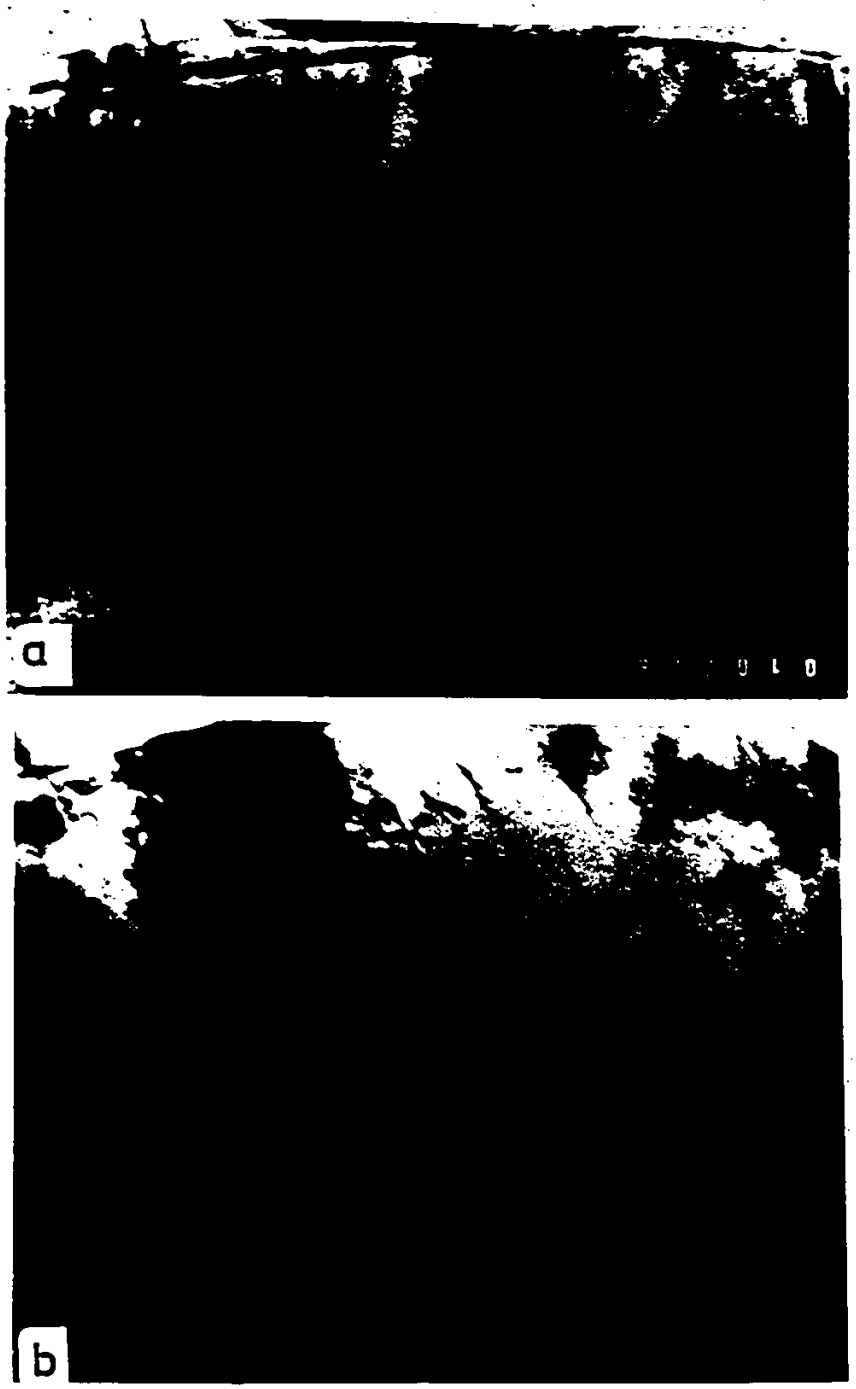

Figure 46. Cu-1.52 wt % Co; 600°C, 2 min. a) Fine coherent rods and local bowing of the grain boundary between rods are visible (31500×), b) the same areas as in a) (65250×).

Figure 47. Cu-2.82 wt % Co; 700°C, 10 min. Coherent rods, some in the process of spheroidization are seen. Some homogeneously nucleated particles between the rods are present (94500×).

Figure 48. Cu-2.82 wt % Co; 700°C, 10 min. Coherent rod particles are visible with two parallel lines of contrast. An especially interesting feature is the evidence of etched out spherical particles in rows as well as of some rods. At the right-hand side the g is at some angle to the rod axis giving a complex contrast of rod particles (65200×).

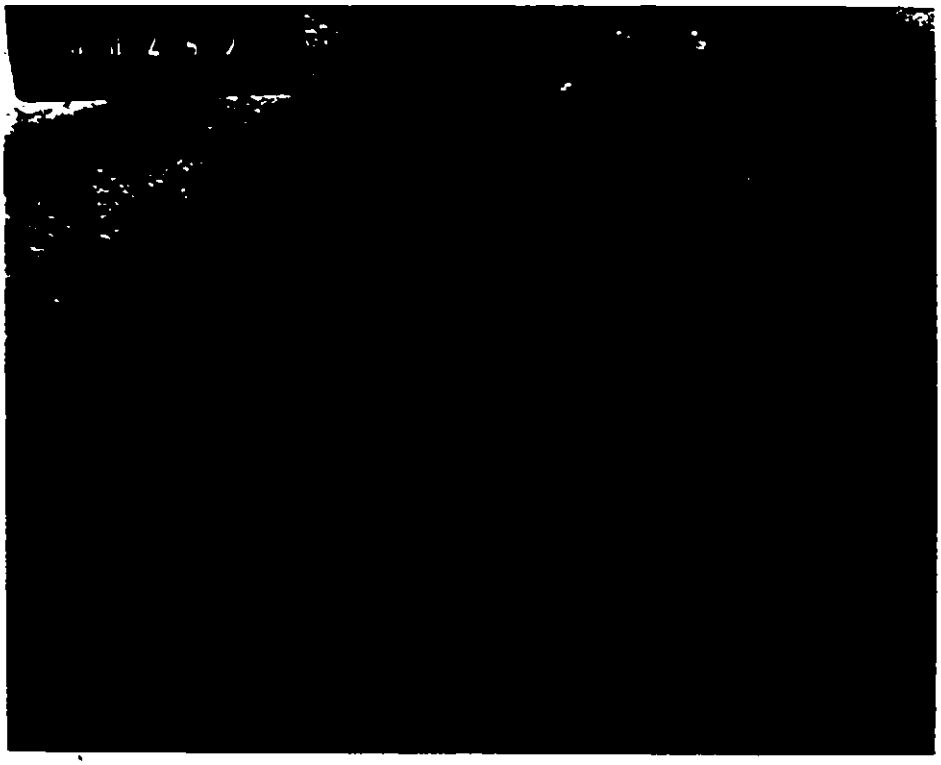

Figure 49. Cu-1.52 wt % Co; 550°C, 20 min. Etched out rod particles with thickness fringes (51000×).

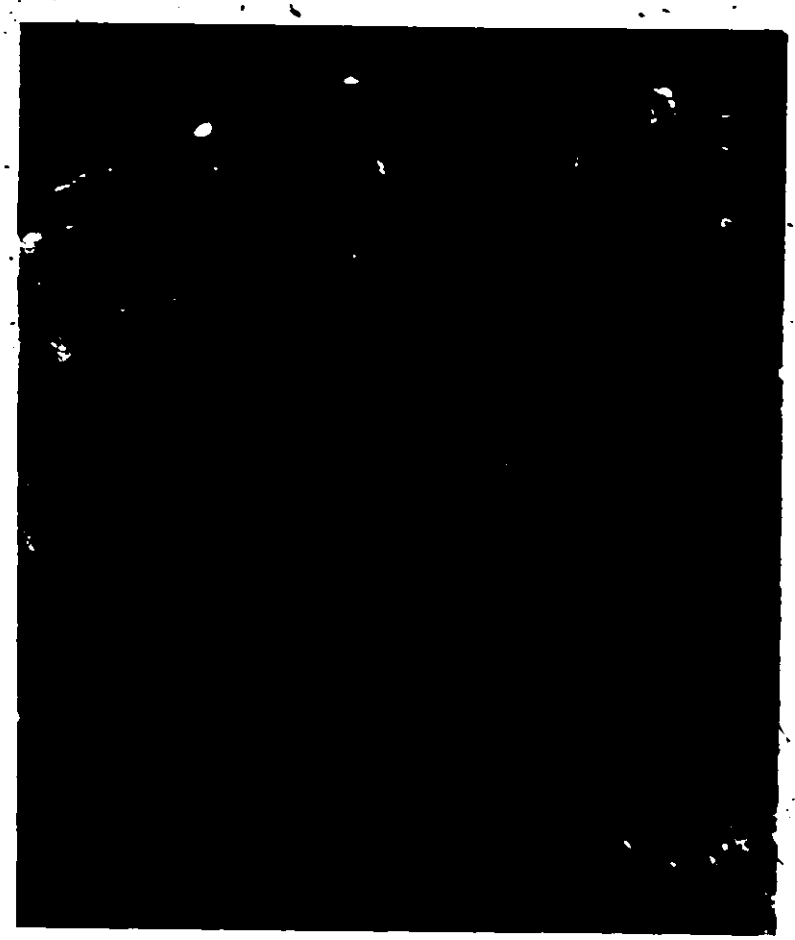

Figure 50. Cu-1.52 wt % Co; 500°C, 20 min. Thickness fringes of etched out rod particles are seen (65250×).

Figure 51. a) Cu-2.82 wt % Co; 550°C, 100 hours. Incoherent grain boundary precipitates and coherent matrix precipitates are visible. PFZ on both sides of the boundary exists. (117000×).

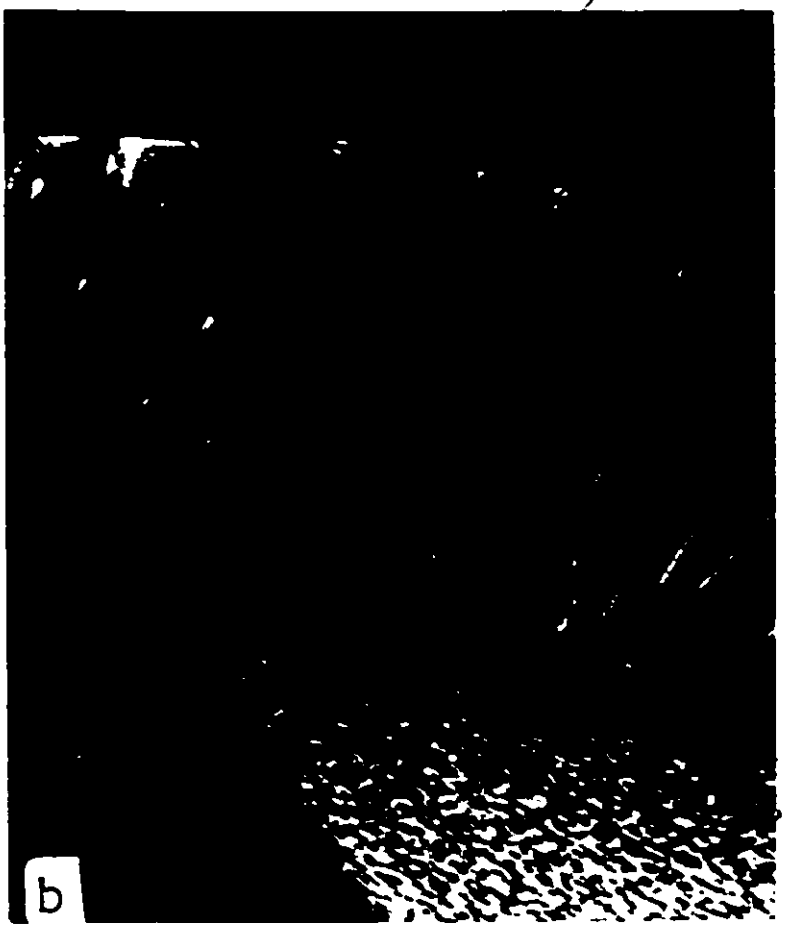

Figure 51. b) Cu-2.82 wt % Co, 750°C, 10 min. Etched out, probably incoherent rods are seen with the line of incoherent particles at the start of the transformation (31500x).

grain boundary reaction front. Figure 44 shows a twin stopping the rod growth, as well as an abrupt change in interrod spacing, S. Figure 47 shows some rods breaking up into spheres. The common feature of the kinetics of the rod instability process being sensitive to the rod radius is clearly visible in most of the micrographs which show rods with local perturbations. Figure 47 suggests that some supersaturation is left behind the moving reaction interface, to be reduced by precipitation of spherical particles between rows. The spacing S between rods may vary by more than a factor of two since the electron microscopy seldom revealed a uniform spacing. Figure 51 shows a seldom observed feature of the presence of incoherent precipitates at the start of rod colonies while Figure 50 shows grain boundary precipitates.

Figure 52 is interesting in that it shows the existence of two regions of different microstructures formed by discontinuous mode reaction, i.e., the microstructure with coherent aligned particles is followed by a region of incoherent particles as demonstrated by the moiré patterns. There is a change in S between these two regions, as well as in the shape of the moving interface, which was almost flat during growth of the coherent rods but which took a more convex shape during growth of incoherent rods.

Another interesting although not common feature is documented by micrograph 53, where dislocation loops around rod particles are visible, indicating a semicoherent interface of rods. The distance between the loops is measured as 120 Å, which agrees with the distance of 150 Å calculated using the known mismatch in Cu-Co alloys.

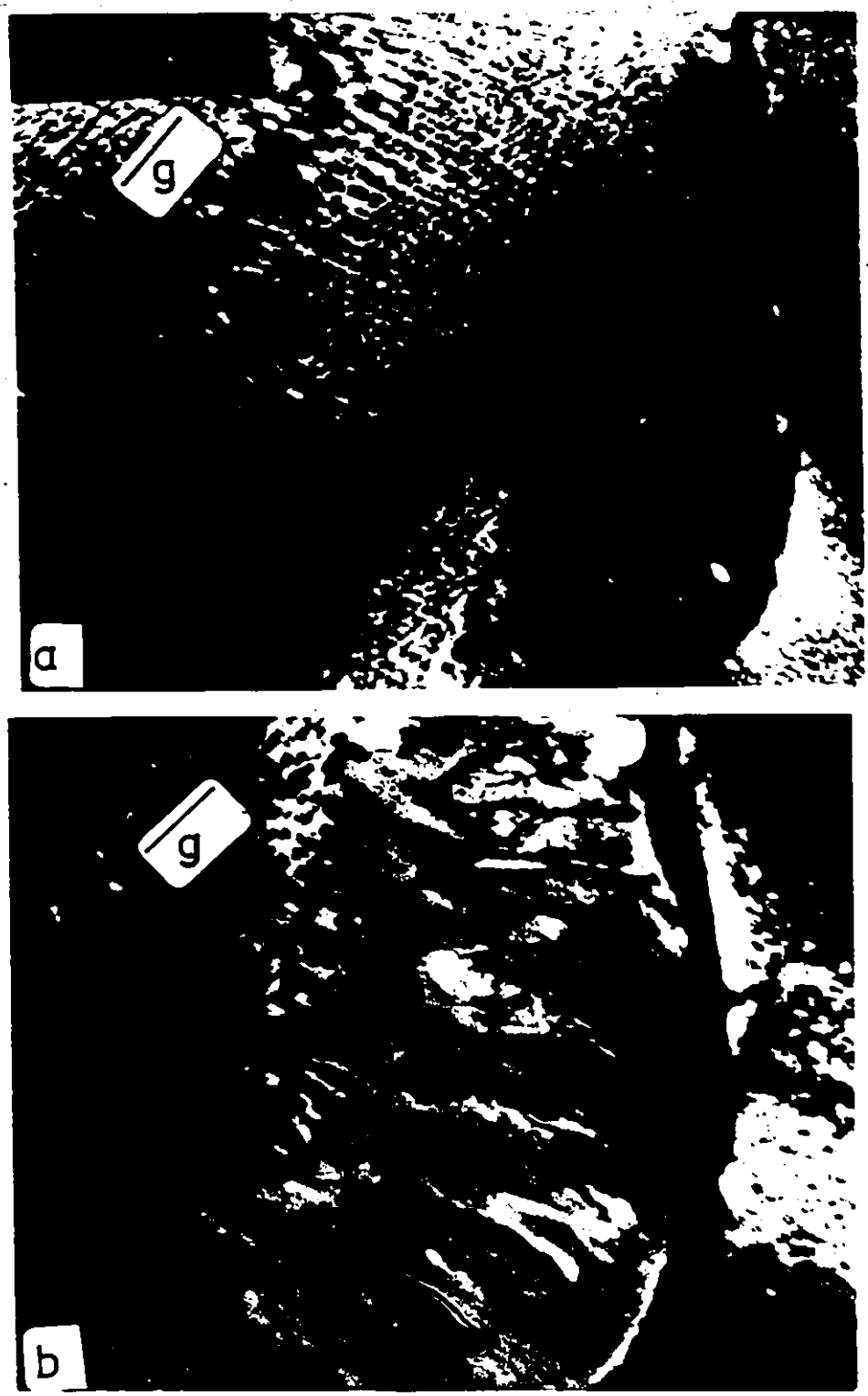

Figure 52. Cu-2.82 wt. % Co, 750°C, 10 min. Few different regions of microstructures are present, 1) homogeneous, statistically distributed coherent particles, 2) aligned rows of coherent particles, 3) coherent rods, and 4) incoherent rods. a) 24750× , b) 41250×.

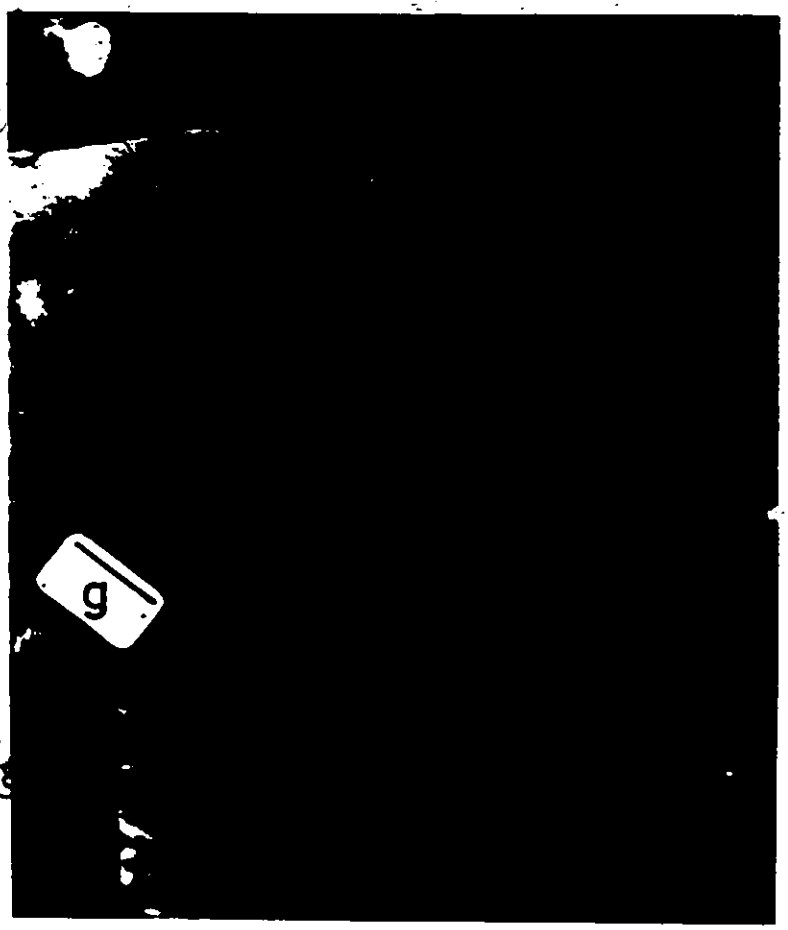

Figure 53. Cu-2.82 wt % Co; 780°C, 10 min. Semicoherent rod particles with dislocation loops around them are visible. PFZ is present in front of rods (53250×)

Figure 54 shows a microstructure characteristic of the samples deformed prior to precipitation heat treatment. The characteristic row microstructure is evident. Particularly worthy of notice is the existence of twins crossing the discontinuously transformed region. The colonies of row particles are neither stopped nor changed in their growth direction indicating that the moving rod-matrix interface was an incoherent high-angle boundary. Figure 55 shows the incoherent matrix precipitates.

Figure 56 shows the effect of the relative grain boundary energies of Cu-Cu and Cu-Co interfaces. It is seen that the Cu-Cu grain boundary emerges from the Cu-Co interface at an angle of about 135 degrees, which indicates that a Cu-Co boundary is of higher energy than a Cu-Cu grain boundary. Figure 57 shows the statistical result of measured angles in the Cu-Co alloys. The maximum is located at an angle of 135°. It indicates the relative relationship of $\gamma_{Cu-Cu}/\gamma_{Cu-Co} \sim 0.8$, thus giving a value of ~ 750 erg cm^{-2} for the energy of the incoherent interface. Table I summarizes the results for the Cu-1.52 wt % Co alloy obtained in this investigation. The measured radii of spherical particles r are considered to be reliable within about 15%. The interrod spacings S, measured as apparent spacings, are marked with asterisks; due to the projection effect in tridimensional foil section, the rods normal to the interface may show the measured spacing S to be 50% less than the true spacing. The values for velocities v are determined as a maximum distance

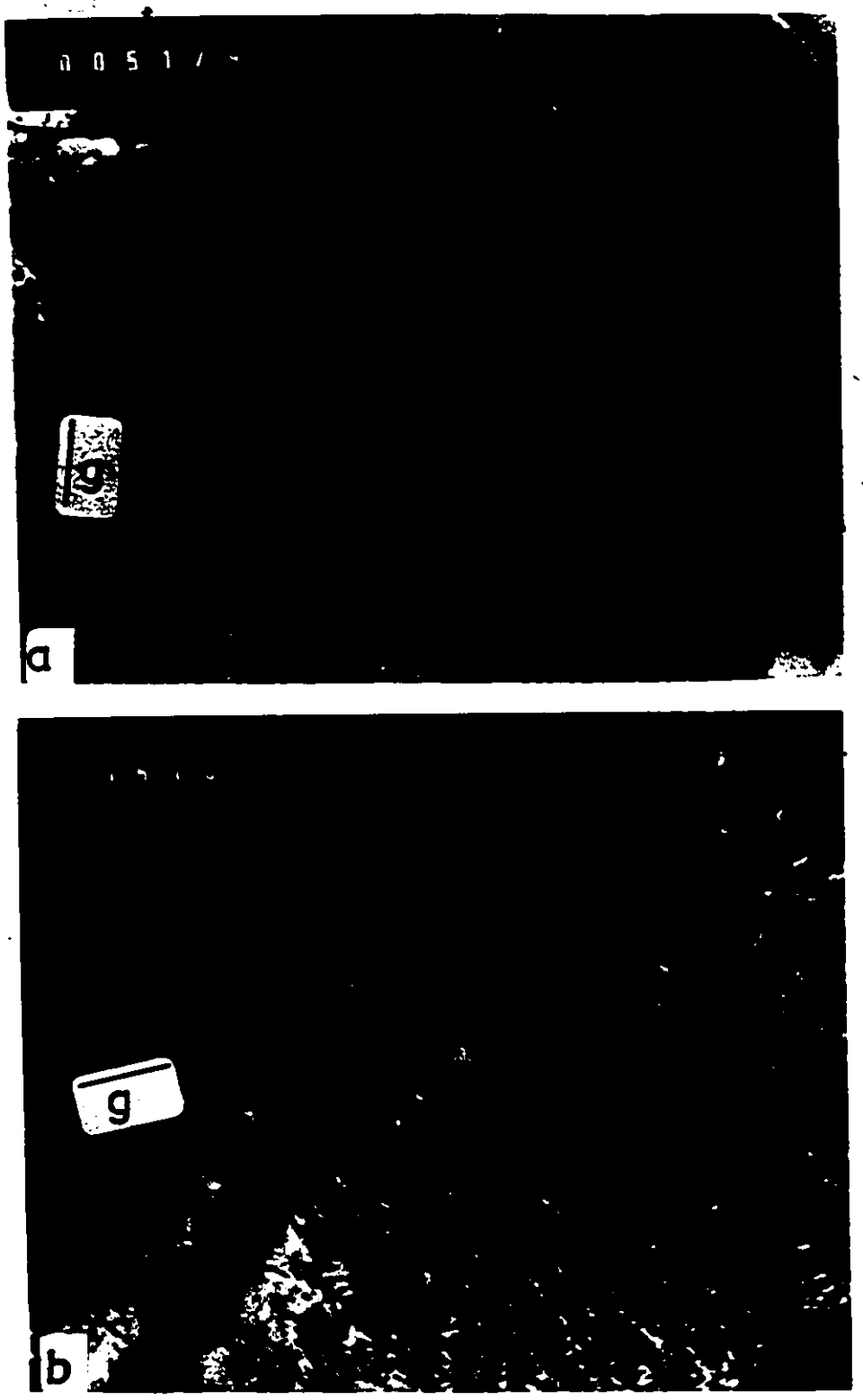

Figure 54. Cu-1.52 wt % Co; 50% deformed, 670°C, 10 min. Rows of spherical particles are present. Some rods are visible. An interesting feature is the presence of a twin not influencing the growth of rows.

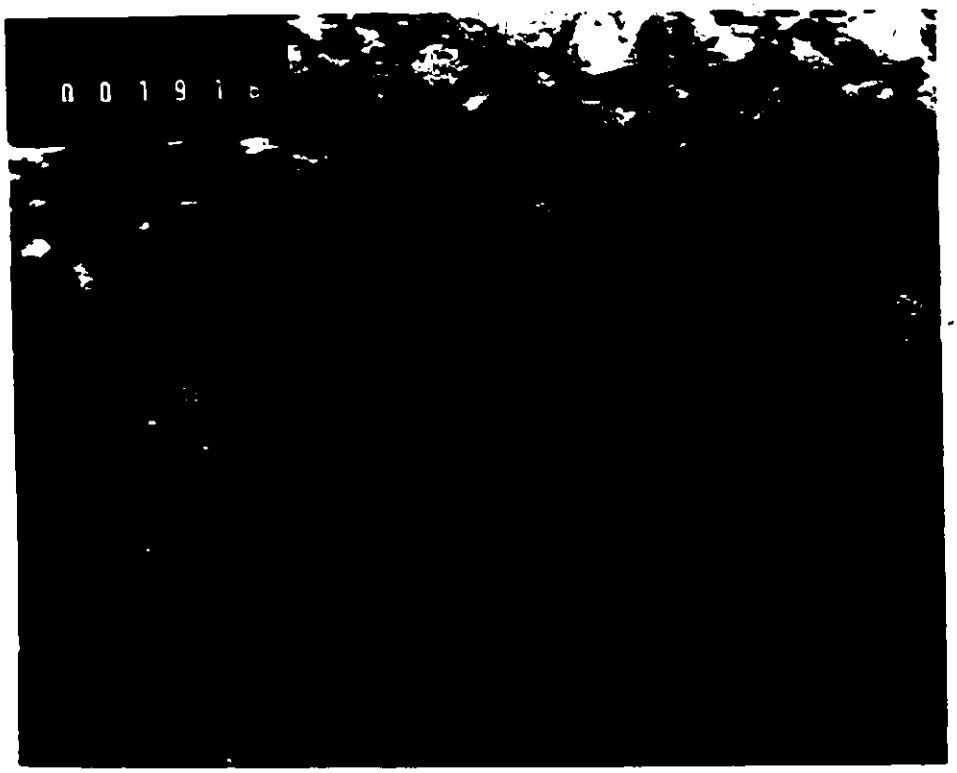

Figure 55. Cu-2.82 wt% Co; 700°C, 2 hours
Incoherent particles with typical moiré patterns, is visible.

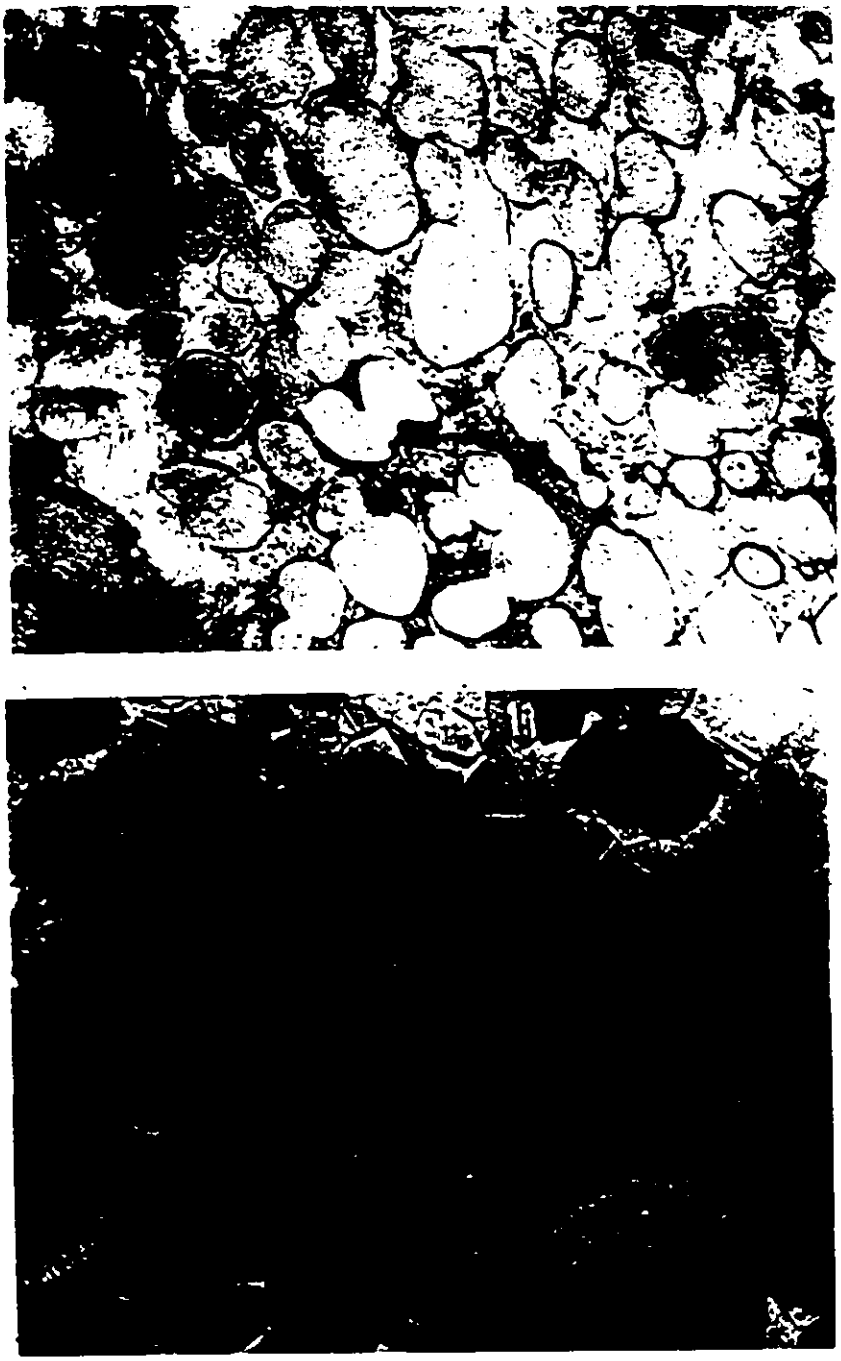

Figure 56. Cu-50% Co, 1000°C, 3 days' a) etched in order to reveal a Co-rich phase, b) etched in order to reveal a grain boundary in the Cu-rich matrix phase (120×).

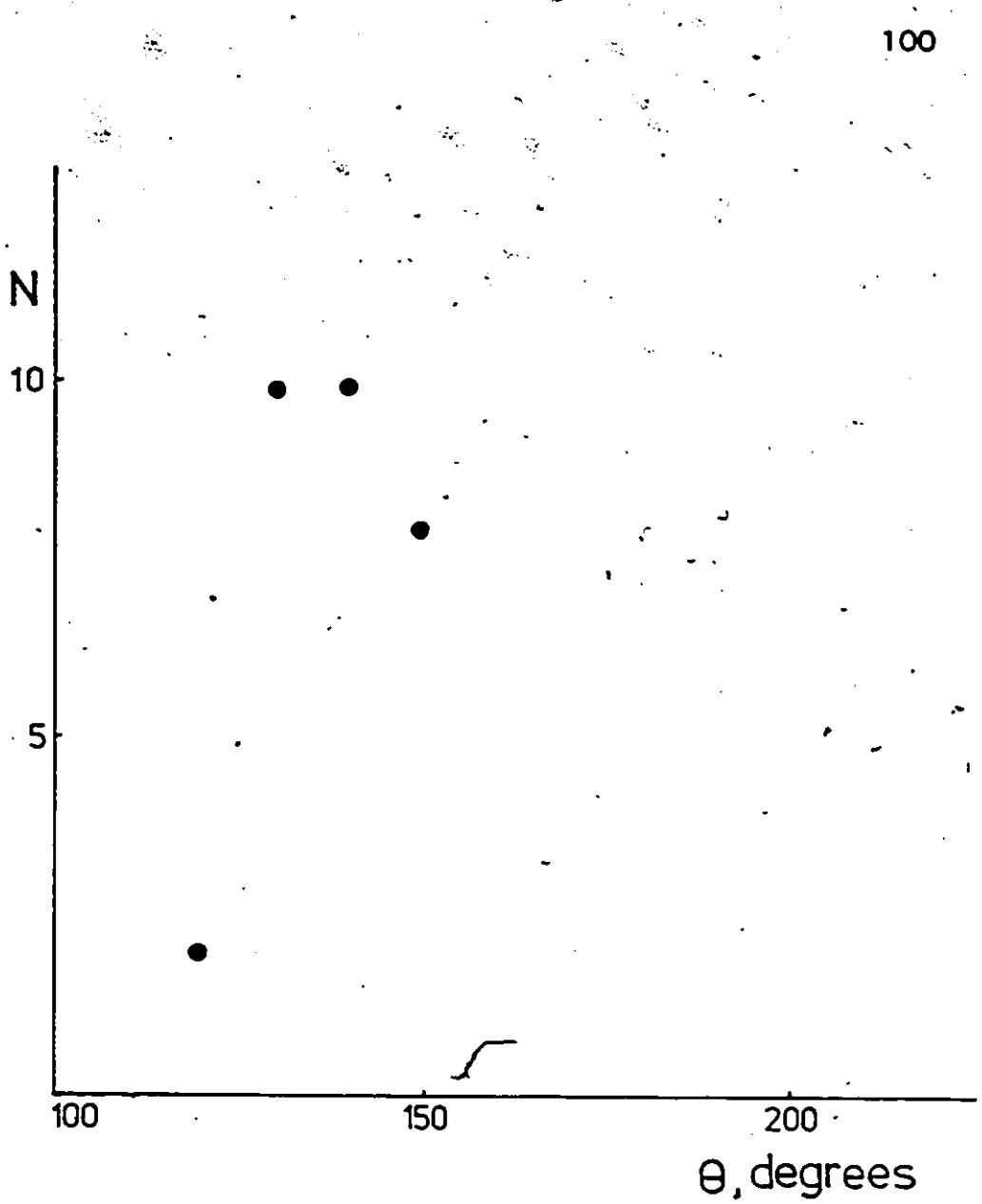

Figure 57. A plot of the number of measured dihedral angles versus dihedral angle in Cu-50% Co.

Table I

Cu-1.52 wt % Co								Cu-2.82 wt % Co							
Temp. (°C)	time (min)	S Å	λ Å	r_{rod} (Å)	r_{sphere} (Å)	PFZ Å	v (cm sec^{-1})	Temp (°C)	time (min)	S Å	λ Å	r_{rod} Å	r_{sphere} (Å)	PFZ Å	v (cm sec^{-1})
450	25	420*		50											
	25	470		20			5×10^{-8}								
	25	390*		45			1×10^{-8}								
	25	570		56			2×10^{-8}								
500	30	530*		25			4×10^{-7}	550	20	350		60			
600	10	590*	210	40	75		8×10^{-7}								
	2	480*		55			1×10^{-6}								
		845	280	30	70		1.5×10^{-6}								
650	10	500*	170		55		1×10^{-6}								
670	10	680					7×10^{-7}								
	10	400*	200		65		9×10^{-7}								
	10	700	220		70	1200	7×10^{-7}								
	10	500*	200	23	57	950	2×10^{-7}								
700	10	520*	280	60	115	1400	4×10^{-7}	700		769		58			1×10^{-7}
	10	630	180		70		2×10^{-7}			690		40			1×10^{-7}
	2	500*	200		90	900	5×10^{-7}			600*					
720	10	570*	380		70		6×10^{-7}			575*		57			2×10^{-7}
	10	570	476		119		2×10^{-7}								
	10	480*	320			2800	1×10^{-7}								
	10	700	250		70		1×10^{-7}	750		690		57			3×10^{-7}
								780		845				1400	1×10^{-7}

*The spacings marked by asterisks are apparent ones; for the others, projection effects could be taken into account and they are therefore true spacings.

of advance of the moving boundary in a given reaction time. The smaller displacements should correspond either to a later start of reaction or to have a growth speed smaller than the largest transformed region. There is an added difficulty in estimating the true growth distance. Measurement should be made in the direction of colonies growth, which, in general, is not normal to the plane of section. However, should the grain boundary from which the colony is growing not be normal to the sectioning plane, no great error is believed to be introduced into the estimate of growth distance. More important in determination of velocity is the uncertainty in the starting and stopping time of the moving interface. Figure 58 is the plot of estimated velocities as a function of temperature for alloy Cu-1.52 wt % Co.

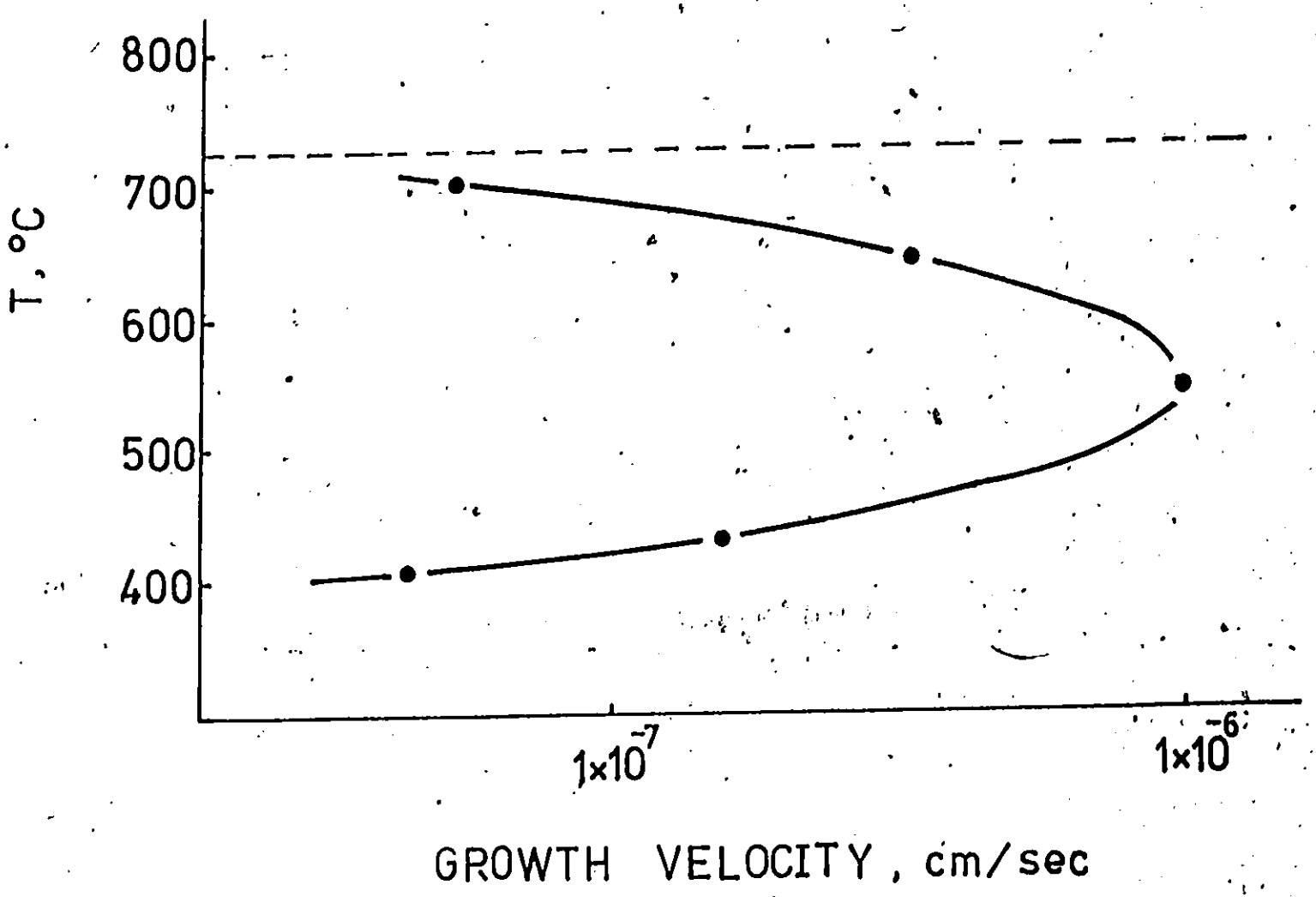

Figure 58. The temperature-velocity dependence in Cu-1.52 wt % Co alloy

CHAPTER 5

DISCUSSION

5.1 Preamble

In the account of the experimental findings presented in Chapter 4, it was concluded that discontinuous rod formation is the dominant type of heterogeneous precipitation reaction in this system. This was proved by direct observation at lower temperatures and supported by indications of apparent rod instability effects at higher temperatures and, as will be shown, it is consistent with considerations of the kinetics of the rod spheroidization process. The discontinuous rod precipitation reaction is the first reaction encountered in the temperature and composition regimes investigated, and column formation is connected with and derived from this discontinuous reaction product as a consequence of rod instability. Consequently, two main questions should be answered concerning:

i) the formation of rows, as a consequence of the existence of prior rods, and

ii) the discontinuous reaction, its mechanism and kinetics.

In the remainder of this chapter a discussion of the discontinuous rod precipitation will be presented along with a discussion of an alternative mechanism of column formation as envisaged by the author. The result favours the rod instability mechanism.

5.2 Spheroidization of Rods

In section (2.2), we have already explored the regime of the rod → row transformation according to simple thermodynamic considerations with the result that the columnar row structure can have a smaller integrated surface energy than the rods from which it was formed within some range of size r, and distance between them in a row, λ. From the experimental data we can take some pair of values for the particle size r and distance λ and, by comparison with the computed graphs (Figure 20) test the possibility of occurrence of the rod → row transformation reaction. We have chosen a particle radius of 70 Å and a distance λ of 220 Å as representative of values obtained from the present experiments. This point (A) was plotted in Figure 20 and, since its location was close to the dividing curve of equal surface areas for the two microstructures, a decision could not be made easily. However since the rod instability behaviour is extremely sensitive to the initial rod radius, which in turn is responsible for the dimensional parameters r and λ, one should be very careful in deciding whether the transformation is possible on this basis. The values for λ and r were taken from micrographs where the columnar structure was the only microstructure present.

As a matter of fact, spherical particles in rows could conceivably have been the product of a coarsening process, in which case the initial distance λ would be, say, one half that

observed (approximately 100 Å). The corresponding particle size would be about 56 Å, which would yield the point B shown in Figure 20. However, the coarsening time of 56 Å particles to 70 Å was estimated to be about 1.2 hours at 700°C. This is an exceedingly long time compared to the experimental time of reaction (at most 10 min.). Hence, the Ostwald ripening of initially formed spherical particles is ruled out as a possible stage in the total rod → row transformation.

There is a further possibility to be considered: In all discontinuous precipitation reactions involving grain boundary diffusion, there will be composition gradients in the matrix left behind the moving α_0/α interface. Thus, one expects some free energy (supersaturation) stored in the product matrix phase between the rod particles. Capillarity would lead to additional storage of supersaturation, and these two terms would eventually lead to thickening of the precipitated rods or, if spheroidization took place, to the growth of the resultant spheres. A further growth will occur only if the spherical particle has significantly smaller curvature ($\frac{2}{r}$) than the rod ($\frac{1}{r_0}$) since the sphere can then increase its radius (decrease its curvature) and consequently the diffusion potential for growth. If such fine rods were initially precipitated, their instability would lead to a smaller radius of spheroidized particle with a spacing λ, which would shift the system point in Figure 20 to the region where the rod → row transformation is energetically favoured. As an example, a rod radius of about 20 Å will give (by spheroi-

dization) a particle of approximately 40 Å radius, and a corresponding point (C) in Figure 20 which satisfies the conditions required for rod spheroidization. The observed particle radius could then result from further growth.

As already mentioned in section 1.1, there exists in the literature[16] a suggestion of rod spheroidization in Cu-Co alloy, accompanied by a micrograph of rows of Co particles. The measurements of radius of spherical particles r and distance λ from this micrograph are plotted in Figure 20 as point D which falls far inside the region where the rod → row transformation is favoured.

Finally, the kinetics of rod spheroidization was studied. There are two possible kinetic paths by which the rod can transform into a string of spherical particles; One involves the development of infinitesimal perturbations on an infinitely long rod, and yields for the time of spheroidization:

$$t = \frac{r_0^3 \, \Delta r \, RT (C_\beta - C_\alpha)}{C_\alpha \, D_v \, V_m \, \gamma \, \Delta k \cos kz} , \qquad (19)$$

where r_0 is the initial, unperturbed radius of the rod, Δr is the perturbation, C_α and C_β are the equilibrium compositions of the matrix and rod, respectively, Δk is the amplitude of perturbation, D_v is the volume diffusivity, V_m is the molar volume, γ is the surface energy of rod and $k = 2\bar{u}/\lambda$ where λ is the wavelength of the perturbation and z is the axis along rod, R and T having their usual meanings. The other path takes into account the end effects of semiinfinite rods and yields a much shorter time for

detachment of a spherical particle in the form of:

$$\tau = \frac{r_0^3 \, R \, T}{C_0 \, V_m^2 \, D_v \, \gamma} \quad , \qquad (20)$$

where C_0 is the composition of the supersaturated matrix, and the other symbols are the same as in equation (19). In the case of detachment, one should sum all τ's of detachment of a single particle in order to get the integral time for spheroidization of the rod as a whole. If steady-state rod formation is assumed, τ becomes a measure of the distance behind the grain boundary over which rods might exist. If one assumed the initial existence of a long rod, $\Sigma\tau$ as the total time would not necessarily be less than the time t (equation (19)) leading to simultaneous breakdown of the long segment. As an example, the spheroidization time t (equation (19)) of a rod of 6000 Å in length and radius r_0 of 15 Å at 700°C is 8 minutes, while τ (equation (20)) will be only about 15 sec for end detachment, but $\Sigma\tau$ would be 15×6000/200 i.e. about 8 min for λ = 200 Å.

The end detachment process is very attractive, theoretically at least, because this allows a quasi-steady process to occur. The rod is laid down at the reaction front, and spheres detach regularly from the end, leaving a constant length of perturbed rod attached to the interface and requiring only a short time τ for sphere detachment. For example, at 700°C, for $v = 4\times10^{-7}$ cm/sec^{-1}, one would expect that 30 Å diameter rods would have spheres detached from their ends in approximate-

ly 7 seconds. Hence the length of rods at the interface would be about 240 Å. Similar calculations for other temperatures suggest that the end detachment mechanism seems more likely to be the process of rod breakdown in most of the cases studied. For example, at 600°C, τ for a 15 Å radius rod is 2 minutes while at 500°C, it is almost one hour. This is in agreement with the absence of experimental evidence for rows at temperatures lower than 600°C.

Whatever the mechanism of rod spheroidization, rod instability or end detachment, the experimental conditions (temperature and time reaction) are always in agreement with the time calculated on the basis of the models for rod spheroidization. However, one should note the strong dependence of τ on rod radius when considering the rate of rod instability. This gives a marked local sensitivity of the reaction from one rod to the next, or even along a single rod, and can help to explain those structures in which rods and rows are seen to coexist (Figure 28). Table II shows some of the calculated times for different temperatures and rod radii. Obviously, the coexistence of rods and rows is in fact a quite common feature of the reaction.

5.3 Model for Non-steady Mechanism of Discontinuous Reaction

There is an alternative mechanism of row formation as envisaged by the author which is based on a non-steady state grain boundary movement. One reason for discussing it is to eliminate it as a practical mechanism for our experimental conditions.

TABLE II

T (°C)	τ(sec) / r_o=60 Å	τ(sec) / r_o=30 Å	τ(sec) / r_o=20 Å	τ(sec) / r_o=15 Å
700	4.0×10^{2}	5.3×10	2.0×10	6.0
600	8.0×10^{3}	1.0×10^{3}	3.0×10^{2}	1.2×10^{2}
500	2.8×10^{5}	3.9×10^{4}	1.1×10^{4}	4.8×10^{3}

In this model it is proposed that the grain boundary is pinned by the growing particles and interacts with them (i.e. exerts a force on the particles) as it moves under the influence of some driving force. This situation is closely approximated by a treatment due to Ashby and Lewis[82,83]. The moving grain boundary would occupy successive equilibrium positions, determined by the capillarity conditions until the critical position would be reached where the particles exert a maximum pinning force. After this no equilibrium positions can be attained and the boundary would break away from the particles. There is a relationship between the break-away distance, i.e. interparticle spacing λ and the driving force, P, for a given distance between the particles S and a given grain boundary surface energy, γ_b:

$$\lambda = \frac{S^2 P}{8\gamma_b} . \qquad (21)$$

Hence, without considering the nature of the driving force acting on the grain boundary, the maximum pinning force, depending on the size of the particles, can serve as a test for the driving force present, since,at the moment of break away of the boundary from the particles, the driving force is equal to the pinning force. The maximum pinning force without including the nature of the particles* could be estimated from the formula:

---

* The nature of the particles enters the calculation through the angle α at which the boundary meets the particle under the assumption of local equilibrium of boundary surface tensions at the joining point.

$$P^{p} = N_s \bar{u} r \gamma_b \qquad (22)$$

where N_s is the number of particles per unit boundary area (about 3×10^{10} cm^{-2} in this case), r is the radius of the particle at the moment of break away (about 70 Å) and γ_b is the surface free energy of the grain boundary. The maximum pinning force is estimated to be about 1×10^{7} erg/cm^3 which in turn gives the breakaway distance λ (equation (21)) of about 10 Å. This calculated distance is, of course, much too small. Ashby and Lewis note that their calculated grain boundary shapes at breakaway are generally rather flat and curved only locally close to the particles. Hence, for this and other reasons, one cannot accept the idea that the row formation is based on a non-steady state discontinuous precipitation reaction.

5.4 Mechanism of Discontinuous Rod Formation in Cu-Co Alloy System

(a) Preamble

On the basis of the previous discussion, it is concluded that the direct experimental evidence for the presence of coherent rods, the self-consistent set of dimensional parameters for the process of rod spheroidization supported by the kinetics of spheroidization (i.e. the measured interparticle spacing λ, a corresponding derived radius of rod particles r_0 and the time of the spheroidization process τ_{r_0}), together with the failure of the non-steady state model, are fully consistent with the discontinuous rod formation reaction. In subsequent sec-

tions nucleation of coherent particles at the grain boundary, thermodynamic aspects of rod precipitation, driving forces acting on the grain boundary during rod colony growth as well as the kinetics of reaction will be considered in turn.

b) Nucleation of rods

We will treat the formation of rods by first considering the nucleation of coherent particles at high-angle disordered grain boundaries and then discussing the evolution of such particles into rods. This is appropriate since neither the shape of the critical nucleus nor its interaction with the grain boundary is determinable with the electron microscopic techniques employed.

Nucleation theory requires that a nucleus be of such a shape that it requires a minimum amount of interfacial free energy per unit volume in the absence of strain energy. If the two phases are fully coherent, nucleation at a grain boundary would hardly be expected in view of the small activation barrier for homogeneous nucleation. However, the volume strain energy term, which acts to increase the activation barrier for homogeneous nucleus formation is proposed in this study to play a role. We suppose that the grain boundary nucleation event is favoured precisely because the boundary cannot support or transmit a shear stress to the grain with which the precipitate is not oriented, so that the strain energy per unit volume of precipitates is reduced below its homogeneous value, and the consequent formation of a high-energy disordered facet lying in the grain boundary plane is favoured.

The shape of the critical nucleus has been obtained by applying Cahn and Hoffman's analysis for the equilibrium shape of a grain boundary precipitate. In the case of a Cu-Co alloy, the coherent interfacial free energy of the Co-particles is taken to be isotropic and the equilibrium shape will therefore consist of spherical segments so that the shape of the particle nucleated at the grain boundary can be constructed from truncated sections of isolated spherical segments. The construction, shown in Figure 59, is simply performed by displacing the centers of the two nuclei with vectors $\vec{\xi}_1$ and $\vec{\xi}_2$ corresponding to the interfacial coherent boundary energy of Co particles in a Cu matrix (200 ergs cm^{-2}) and the grain boundary energy of Co incoherent interphase (assumed to be $\sim$ 750 ergs cm^{-2}) by a vector $\vec{\xi}_b$ corresponding to the interfacial free energy of Cu matrix grain boundary (600 ergs cm^{-2}). The equilibrium shape is shaded and consists of the regions of the overlap, and the equilibrium dihedral angles are also indicated.

The value of the high-energy facet of Cu-Co interface was estimated as follows: From the work by Servi and Turnbull[68], the interfacial surface energy between coherent cobalt-rich particles and the copper solid solution of 200 erg cm^{-2} is confirmed to be mostly the contribution from the chemical part of the interfacial energy. Therefore, the coherent Cu-Co interfacial energy is considered to be of the "chemical" type of interface. The incoherent Cu-Co interface must include the geometrical part as well. However, since the Cu-Co incoherent grain boundary is a

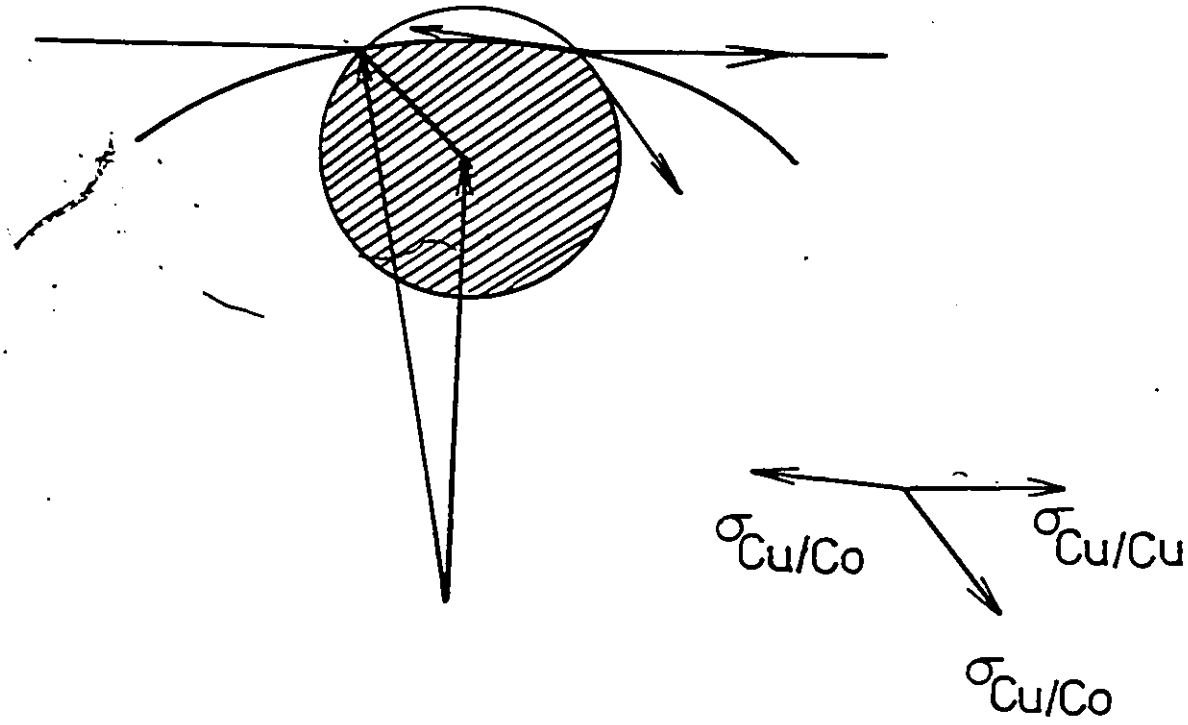

Figure 59. The equilibrium nucleus shape of a grain boundary precipitate

high-disordered type of interface or "geometrical" type of interface, we can assume then that the incoherent Cu-Co phase boundary is the sum of these two parts, giving a value of about 800 erg cm^{-2}. In section 4, we have confirmed experimentally a value of 750 erg cm^{-2} as a reasonable estimate.

The kinetics of nucleation in the Cu-Co system is known to be fast for general precipitates. By using the formula[51]

$$\tau_n = \frac{kTn_k^2}{\Delta G_k^0 \beta_k}, \qquad (23)$$

where ΔG_k^0 is the activation barrier for nucleation (4.5×10^{-12} erg in our case), β_k is the frequency factor including the diffusivity due to the particular transport mode of solute to the critical nucleus ($\sim 6\times10^{2}$ sec^{-1}), n_k is the number of atoms contained in the critical nucleus (22 atoms) and k and T are constants with their usual meanings, a nucleation time of 0.02 sec was obtained if only volume diffusion transport was considered, i.e. that the nucleus was formed solely by addition of solute atoms to the coherent spherically curved interface. If the grain boundary aids the nucleation process by supplying the solute atoms along it, τ_n is 10^{-5} sec.

However, since both τ's, with and without the aid of grain boundary diffusivity, are less than 0.1 sec, the difference is expected not to be crucial.

Instead, we conclude that the growth of general precipitates in front of the moving boundary reaction is slower so that

the amount of the driving force lost by its occurrence is initially small, and the discontinuous precipitation of rods takes this advantage in the early stage of the reaction. This point will be explored in more detail as follows.

The experimental results show the radius of the particles in columnar arrays to be approximately 60 Å and the spacing between them to be about 200 Å. Supposing that the reaction is a consequence of rod instability, the spacing of 200 Å would result if the particles were initially about 40 Å in radius (the 60 Å particles are envisaged to be the result of subsequent growth processes). Hence, starting with spherical particles of 40 Å radius, formed by rod spheroidization, the initial radius of rod particles turns out to be about 20 Å. By considering the two reactions to nucleate essentially simultaneously, one in the matrix, the other at the grain boundary, and the latter one to be about two orders of magnitude faster than the first one, we conclude that rod particles have formed by a discontinuous coarsening process.

However, as the reaction proceeds with time, the supersaturation in the matrix ahead of the growing rod particles will be reduced due to the precipitation of the homogeneously nucleated particles in front of the moving interface.

Thus, in the early stage of precipitation of the Co phase, both homogeneous and discontinuous reactions take place simul-

taneously but, due to the much faster discontinuous reaction, most of the supersaturation will be used up by discontinuous rods while, in the later stage, less and less supersaturation will be available and, finally, the discontinuous reaction will stop.

This situation is thought to be the origin of the wide precipitate free zones sometimes seen in front of the grain boundary (Figure 35), which are of the same order as the volume diffusion distance ($\sim \sqrt{Dt}$, i.e. $\sim$ 1000 Å at 700°C). However, at 500°C and 600°C there is no evidence of such precipitate free zones (Figure 45), suggesting that the discontinuous coarsening process continues for a longer time at these temperatures.

c) Genesis of the discontinuous precipitation reaction

The mechanism of formation of rod discontinuous precipitates in the Cu-Co alloy system, which will be proposed in this section, is based on the existence of a high diffusivity path for grain boundary precipitates which provides the origin of its evolution into rods through the balance of surface tension forces at the three-phase junction.

Immediately after the nucleus is formed, the diffusivity along the high-diffusivity incoherent nucleus interface, will cause the development of a "lump" of precipitate into the neighbouring matrix grain. Assuming that the balance of surface tension forces holds during this process, the grain boundary

will bow towards the receding grain (convex towards the growing grain) (Figure 60). By further growing of the particle while still balancing the interfacial energies at the three-phase junctions in the reaction front, the growing precipitate will be converted into a rod-like particle, pulling along with it the grain boundary (Figure 61). Hence, the chemical free energy is acting on the rod particle causing its growth, while the connecting α_0/α grain boundary segments are pulled along to keep the interfacial balance at the three-phase junctions. Thus the driving force acting on the grain boundary comes from the balancing of interfacial energies. This mechanism is quite similar to that of the Tu and Turnbull model[22].

Since the mechanism proposed originates from the nucleation of the grain boundary precipitate, it would be expected, according to Aaronson and Aaron's detailed treatment[23] that this particular type of nucleus shape with $\gamma_{\alpha\beta} > \gamma_{\alpha\alpha}$ would prohibit the development of the discontinuous reaction.

Evidently, this is not a general argument; we have shown that the grain boundary can bow toward the precipitates and still lead to the development of a discontinuous product.

d) Thermodynamics of rod precipitation

There is an aspect of rod-like precipitates different from their lamellar counterpart which involves thermodynamics and which merits further discussion.

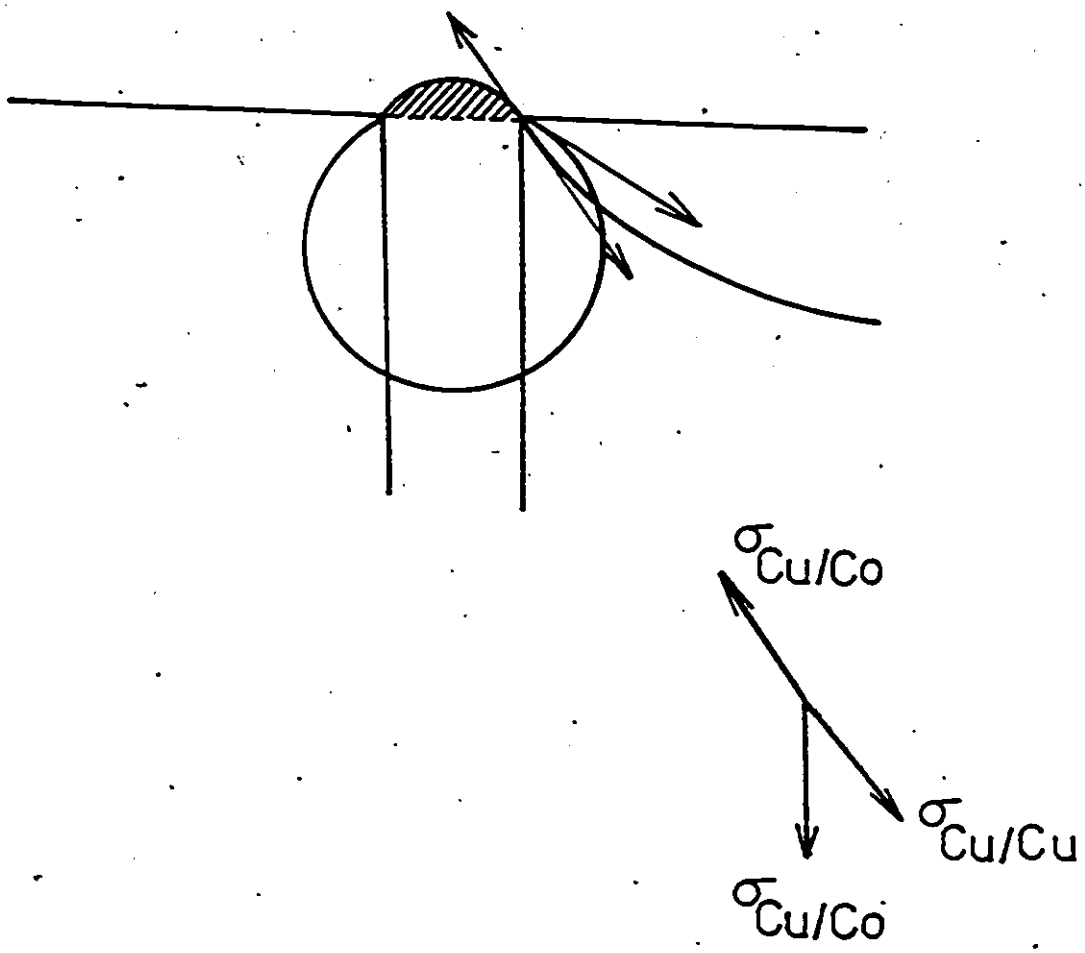

Figure 60. Development of grain boundary nucleus into rod morphology

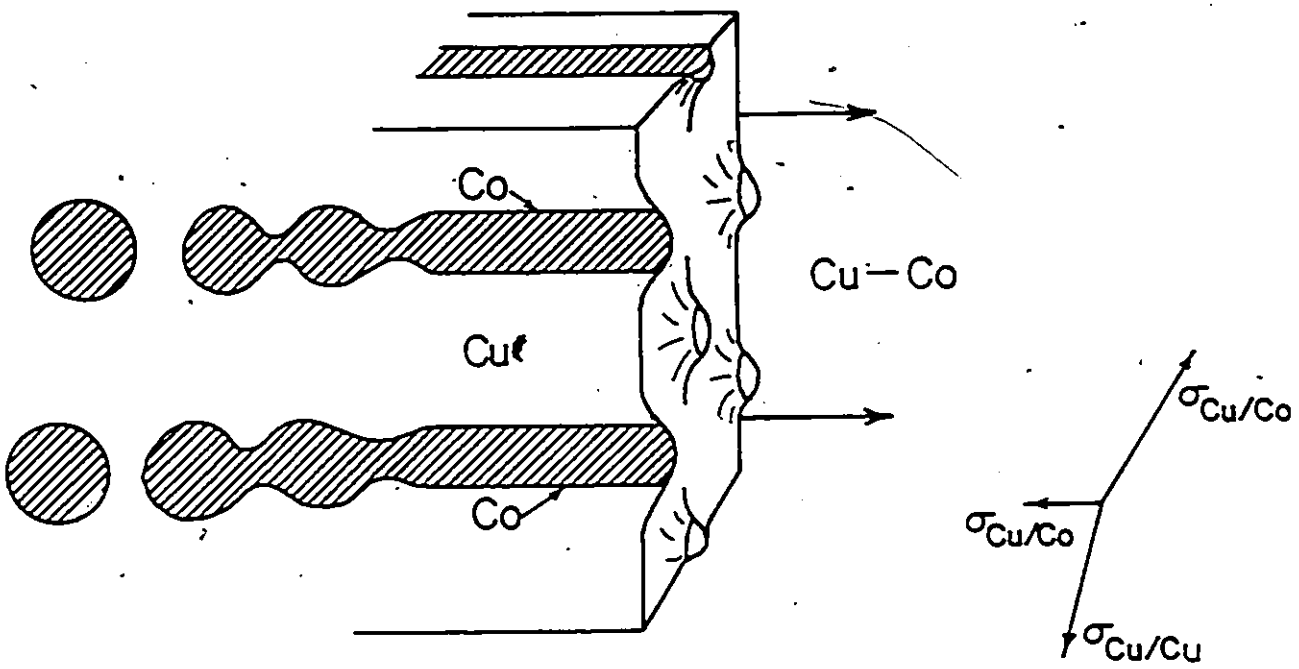

Figure 61. Schematic representation of formation of rows of particles

In the case of rod morphology, there exist two radii of curvature: r, for the interface which contacts the parent matrix grain, and r_0, for the interface imbedded in the product matrix phase. (In the lamellar case, there is only the radius r present due to plane interfaces of the β phase surrounded by the depleted matrix.)

Figures 62a and 62b are hypothetical free energy and phase diagrams. There is a free energy available to drive the precipitation reaction, ΔG_0, of an alloy of composition C_o. If a spherical particle of radius r is formed, the free energy decrease will be ΔG_r. Further decrease of free enegy will be obtained by formation of rod particle of radius r. Therefore, the free energy, $\Delta G_{realized}$, is the driving force for rod-like particle formation.

If the rod particles are assumed to be in equilibrium with the matrix, then the volume fraction realized will be determined by the composition of rods of radius r, C_{rod}, and the spacing S between the rods will also be determined. For a given rod radius r, the volume fraction is $N^{rod}\bar{u}r^2$ where N^{rod} is the number of rods per unit area correlated to the spacing between S, as $N^{rod} = \frac{1}{S^2}$, so that the volume fraction becomes:

$$V_f = \frac{\bar{u}r^2}{S^2} . \qquad (24)$$

In our case, by taking the equilibrium composition to be that given by the phase boundary at 700°C, the volume fraction would be 6×10^{-3}, which would result in a spacing of about 480 Å for

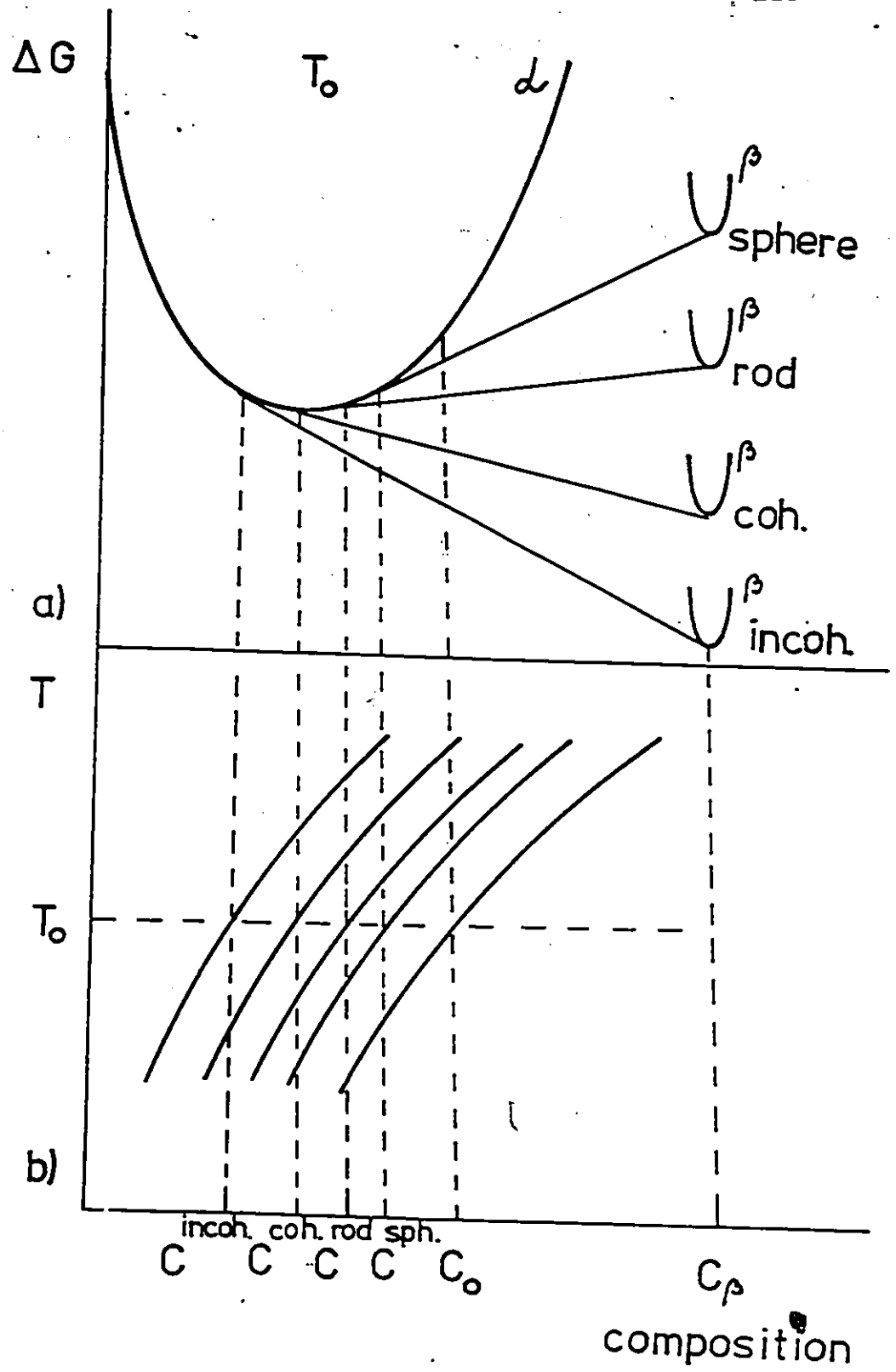

Figure 62. a) Hypothetical free energy diagram and b) corresponding phase diagram in the case of rod-like precipitation

an assumed rod radius of 20 Å. However, the experimentally observed value for S is about 600 Å which for the same radius of rod, gives a volume fraction of 3.5×10^{-3}. This value is the expected one if the Gibbs-Thomson effect is considered in determining the composition in equilibrium with the rod particle. This suggests that, in our experiments, rods are formed in local equilibrium with the depleted matrix, as determined by the curvature of the precipitates. The assumption that the matrix is essentially uniform between rods will be justified later.

In summary, the rod-like precipitate morphology exhibits two mutually dependent variables, the radius of rod, r and the interrod spacing, S. The formation of rods of a particular radius r, fixes the volume fraction through the Gibbs-Thomson effect, thereby determining the maximum free energy available for the discontinuous reaction.

Because of the small radius of the rods, there will be some residual supersaturation (relative to infinite radius particles) left in the product matrix, $\Delta G_{retained}$.

e) Driving forces acting on a moving grain boundary

Based on the premise that discontinuous precipitation of coherent rods in the Cu-Co alloy system is a rather general phenomenon, we will proceed with a discussion of the driving forces on the $\alpha_0|\alpha$ interface, here seen as a crucial concept in the application of the theory of discontinuous precipitation.

According to Hillert as reviewed in section 1.2, at least two kinds of driving forces could be operative in some systems exhibiting discontinuous reactions:

i) chemical force and

ii) coherency force.

We will discuss the possible cause of rod formation in Cu-Co alloys by considering these two forces; in addition, a "pulling force" will be invoked as a consequence of the balance of interfacial forces acting at the three phase junction. The available velocity and diffusion data will be used in deciding what kind of driving force operates in a Cu-Co alloy.

i. The chemical driving force

As reviewed in section 1.2, the chemical force acting on the reaction front in discontinuous precipitation arises from the fact that the grain boundary transport is much faster than volume diffusion [(due to the fact that D_b (boundary diffusion coefficient) is much greater that D_v (volume diffusion coefficient)], so that there exists a concentration step at the moving grain boundary. This results in a force (available to move the boundary) of the form:

$$P^{chem} = f \frac{\Delta G^{diff}}{V_m} \qquad (25)$$

where

$$\Delta G^{diff} = \frac{RT}{V_m} \frac{(C_o - C_e)^2}{2C_o} \qquad (25a)$$

if dilute solid solution is assumed, C_0 being the composition of supersaturated alloy, C_e its equilibrium composition given by a phase boundary; for the rod formed of radius r, the equilibrium composition, is given by C_{rod} in Figure 62b.

The fraction of this force available for boundary migration is estimated as

$$f = 1-\exp(-\frac{vb}{2D_v}), \qquad (26)$$

where v is the growth velocity, b is the atomic distance (about $\sim$ 5 Å) and D_v the volume diffusion coefficient[77].

In our case, at 700°C, $v \sim 1\times10^{-7}$ cm sec^{-1} and $D_v = 1.32\times10^{-12}$ cm^2 sec^{-1}, giving a small value of f - about 0.02. Therefore, there is a limited chemical force available to drive the migration of the grain boundary at 700°C. However, at temperatures of 600°C and lower, a greater fraction of chemical force is developed. For example, at 600°C, a smaller part of the chemical free energy, ΔG^{diff}, would be lost to volume diffusion, since volume diffusion is slow in comparison with the growth rate v, and a fraction f would be available to move the boundary. Here, the following values have been used for estimation of f at 600°C: $v \sim 1\times10^{-6}$ cm sec^{-1}, $D_v = 8.42\times10^{-14}$ cm^2 sec^{-1}, so that f is roughly 0.26. At 500°C, where $D_v = 1.5\times10^{-15}$ cm^2 sec^{-1} and $v \sim 2\times10^{-7}$ cm sec^{-1}, $f \sim 0.96$.

Hence, the chemical driving force is expected to have a dominant influence in the temperature regime of 600°C and below, but it makes a minor contribution for temperatures above

600°C.

ii. Coherency force

In regimes where volume diffusion dominates, the local driving force for grain boundary migration may have another source. One possibility is that coherence stresses due to composition gradients developed in a depleted zone ahead of the boundary provide this source. The necessary concentration gradients are supposed to develop from the rapid grain boundary diffusion process as superimposed on a much slower process of volume transport to the grain boundary. By building up these steep concentration gradients on both sides, e.g. of a boundary at rest (Figure 63), stressed layers are expected to form. The stress is due to the variation of lattice spacing a, with composition as indexed by parameter $\eta = \frac{d\ell na}{dc}$. If some initial force acts on this boundary (as a consequence, say, of a fine initial grain size), a coherency force acting on the grain boundary is instantly established. If it is further assumed that volume diffusion governs the migration process, we can consider the equilibrium between the stressed layer of parent matrix and precipitates as well as between the unstressed product matrix grain and precipitates. The chemical potential difference across the boundary layer then gives rise to a concentration step which acts as an unbalanced force to move the boundary. This situation is represented in Figure 64 on a hypothetical free energy diagram while Figure 65 represents the concentration pro-

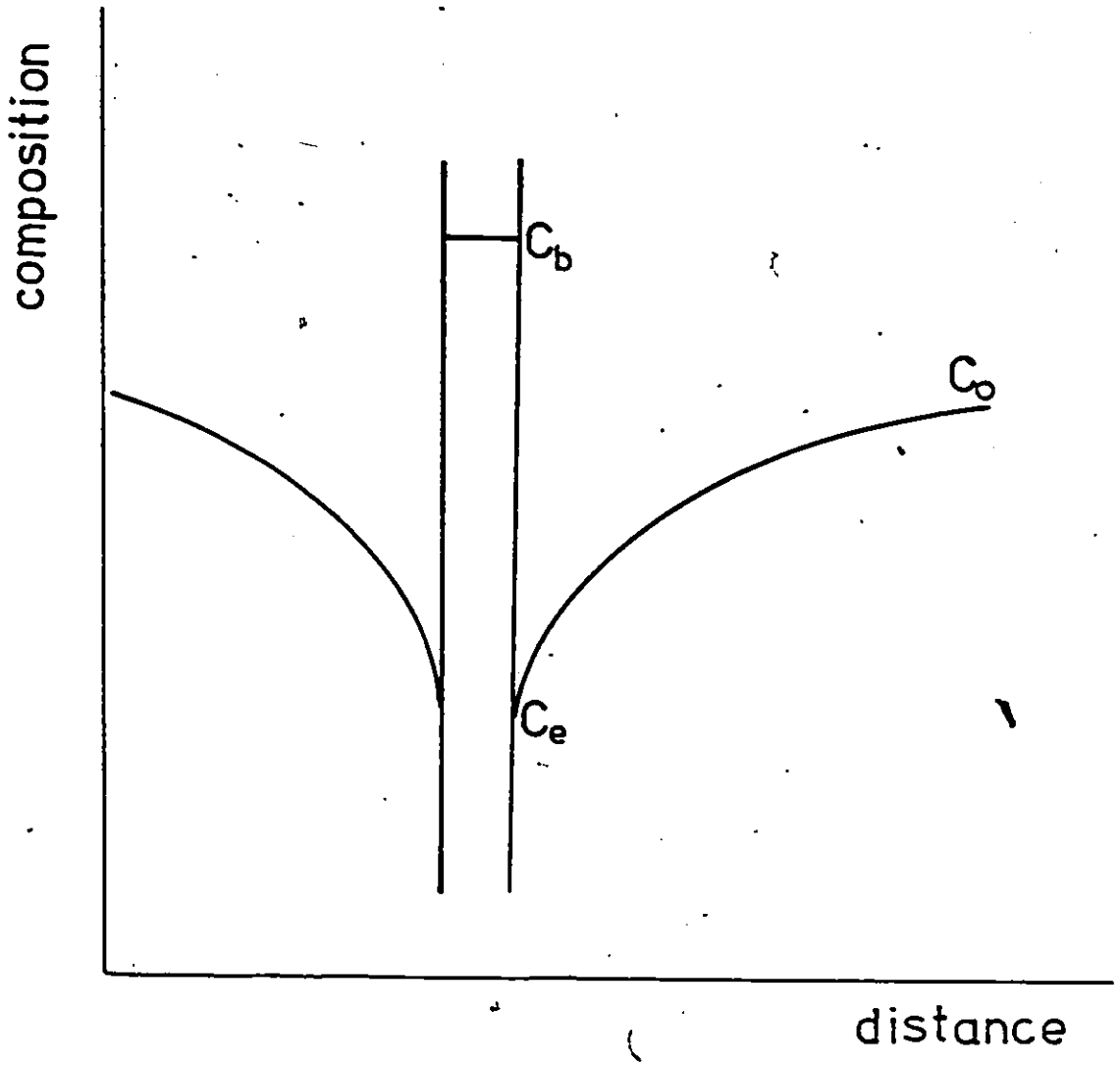

Figure 63. Schematic representation of concentration gradients developed at boundary at rest

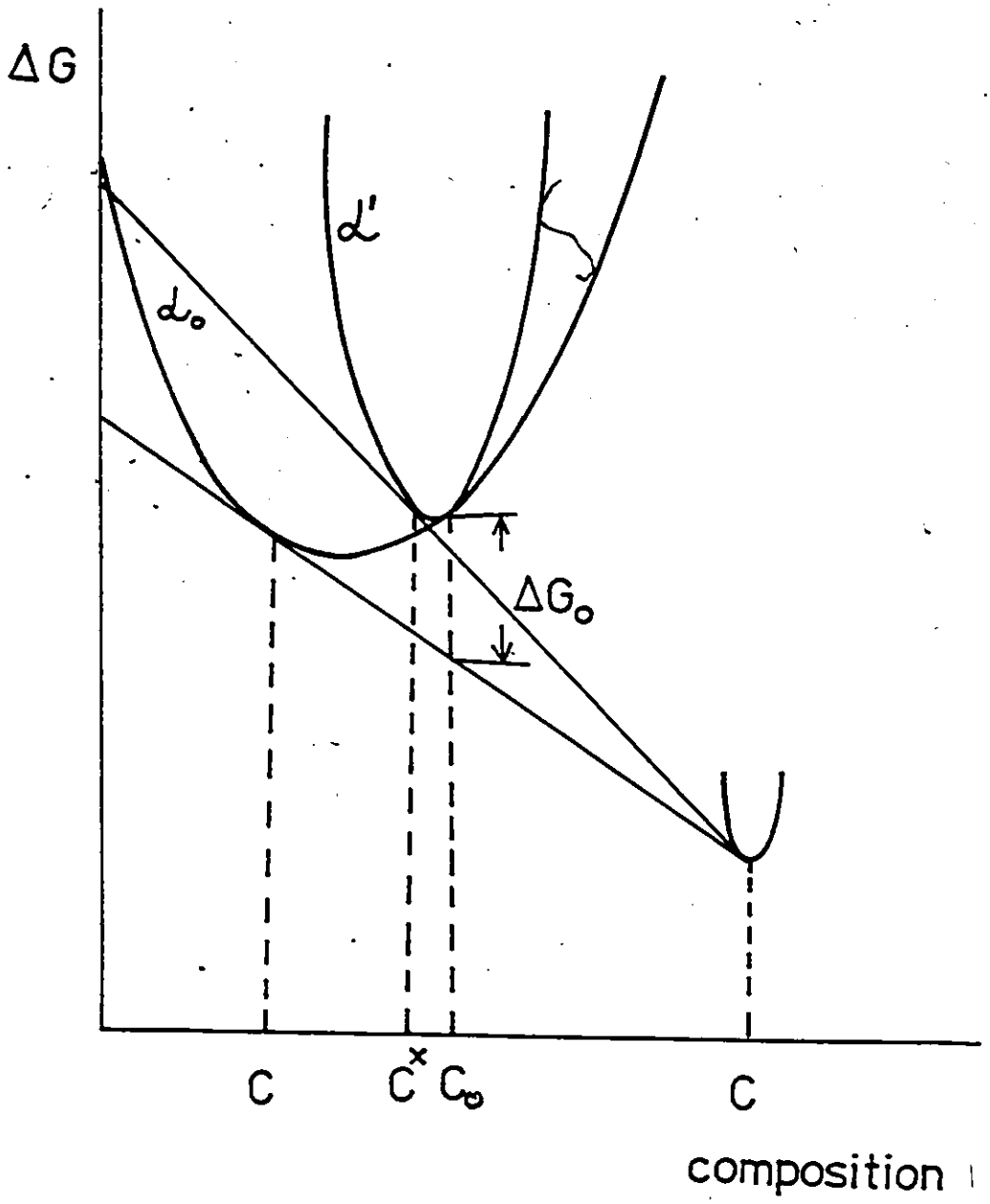

Figure 64. Hypothetical free energy diagram showing the chemical potential difference across the boundary layer due to coherency stresses

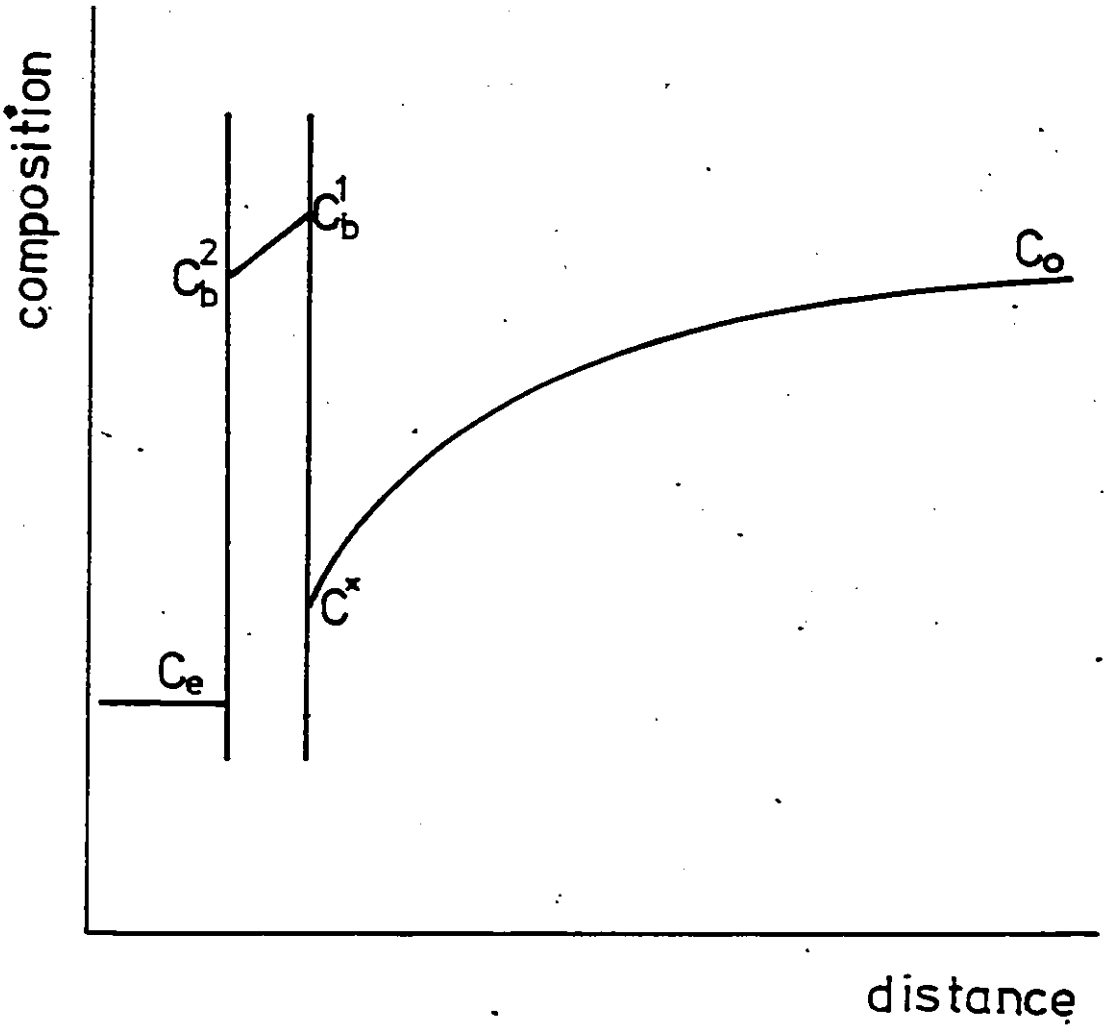

Figure 65. Schematic representation of concentration profile developed at moving boundary

file developed in the case of moving boundary.

The composition of the coherent layer, C^*, was obtained by minimizing the integral free energy of the system with respect to concentration. The chemical driving force acting on the boundary is of the form:

$$P^*_{chem} = \frac{RT}{V_m} \frac{(C^* - C_e^r)^2}{2C^*}, \qquad (27)$$

where C^* is the composition of the coherent layer and C_e^r is the concentration of the solute at the growing spherical particle which varies with particle growth due to capillarity. Thus, the driving force on the grain boundary due to coherency stresses in front of it is always increasing.

The composition of the coherent layer, C^*, will be obtained by minimizing the integral free energy of the system with respect to the concentration if the assumption of local equilibrium in the presence of a strain gradient is valid. The evaluation of C^* is given in Appendix I. The result is of the form :

$$C^* = \frac{RT \frac{C_e}{C_o} + \frac{4\nu^2 E}{1-\nu} C_o - \frac{2\mathcal{R}}{\delta^2} C_e}{\frac{RT}{C_o} + \frac{4\eta^2 E}{1-\nu} - \frac{2\mathcal{R}}{\delta^2}}. \qquad (28)$$

We note that, as expected, this expression for C^* is similar to one obtained by Hillert, the only difference being the term involving the effect of the composition gradient across the grain boundary. Assuming $\mathcal{R}$ (energy gradient coefficient) as a 6×10^{-6} erg cm^{-1}, this term becomes of two orders of magnitude smaller than the chemical term and as such can be ignored.

From the model proposed, the driving force calculated on the basis of equation (27) was negligible since the value for C^* as calculated from equation (28) gave the value of 0.0108 (the equilibrium composition at 700°C in Cu-Co alloy). This situation is explained by a small strain energy contribution, about two orders of magnitude smaller than the chemical term in equation (28) for parameters chosen to represent the Cu-Co alloy system.

iii) Capillary forces

A further kind of force acting on the grain boundary could perhaps arise from capillarity effects. Capillary forces have their origin in surface free energy.

Two kinds of capillary force are envisaged as possible:

a) a general, grain growth force arising from the initial curvature of grain interfaces and

b) a "pulling force" due to the tendency of the growing rods to pull the boundary into such a shape that the boundary curvature assists growth.

Both of these capillary forces should result in migration of the interfaces towards their centers of curvature. Each of them will be discussed in turn.

a) The grain growth force might be expected to play a role in a migration of the grain boundaries in the alloys investigated here due to a fine-grained nature of the material used. If the 60 μm grain size is used in a calculation of the

capillary force, a value of the order of 10^5 erg cm^{-3} is obtained. For an experimentally observed velocity of $\sim 1\times10^{-6}$ cm sec^{-1} at 600°C, this would give a mobility of the boundary of about 10^{-11} cm^4 erg^{-1} sec^{-1} in agreement with the value obtained from grain growth experiments in copper[84]; this agreement holds for any other temperature and experimentally observed velocity.

However, if the grain growth force were the only one operating during the formation of rod colonies, we would expect to find all grain boundaries migrating towards their centers of curvature. This was not observed.

b) In the section on genesis of rod formation (5.4c), we discussed the initial driving force acting on the boundary as due to the surface tension equilibrium at three-phase junction. Assuming the maintenance of the three-phase mechanical equilibrium at the rod-matrix junction during the growth of rod, a pulling force will develop in the absence of any other force acting on the interface. As the precipitates grow, they must pull the grain boundary between them, and in doing so, they will supply themselves with solute.

To demonstrate the existence of this pulling force, consider the following simple argument. If the rods grew and simply left the grain boundary behind them, they would necessarily form a new incoherent rod-matrix interface (with a surface free energy of about 750 erg cm^{-2}). The work done in creating this new surface, if the rod has moved a distance $d\ell$, would be:

$$W = N^{rod} 2\bar{u} r_0 \gamma_x d\ell , \qquad (29)$$

where N^{rod} is the number of rods per unit area, r_0 is the rod radius, and γ_x is the surface free energy of newly formed interface. The force would correspond to $F = W/d\ell$, i.e.:

$$F = N^{rod} \cdot 2\bar{u} r_0 \gamma_x \qquad (30)$$

which is of order 10^8 erg/cm^{-3}. Obviously, the boundary must accompany the rod tips. This simple consideration therefore indicates that the coherent rods could grow and pull the adjoining boundary along in the absence of a significant chemical force. The local force on the boundary due to capillarity would then be of the correct sign and be determined by the local boundary curvature.

f) Estimation of the interface shapes

In the preceding sections of this chapter we have come to the conclusion that there exist two possible kinds of force causing the movement of the boundary interface α_0/α during discontinuous precipitation in Cu-Co alloys. The forces developed are classified as a chemical force (most effective at temperatures at 600°C and below) arising from fast boundary diffusivity in these alloys and a pulling force (likely effective above 600°C) arising from the curvature of the boundary. These forces acting on the grain boundary determine its shape at any given value of interrod spacing, S.

The fact that cold work did not show any noticeable effect on discontinuous precipitation (Figure 54) suggests that the

stored energy term is probably smaller than the operating forces discussed above.

In the next section,we will proceed by considering possible equilibrium interface shapes when no net force acts on the grain boundary.

Figure 66 shows the boundary shape construction carried out under the assumption that the driving force has been completely eliminated, i.e., the surface of revolution which has zero net curvature was obtained by rotating a curve y(x) such that the integral

$$I = 2\bar{u} \int_{x_1}^{x_2} y \sqrt{(1+y'^2)}\, dx \qquad (31)$$

is a minimum. The method of finding the minimal surface of revolution is given in Appendix II a with the well known result of the form:

$$y = a \cos(\frac{x}{a} + b) \ , \qquad (32)$$

where x and y coordinates are defined in Figure 66a, b, and a and b parameters are found from the imposed condition as a tangent of the equilibrium dihedral angle between the grain boundary and the cylinder (being 55° as obtained from the equilibrium nucleus shape construction in Figure 59). The details of determination of parameters a and b are given in Appendix II b.

Figure 66 shows that the shape of the boundary is fairly flat, and as expected, only locally curved close to the

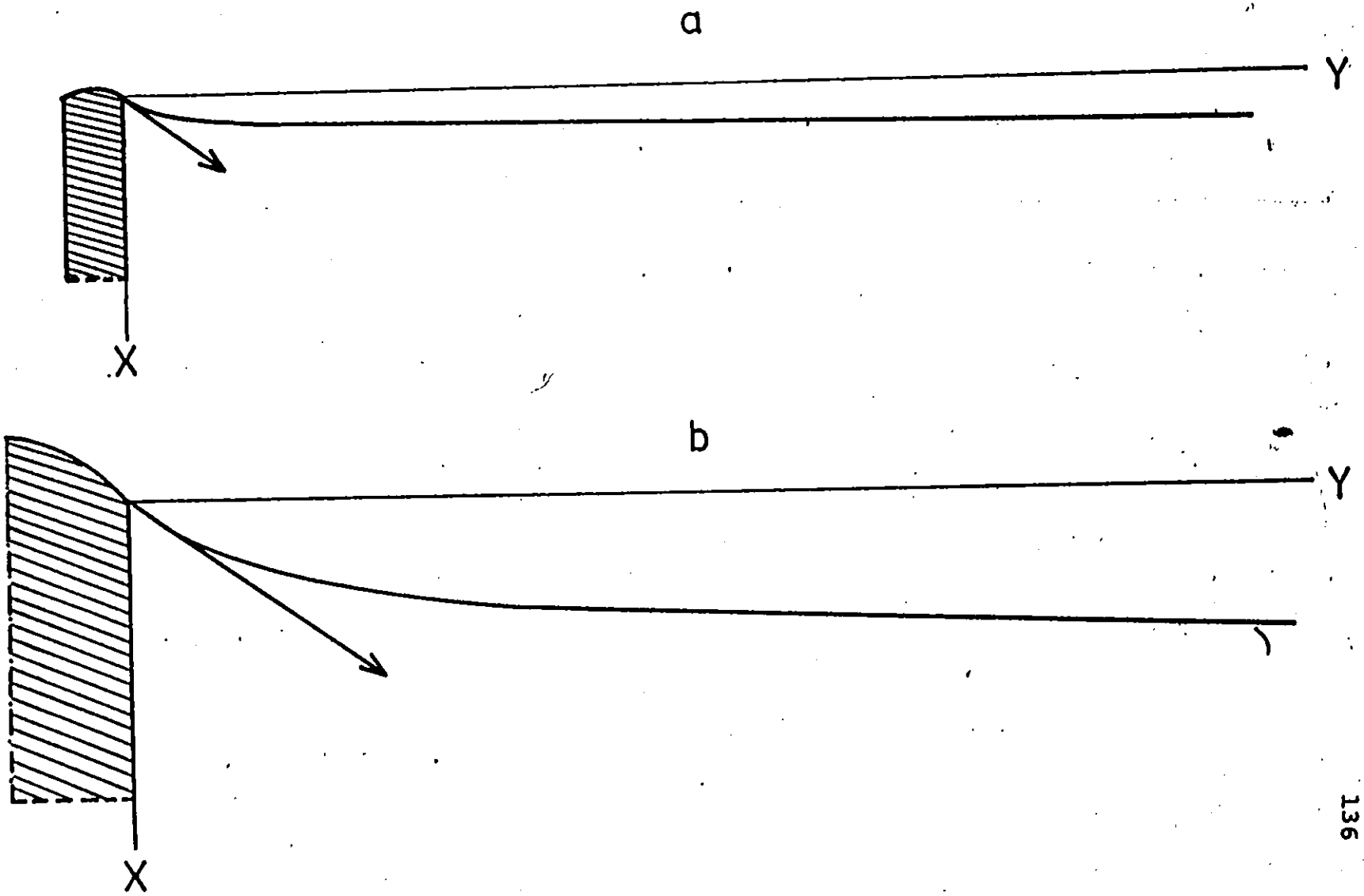

Figure 66. a) The boundary shape construction when no force acts on it
b) the same as in a) just magnified

precipitate in order to satisfy mechanical equilibrium at the three-phase junction. The geometry at the junction is quite sensitive to the values chosen for γ's representing the surface free energies of adjoining interfaces.

Next, we will proceed with the solution of the diffusion equation for the case of a grain boundary diffusion-controlled process with cylindrical symmetry. Steady-state growth will be assumed with all diffusion occurring inside the grain boundary. Maintenance of the equilibrium composition of the matrix in contact with the rod particles will also be assumed. The diffusion equation is of the form

$$D_b \delta \left(\frac{\partial^2 C_b}{\partial r^2} + \frac{1}{r} \frac{\partial C_b}{\partial r}\right) + v(C_o - C_p) = 0 , \qquad (33)$$

where $C_b \equiv \frac{C_p}{k}$ with k assumed $\sim$ 1, D_b is the boundary diffusivity, δ is the boundary thickness, v is the growth velocity normal to the moving interface, C_o is the composition of the supersaturated matrix in front of the advancing boundary, C_p is the composition just behind the boundary, and C_b is the boundary composition which is closely connected with matrix composition C_p, and r is the radial distance from the rod centre. The method of solving the diffusion equation is given in Appendix III, and the final result is obtained as:

$$\frac{C(r)-C_o}{C_p-C_o} = \frac{I_o(\sigma r)K_1(\sigma b)+I_1(\sigma b)K_o(\sigma r)}{I_o(\sigma a)K_1(\sigma b)+I_1(\sigma b)K_o(\sigma a)} , \qquad (34)$$

where I_o and K_o are the modified Bessel functions of zero order of the first and second kind, respectively, and I_1 and K_1 are their derivatives, a is the rod radius, and b = S/2; parameter σ is expressed as

$$\sigma = \sqrt{\frac{kv}{D_b \delta}} \quad . \tag{34a}$$

Figure 67 shows the calculated concentration profiles for different σ values, and for the case of $b \approx 10\ a$ (corresponding to the present experimental conditions). The numbers given on each curve are the values of $\sigma \cdot (b-a)$. Table III lists the values of $\sigma(b-a)$ in Cu-Co alloys for the present investigation. The boundary diffusivity D_b was chosen to be such that the activation energy (Q_b) is half of that for the volume diffusion case (Q_v) for which there exists experimental evidence from tracer diffusion of Co^* in Copper ($D_{Co \to Cu} = 1.93 \exp(-51/RT)$[77]. There are no experimental measurements of grain boundary diffusivity for either Cu or Co atoms in copper. However, there are data[87] on grain boundary diffusion of Cu in Ni which give an activation energy of 23 Kcal mol^{-1}, with the volume diffusion as $D^*_{Ni-Cu} = 2.7 \exp(-56.5/RT)$ approaching that of D^*_{Co-Cu}. Since Ni atoms are similar to Cu atoms, the value $Q_v/2$ has been taken here.

The result of these considerations is that the solute distribution in the boundary is essentially flat. If the boundary diffusivity is enhanced by boundary motion as suggested by the work of Hillert and Purdy, the conclusion will be unchanged. This implies that a) the reaction is not controlled by grain

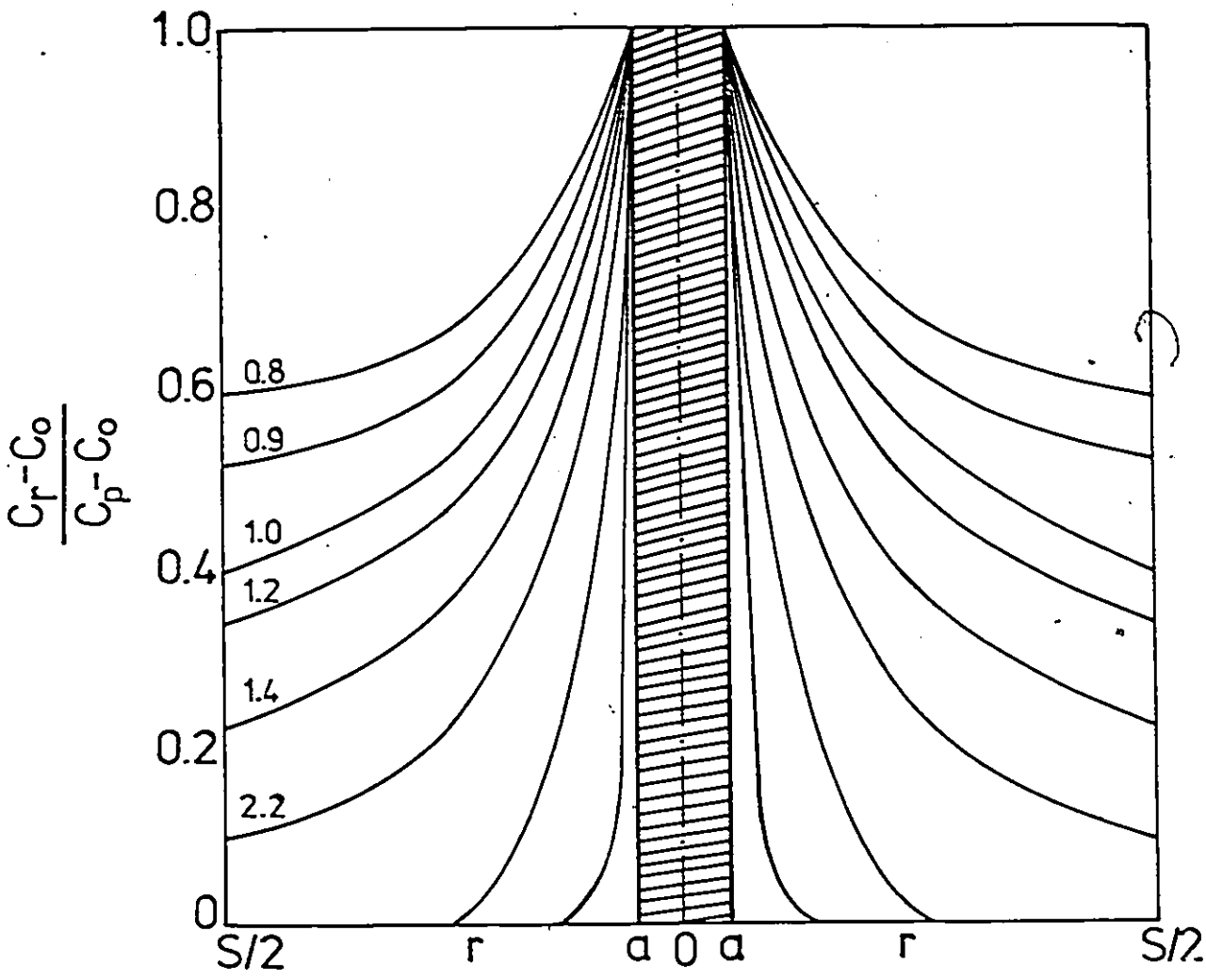

Figure 67. Calculated concentration profiles from the solution of grain boundary diffusion controlled process in the case of cylindrical symmetry

TABLE II

Temperature (°C)	velocity cm sec^{-1}	D_b $cm^2 sec^{-1}$	$\sigma = \sqrt{\frac{k \cdot v}{D_b \delta}}$ cm^{-1}	$\sigma \cdot (\frac{s}{2} - a)$
700	4×10^{-7}	8.1×10^{-7}	0.5×10^{3}	1.3×10^{-2}
600	1×10^{-6}	1.81×10^{-7}	1.05×10^{4}	2.8×10^{-2}
500	2×10^{-7}	2.74×10^{-8}	1.89×10^{4}	5.12×10^{-2}
400	1×10^{-8}	2.36×10^{-9}	0.29×10^{3}	0.79×10^{-3}

boundary diffusion and b) the interface shape, however determined, will be one of constant net curvature, as discussed below.

Assuming that the moving interface takes an equilibrium shape, then the equilibrium equation of the forces acting on the boundary must be such that the sum of the other forces exactly balance the forces due to interface curvature at each point along the interface:

$$\sum_{i=1}^{n} P_i = \frac{a\gamma}{\rho} \quad , \tag{35}$$

where ΣP_i is the sum of forces acting on the boundary, a is a geometric factor, γ is the surface free energy of the moving interface and ρ is the radius of curvature. For the discontinuous precipitation reactions considered here this equation assumes the form:

$$f \frac{\Delta G^{chem}}{V_m} + \frac{v}{M} + \gamma(K_1+K_2) = 0 \quad , \tag{36}$$

which expresses an equilibrium under the action of four forces: one equal to $f\Delta G^{chem}/V_m$ (the chemical force); one is equal to v/M (a friction force), and two forces of the same kind but possibly of opposite sign, γK_1 and γK_2, due to the surface tension of the boundary.

For the simple case of a constant net force acting on the moving interface, we can describe a few possible interface shapes. These shapes as schematically presented in Figure 68

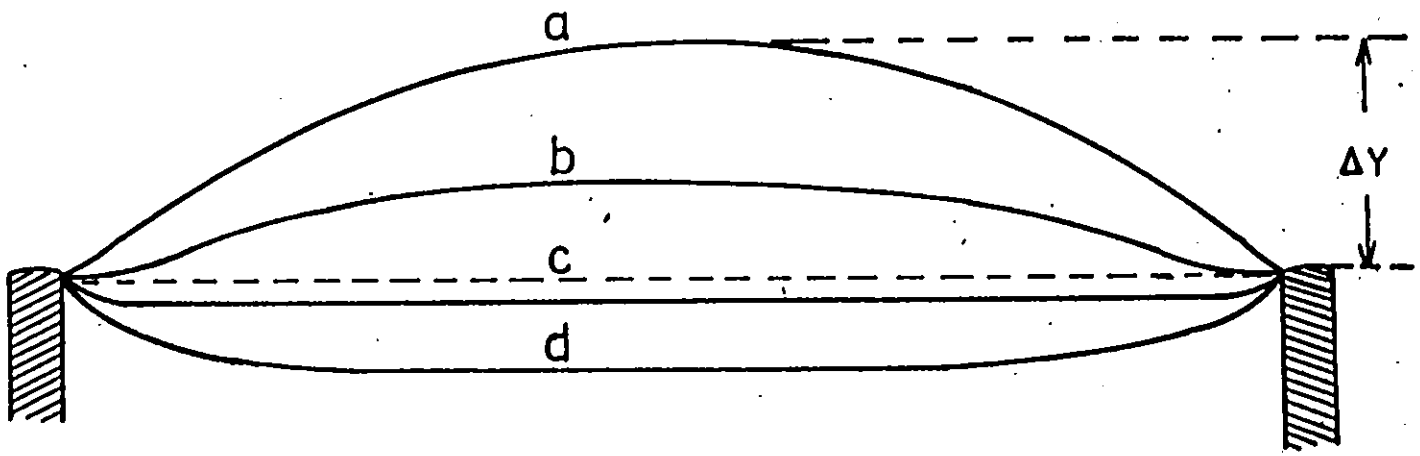

Figure 68. Schematic representation of various possible shapes that grain boundary can adopt if a) chemical force fully operates, b) chemical force is partially offset by mobility, c) no-force acts on the boundary, d) pulling force aids the motion of the boundary

are obtained when:

i) the chemical force balances the curvature (the mobility in this case is assumed to be so high that its influence can be neglected) (Figure 68 a).

ii) the chemical force is partially offset by a mobility term (Figure 68b),

iii) the net curvature is set equal to zero (Figure 68 c),

iv) the pulling force aids the motion of boundary (68d).

For the present experimental conditions, a flat composition profile in the interface is expected for all temperatures of interest. Thus, the chemical term should be essentially constant along the interface.

Since the mobility may be assumed to be constant at given temperature and composition, a constant net force from the chemical and mobility terms will act on the α_0/α interface (equation (34)). Thus, the shapes of Figure 68 b,c are thought to be possible representations of the true shape. It is difficult to use experimental observations of quenched interfaces to decide between them because of the possibility that some alternation occurred in the final quench. Generally, it is felt that this problem should be of minor importance since the fastest growth rate encountered, in this work is about 1×10^{-6} cm.sec^{-1} so that in 1/10 second the interface can advance only 10 Å. However, due to the fine scale microstructure of rods, the interrod spacing being itself small ($\sim$ 600 Å) the interface shapes as observed cannot be fully trusted.

If it is nevertheless assumed that the observed interface shapes are representative of growth conditions, then it is apparent from Figures 28 and 42 that these are generally rather flat. Since the composition profiles within the interface are presumed flat, boundary diffusion cannot be the controlling step and we are left with three alternatives:

i) The shape (a) might be realized in the case of a high mobility boundary, such that most of the chemical force is balanced by curvature. Hence, the net driving force is reduced to a very small value and we can calculate the curvatures of the bowing boundary at, say 500°C as follows:
for the Cu-1.62 wt% Co alloy, $\frac{\Delta G_{chem}}{V_m}$ is about 1.8×10^8 ergs/cm^3 for a rod radius of 20 Å. Then, using the Ashby-Lewis expression for the amplitude

$$\Delta y = \frac{s^2 \Delta G_{chem}}{8\gamma_b V_m} , \qquad (37)$$

we find $\Delta y \sim 300$ Å, which is comparable with the spacing.

ii) A flatter shape, (b) or (c), would imply that a larger driving force acts on the boundary, and that the mobility of the boundary is small, and rate-determining.

iii) An inverted shape (d) might be realized at the highest temperatures where the chemical force is largely dissipated by volume diffusion and where capillarity is needed to overcome boundary friction.

For most of the temperature range of interest, it seems that the second alternative is the most reasonable. It is consistent with the observations of quenched interfaces, and it does not require that the interface support a large bowing amplitude (which would tend to cause the boundary to break away from the rods by perturbing the equilibrium at the three crystal junction).

In the discussion following this section, we will be considering the kinetics of rod transformation and we will demonstrate that the mobility is low in the given experimental conditions, thus controlling the rate of the reaction.

5.5 Growth Kinetics

The kinetics of rod formation in the Cu-Co alloys will be considered in two regimes of temperature; one above 600°C where there is little effective chemical force acting on the boundary and the other below 600°C, where the full chemical force acts on the boundary.

a) Low-temperature regime

In the previous section, we have concluded that at lower temperatures the moving interface α_0/α during rod growth is migrating under the influence of a large chemical force which is not offset by curvature. Hence, mobility must be controlling the rate of rod growth.

By assuming a mobility controlled reaction such that the full chemical force acts on a boundary with no net curvature,

we will evaluate the mobilities for the present alloys and then compare these with the mobilities obtained from other experiments[84,85,86]

The expression used for mobility calculation is of the general form:

$$v = M.P \quad , \qquad (38)$$

where v is the velocity of the boundary movement and P is the force acting on the boundary; M is the constant of proportionality expressing the velocity per unit force. In the present case, force P is the chemical free energy $\Delta G_r^{chem}/V_m$ released during the growth of rod of radius r, and is only limited by the capillarity effect for a given rod radius, r.

The mobilities of the moving boundary in these experiments are plotted in Figure 69a; the mobilities extracted from other experiments are also plotted (Figure 69 b,c). It is clear that the mobilities as obtained in the Cu-Co system during the discontinuous growth of rods are about three orders of magnitude lower than those from other experiments. The experiments chosen to yield values of mobility for purposes of comparison were grain growth and recrystallization reactions since they also involve boundary mobility control.

Grain growth experiments in α-brass were used[84] and the experimental data extrapolated for pure copper, giving values of $K_o = 3\times10^{-3}$ $cm^2.sec^{-1}$ and $H_o = 20.2$ kcal/gmol; the mobilities are then plotted in Figure 69 b.

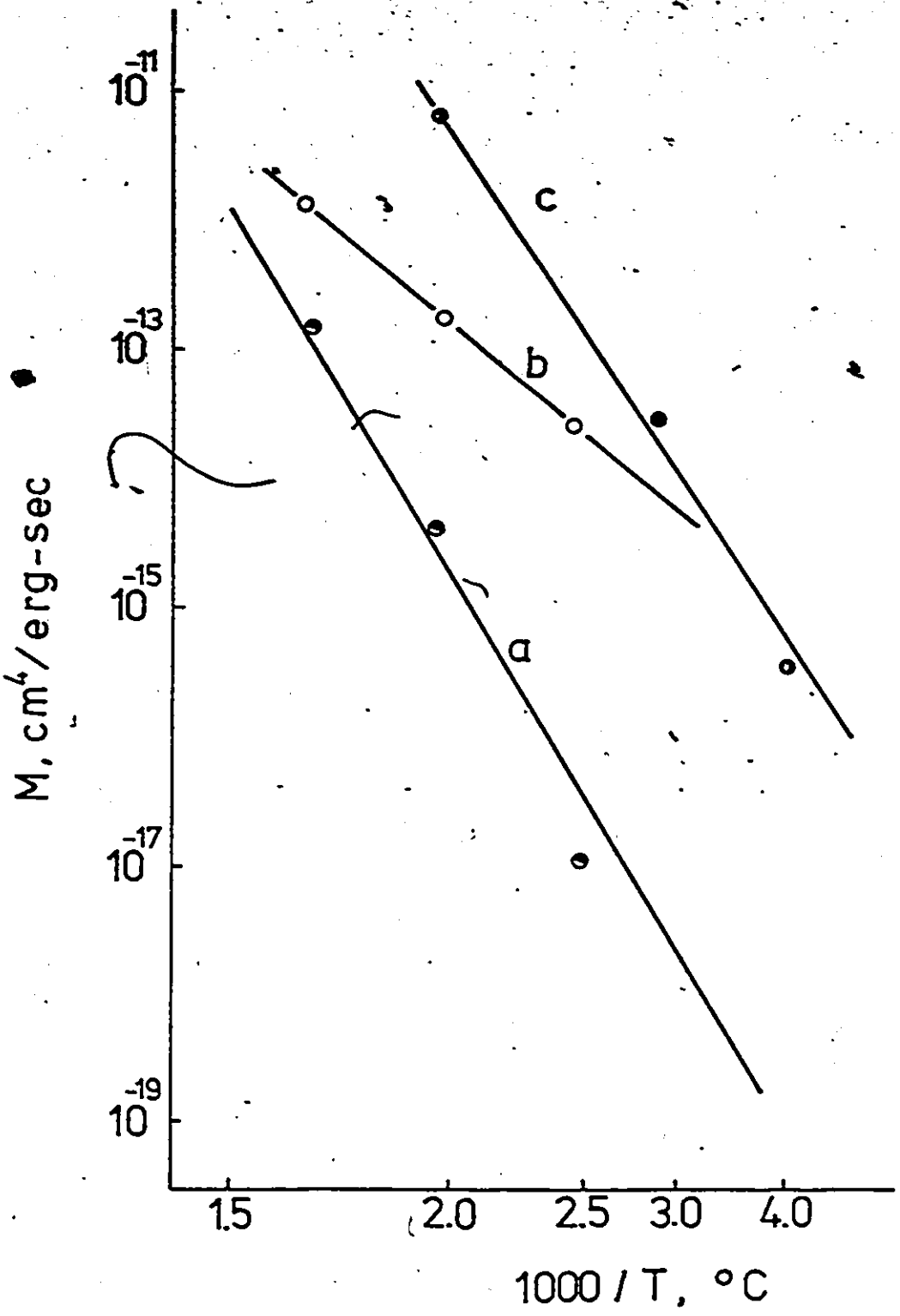

Figure 69. Mobility terms plotted versus temperature.
a) from present experimental conditions
b) from grain growth experiments
c) from recrystallization experiments

Recrystallization experiments were performed on OFHC copper[85,86], leading to the results plotted in Figure 69c. The difference in activation energies for grain growth and for recrystallization reactions is thought to result from different purity levels of the copper.

From the results presented in Figure 69, the boundary mobility in Cu-Co alloys is thus shown to be much smaller than for copper. It is believed that this is due to the homogeneously precipitated coherent particles which are always present in front of the advancing interface. This is confirmed by the recrystallization behaviour of Cu-Co alloys investigated[16,88]. It was found that coherent particles do impede the recrystallization.

We can argue about the importance on strain energy on the boundary movement in this system from simple macroscopic point of view. The strain energy per unit volume does not depend on the size of the particles, but on their volume fraction (being proportional to it). The volume fraction of homogeneous precipitation during the development of rod colonies is much smaller than that of rods (otherwise they will stop the growth of rods), thus causing the resistance to the increase in strain energy per volume. This effect is decreasing as homogeneous particles approach their equilibrium volume fraction with aging.

After arguing that the mobility is rate controlling in the discontinuous precipitation of rod particles in Cu-Co

alloys (due to its low value as a consequence of coherent spherical Co particles present in front of the moving boundary) we will proceed further with the discussion of kinetic behaviour, i.e. determination of the distance S between rods. In general, in a discontinuous precipitation reaction the maximum velocity criteria (i.e. the maximum decrease in the free energy) is taken for spacing determination; the consideration of maximizing the rate of entropy production is also available[90].

Since the velocity of the reaction is proportional to the the driving force (the proportionality constant M being the mobility of the moving front), and the driving force is proportional to the maximum available chemical force (the factor of proportionality f being a constant at a given temperature and velocity), we can represent the kinetic behaviour of discontinuous Cu-Co transformation at a given temperature by plotting the maximum available chemical free energy $\Delta G_r^{chem}/V_m$ versus the radius of rod formed, r, (Figure 70). For a given radius, there will be an equilibrium volume fraction which determines the spacing S (also shown in Figure 70). The driving force is zero at critical radius r_c for which spacing S adopts an infinite value. By further increasing the radius of rod (i.e. the volume fraction), the driving force increases rapidly towards its maximum corresponding to the radius r_0 and spacing S_0, after which there is no marked change in driving force (or volume fraction). This implies

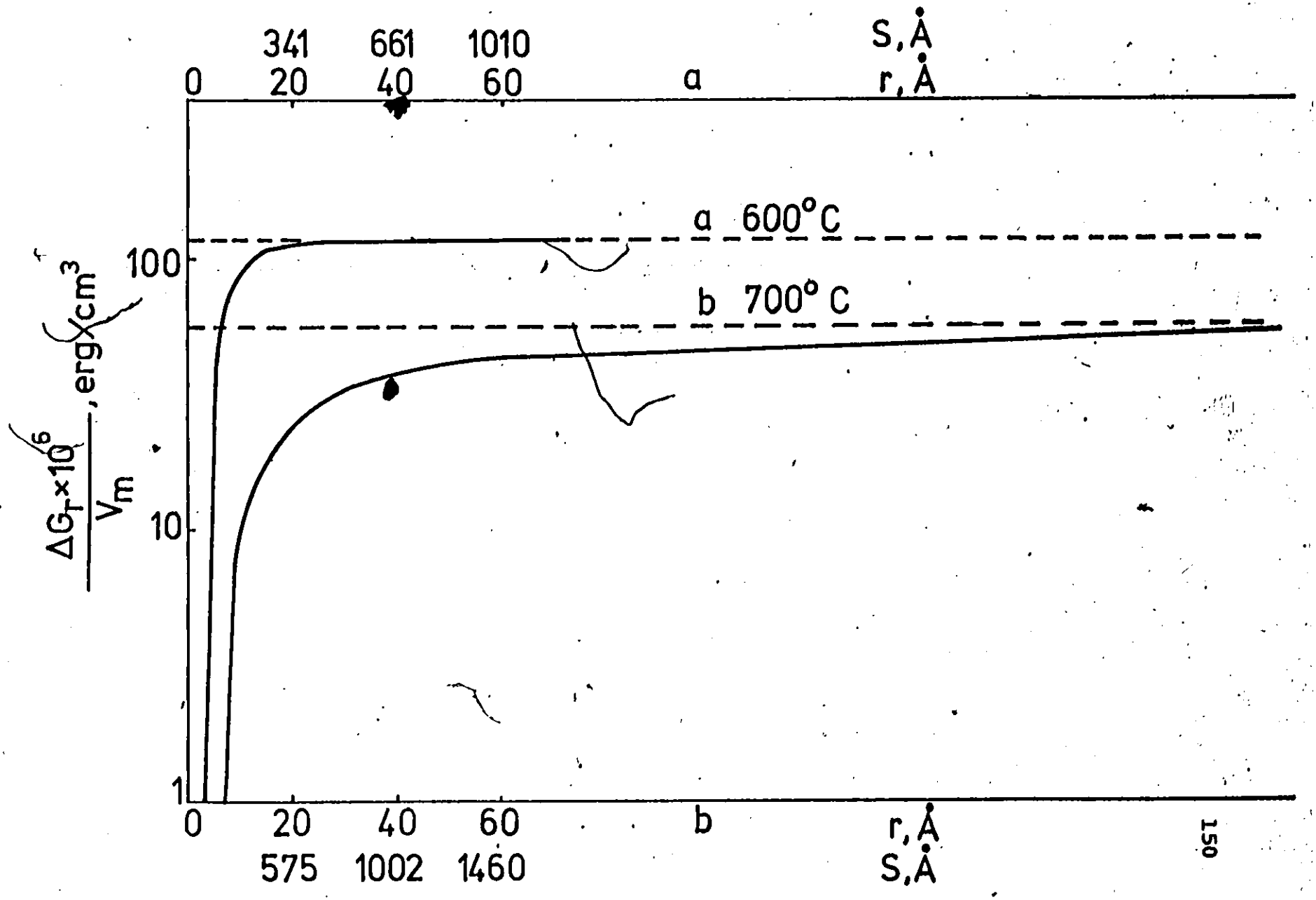

Figure 70. Chemical free energy available for rod formation versus radius and S spacing at a) 600°C and b) 700°C

that the velocity should also be constant above S_o spacing. However, one should expect a falling off of velocity at large spacings due to an increasing role of boundary transport.

It is therefore clear that there exists a range of spacings (600 to about 5000 Å at 600°C) over which the velocity of the reaction would be roughly constant. The observed spacing S_o (∿ 500 Å at 600°C and ∿ 1000 Å at 700°C) is the minimum spacing corresponding to this maximum velocity. At the same time, the corresponding radius r_0 necessarily leaves the maximum supersaturation in the product matrix phase.

In order to estimate theoretically the spacing at which the boundary diffusion starts to control the kinetics of reaction, we have chosen a spacing of 1 μ, the other conditions being the same, and calculated the concentration profiles from Figure 67. The chemical force is found to be decreased to 1/3 of its maximum value available at given temperature. At the spacing of 0.8 μ the driving force was decreased to 2/3 of its maximum value.

b) The high temperature regime

It was already proposed in section 5.4 iii that, at higher temperature, the growing rods pull the boundary. In order to keep pace with the growing rods, the pulling force would then adjust itself internally by assumping a shape like that of Figure 68d. As a first approximation, it will be considered that the volume diffusion gradient is everywhere normal to a planar grain boundary, which has sufficiently high diffusivity to act as a perfect sink (i.e. concentration in the grain boundary is the same everywhere along it) and is in equilibrium with the rods. Then, the driving force on the interface is given by

$$P = [1-\exp(-\frac{vb}{2D_v})]\frac{\Delta G_r}{V_m} . \qquad (39)$$

The fact that volume diffusion gradients exist in front of the boundary will have two results. The first of these, as already noted, is the diminution of the chemical force (to about 2% of its maximum possible value) available to drive the boundary. The second is that any homogeneously nucleated particles will tend to be dissolved before the boundary reaches them. Thus both the driving force and the resistance to boundary motion will be decreased, and it becomes difficult to assess, with certainty, the conditions of the various small forces which might act on the interface at these temperatures. It is not even clear what the rate-determining step might be in these circumstances, although the intrinsic mobility of the boundary suggests itself as a likely rate-determining factor.

Further, this discussion deals with the observed interface velocity only. Since higher velocities would be accompanied by larger chemical forces, one could conceive the non-equilibrium component of the transformation to exist at these higher temperatures also. However, the answer to this question needs a further analysis of the reaction in this temperature region.

CHAPTER 6

FUTURE WORK

Discontinuous precipitation is a complex reaction, whose analysis depends on the knowledge of several quantities in addition to the growth parameters v and S. Such quantities include the concentration profile behind the moving boundary, grain boundary diffusivity, mobility of the moving boundary, specific surface energies of surfaces involved.

(a) The concentration profile in a Cu-Co alloy with discontinuous precipitates of such a fine spacing as has been observed experimentally could be obtained by using a STEM technique.

(b) Although it is impossible to obtain independent data for interface diffusion between the phases of interest in a cellular precipitation reaction, boundary diffusion data in the homogeneous alloys of the major phase should still be useful, such as in α-Cu-Co.

(c) For similar reasons, independent experiments should be performed to evaluate the mobility of grain boundaries in both α Cu-Co alloys and α+β Cu-Co alloys, such as grain growth or recrystallization measurements.

In order to confirm the kinetics of rod reaction, in situ, hot stage electron microscopy technique would be of value. However, it will still be very difficult to carry out this procedure since one cannot predict which grain will give the desired transformation.

CHAPTER 7

CONCLUSION

Supersaturated α phase copper-cobalt alloys decompose by both a continuous and discontinuous mode. The general precipitates interfere with the cellular reaction, influencing its kinetics. The growth rate and interrod spacings for discontinuous precipitates have been measured. Transmission electron micrographs have been obtained of the discontinuously transformed region, showing rod particles as well as rows of spherical precipitates. These latter spheres are thought to form as a consequence of rod instability.

An evaluation of the kinetic data suggested that an analogue to Smith's model[39] of discontinuous precipitation holds at higher temperatures while Hillert's model[34] is valid for the lower temperature range. A solution of boundary diffusion controlled growth and local equilibrium at the advancing interface was obtained in the case of rod precipitate morphology. The activation energy calculated for the apparent boundary diffusivity is about 35 kcal/mole, which is in agreement with the data obtained from recrystallization experiments under similar alloy conditions. However, the value of boundary mobility required for quantitative agreement is about 1000 times smaller than that calculated from purely mobility controlled reactions in other copper alloys. The lower mobilities are explained as a consequence of homogeneously precipitated particles in front of the discontinuous reaction interface.

APPENDIX I

The evaluation of the composition of coherent layer is done by minimizing the total free energy of a system as follows.

In front of the boundary the free energy is a function of the composition and of the lattice parameter; that is the free energy is the sum of the chemical free energy and elastic free energy. Behind the boundary there is only the chemical free energy term since the stresses are relaxed at the grain boundary. Across the boundary, there exists a gradient energy term. The total free energy will be the sum of all these terms and we can write:

$$F^{total} = F^{chem}_{behind\ g.b.} + (F^{chem} + F^{strain})_{in\ front} + F^{\Delta C}_{across\ g.b.}, \quad \text{(AI-1)}$$

where

$$F^{chem}_{behind\ g.b.} = RT\,\frac{(C_o - C_e)^2}{2C_o}, \quad \text{(AI-1a)}$$

$$(F^{chem} + F^{strain})_{in\ front} = RT\left[\left(\frac{C_o - C_e}{2C_o}\right) + \frac{2\mu^2 E}{1-\nu}\,(C^* - C_e)^2\right], \quad \text{(AI-1b)}$$

where E is the elastic modulus and ν the Poisson's number and

$$F^{\Delta C} = \mathcal{R}\left(\frac{dc}{dx}\right)^2 = \mathcal{R}\,\frac{(C^* - C_e)^2}{\delta^2}, \quad \text{(AI-1c)}$$

where δ is the boundary width, and $\mathcal{R}$ is the energy gradient coefficient.

In equilibrium the total free energy is minimum so that:

$$\frac{\partial F^{tot}}{\partial C^*} = 0 \quad ,$$

which gives the solution for composition of the coherent layer, C^*, as:

$$C^* = \frac{RT\,\frac{C_e}{C_o} + \frac{4\eta^2 E}{1-\nu}\,C_o - \frac{2\mathcal{R}}{\delta^2}\,C_e}{\frac{RT}{C_o} + \frac{4\eta^2 E}{1-\nu} - \frac{2\mathcal{R}}{\delta^2}} \qquad \text{(AI-2)}$$

APPENDIX IIa

The calculus of variations is applied in determining the equilibrium shape of the grain boundary, since the basic problem in the calculus of variations is just to determine a function such that a certain definite integral involving that function and certain of its derivatives takes on a maximum or minimum.

Therefore, in order to determine the surface of revolution, obtained by rotating about the x axis a curve passing through two given points (x_1,y_1) and (x_2,y_2), which has minimum surface area, we must determine the function $y(x)$ which specifies the curve to be revolved, in such a way that the integral

$$I = 2\bar{u} \int_{x_1}^{x_2} y\sqrt{(1 + y'^2)}\, d/x \qquad \text{(AII-1)}$$

is a minimum, and also that $y(x_1) = y_1$ and $y(x_2) = y_2$ with $F = y\sqrt{1 + y'^2}$, the Euler equation

$$\frac{d}{dx}\left(\frac{\partial F}{\partial y'}\right) - \frac{\partial F}{\partial y} = 0 \qquad \text{(AII-2)}$$

must be satisfied and it becomes:

$$\frac{d}{dx}\left[\frac{yy'}{\sqrt{1 + y'^2}}\right] - \sqrt{(1 + y'^2)} = 0 \qquad \text{(AII-3)}$$

or, after a reduction,

$$yy'' - y'^2 - 1 = 0 \,. \qquad \text{(AII-4)}$$

Following the usual procedure for solving equations of this type, we set

$$y' = p \quad , \quad y'' = \frac{dp}{dx} = p\,\frac{dp}{dy}$$

so that ( ) becomes

$$py\,\frac{dp}{dy} = p^2 + 1 \,. \qquad \text{(AII-5)}$$

This equation is separable, and is integrated to give:

$$y = a\sqrt{(1 + p^2)} \equiv a\left[1 + \left(\frac{dy}{dx}\right)^2\right]^{1/2} \,. \qquad \text{(AII-6)}$$

There follows,

$$\frac{dy}{dx} = \left(\frac{y^2}{a^2} - 1\right)^{1/2} \qquad \text{(AII-7)}$$

and hence finally

$$y = a\cosh\left(\frac{x}{a} + b\right) \,. \qquad \text{(AII-8)}$$

APPENDIX AIIb

$$\boxed{y = a \cosh\left(\frac{x}{a} - b\right)}$$

$$\frac{dy}{dx} = \text{tg } 55° = 1.4281$$

$$\frac{dy}{dx} = \frac{y_1}{x_1} \quad \therefore \quad \frac{y_1}{x_1} = 1.4281$$

$$\Downarrow \text{ for } y_1 = 5.0$$

$$x_1 = 3.5$$

$$\frac{y_1}{x_1} = \frac{dy}{dx} = \sinh\left(\frac{x_1}{a} - v\right) \Rightarrow \sinh\left(\frac{x_1}{a} - b\right) = 1.4281$$

$$y_1 = a \cosh\left(\frac{x_1}{a} - b\right) \Rightarrow \cosh\left(\frac{x_1}{a} - b\right) = \frac{y_1}{a} = \frac{5.0}{a}$$

$$\cos^2 h\left(\frac{x_1}{a} - b\right) = \frac{y_1^2}{a^2}$$

$$\cos^2 h = 1 + \sin^2 h \quad \left[\sin^2 h\left(\frac{x_1}{a} - b\right) = \left(\frac{y_1}{x_1}\right)^2 = 1.4281^2\right.$$

$$= \sin^2 h\left(\frac{x_1}{a} - b\right) = 2.0395$$

$$\cos^2 h\left(\frac{x_1}{a} - b\right) = \frac{y_1^2}{a^2}$$

$$\cos^2 h\left(\frac{x_1}{a} - b\right) = 1 + \sin^2 h = 2.0395$$

$$\therefore \frac{y_1^2}{a^2} = 2.0395 \Rightarrow \boxed{a = 2.868}$$

$$\sinh\left(\frac{x_1}{a} - b\right) = 1.4281$$

$$\sinh\left(\frac{3.5}{2.868} - b\right) = 1.4281$$

$$\frac{3.5}{2.868} - b = 1.1542$$

$$\boxed{b = 0.0662}$$

TABLE AIIb

x (Å)	y (Å)
4	6
6	11
8	22
10	44
12	88
14	177
15	251
16	355

APPENDIX III

Steady-state diffusion equation of the form

$$D_b\delta\left(\frac{d^2C_b}{dr^2} + \frac{1}{r}\frac{dC_b}{dr}\right) + v(C_o - C_p) = 0 \qquad \text{(AIII-1)}$$

has been solved satisfying the relation: $C_b = C_p/k$ and boundary conditions that are in the range $0 \leq a \leq r \leq b$:

i) at $r = a$ $\quad C_p = C$

ii) at $r = b$ $\quad dc/dr = 0$

under the assumption of boundary being a plane. If assumed k=1, the above equation becomes:

$$\frac{d^2C_b}{dr^2} + \frac{1}{r}\frac{dC_b}{dr} - \frac{v}{D_b\delta}C_b = -\frac{vC_o}{D_b\delta} \qquad \text{(AIII-2)}$$

The solution of this type of equation consists of two parts:

$$C = C_{particular} + C_{cylindrical} \qquad \text{(AIII-3)}$$

By introducing a new variable, $\sigma^2 = \frac{v}{D_b\delta}$ the $C_{particular}$ becomes the solution of nonhomogeneous part of the equation:

$$-\sigma^2 C_b = vC_o/D_b\delta \qquad \text{(AIII-4)}$$

hence

$$C_{particular} = C_o \qquad \text{(AIII-5)}$$

The $C_{cylindrical}$ is the solution of the homogeneous part of the primary equation:

$$\frac{d^2C_b}{dr^2} + \frac{1}{r}\frac{dC_b}{dr} - \frac{v}{D_b\delta}C_b = 0 \qquad \text{(AIII-6)}$$

such that it is given in a general form in terms of modified Bessel functions of the first (I_o) and second (K_o) kind of zero order as:

$$C_{cylindrical} = \lambda I_o(\sigma r) + \mu K_o(\sigma r) \; . \qquad \text{(AIII-7)}$$

The solution which satisfies this equation is given as:

$$C_{cylindrical}(r) = \lambda \begin{vmatrix} I_o(\sigma r) & K_o(\sigma r) \\ I_o(\sigma a) & K_o(\sigma a) \end{vmatrix} + \mu \begin{vmatrix} I_o(\sigma r) & K_o(\sigma r) \\ I_o'(\sigma b) & K_o'(\sigma b) \end{vmatrix} \; . \qquad \text{(AIII-8)}$$

Let us denote the first determinant multiplying the constant λ as $D_\lambda(r)$ and the second determinant multipling the constant μ as $D_\mu(r)$. Now, by imposing the given boundary conditions we get:

$$D_\lambda(a) = 0$$

and

$$D_\mu'(b) = 0$$

so that

$$C_{cylindrical}(a) = \mu \begin{vmatrix} I_o(a) & K_o(a) \\ I_o(a) & K_o'(b) \end{vmatrix} = C - \sigma \frac{C_o v}{D_b \delta} \qquad \text{(AIII-9)}$$

or finally:

$$C_{cylindrical}(a) = C - C_o \qquad \text{(AIII-10)}$$

which gives the value of constant μ as:

$$\mu = \frac{(C-C_o)}{\begin{vmatrix} I_o(\sigma a) & K_o(\sigma a) \\ I_o'(\sigma b) & K_o'(\sigma b) \end{vmatrix}} \qquad \text{(AIII-11)}$$

From the other boundary conditions that $D_\mu'(b) = 0$ we get

$$C'(b) = \lambda \begin{vmatrix} I_o(\sigma r) & K_o(\sigma r) \\ I_o(\sigma a) & K_o(\sigma a) \end{vmatrix} = 0 \qquad \text{(AIII-12)}$$

which results in $\lambda = 0$.

Hence, the solution for $C_{cylindrical}(r)$ is:

$$C_{cylindrical}(r) = (C-C_o) \frac{\begin{vmatrix} I_o(\sigma r) & K_o(\sigma r) \\ I_o'(\sigma b) & K_o'(\sigma b) \end{vmatrix}}{\begin{vmatrix} I_o(\sigma a) & K_o(\sigma a) \\ I_o'(\sigma b) & K_o'(\sigma b) \end{vmatrix}} \qquad \text{(AIII-13)}$$

Since

$$I_o'(\sigma r) = I_1(\sigma r)$$
$$K_o'(\sigma r) = -K_1(\sigma r)$$

we come to the solution of $C(r)$ as:

$$\frac{C(r)-C_o}{C_p-C_o} = \frac{[I_o(\sigma r)K_1(\sigma b)] + [I_1(\sigma b)K_o(\sigma r)]}{[I_o(\sigma a)K_1(\sigma b)] + [I_1(\sigma b)K_o(\sigma a)]} . \qquad \text{(AIII-14)}$$

However, for σ small, close to 0, K_1 becomes infinite so that a L'Hopital rule is applied giving the final result:

$$\frac{C(r)-C_o}{C_p-C_o} \approx \frac{I_o(\sigma r)}{I_o(\sigma a)} \approx \frac{1 + \frac{\sigma^2 r^2}{4}}{1 + \frac{\sigma^2 a^2}{4}} \approx 1 \qquad \text{(AIII-15)}$$

which gives the final convergence to unity.

REFERENCES

1. A. T. Davenport, F. G. Berry and R.W.K. Honeycombe: Met. Sci. J., 1968, vol. 2, p. 104.
2. J. M. Gray and R.B.S. Yeo: Trans. ASM, 1968, vol. 61, p. 255.
3. K. Campbell and R.W.K. Honeycombe: Met. Sci., 1974, vol. 8, p. 197.
4. F. G. Berry and R.W.K. Honeycombe: Met. Trans., 1970, vol. 1, p. 3279.
5. M. Mannerkoski: Acta Polytechn. Scand., 1964, Ch. 26.
6. R. W. K. Honeycombe: Met. Trans., 1976, vol. 78, p. 915.
7. C. J. Tillman and D. V. Edmonds: Metals Techn., 1974 vol. 1, p. 456.
8. T. J. Headley and J. H. Hren, Phil. Mag., 1976, vol. 34, p. 101.
9. E. Nes and J. Washburn, J. Appl. Phys., 1971, vol. 42, p. 3562.
10. N. Ryum, Acta. Met., 1969, vol. 17, p. 269.
11. O. Izumi and D. Oeschlägel, Scripta Met., 1969, vol. 3, p. 619.
12. E. Nes and N. Ryum, Scripta Met., 1971, vol. 5, p. 987.
13. M. Sundberg, R. Sundberg and B. Jacobson, Jernkont. Ann., 1971, vol. 155, p. 1.

14. J. M. Silcock and W. J. Tunstall: Phil. Mag., 1964, vol. 10, p. 361.

15. E. Nes Acta Met., 1974, vol. 22, p. 81.

16. H. Kreye and E. Hornbogen: J. Mat. Sci., 1970, vol. 5, p. 89.

17. V. A. Phillips: Trans. AIME., 1964, vol. 230, p. 967.

18. A. J. Davenport and R. W. Honeycombe, Proc. Roy. Soc., vol. 322, p. 191.

19. A. Barbacki and R.W. Honeycombe; Metallography, 1976, vol. 9, p. 277.

20. H. I. Aaronson: Decomposition of Austenite by Diffusional Processes, p. 387 ff., Interscience Publishers, New. York, 1962.

21. E. Hornbogen: Met. Trans., 1972, vol. 3, p. 2717.

22. K. N. Tu and D. Turnbull: Acta Met., 1967, vol. 15, p. 369.

23. H. I. Aaronson and H. B. Aaron: Met. Trans., 1972, vol. 3, p. 2743.

24. R. A. Fournelle and J. B. Clark: Met. Trans., 1972, vol. 3, p. 2757.

25. G. Meyrick: Scripta Met., 1976, vol. 10, p. 649.

26. N. Lange and G. R. Purdy (to be published in Met. Trans.).

27. M. Hillert: Decomposition of Austenite by Diffusional Processes, p. 107 ff., Interscience Publishers, New York, 1962.

28. B. E. Sundquist, Met. Trans., 1973, vol. 4, p. 1919.

29. G. R. Speich: Trans. TMS-AIME, 1968, vol. 242, p. 1359

30. J. B. Clark: Acta Met., 1978, vol. 16, p. 141.

31. D. Turnbull: Acta Met., 1955, vol. 3, p. 55.

32. J. W. Cahn: Acta Met., 1959, vol. 7, p. 18.

33. M. Hillert: The Mechanism of Phase Transformations in Crystalline Solids, p. 231, Monograph and Report Series No. 32, Inst. of Metals, 1969.

34. M. Hillert: "Lectures on the theory of phase transformation ed. H. I. Aaronson, chapter 1, p.1, American Institute of Mining, Metallurgical and Petroleum Engineers, Inc., New York, 1977.

35. J.M. Shapiro and J.S. Kirkaldy, Acta Met., 1968, vol. 16, p. 1239.

36. M. S. Sulonen: Acta Met., 1964, vol. 12, p. 749.

37. M. Hillert and R. Lagneborg: J. Mat. Sci., 1971, vol. 6,p.208.

38. A. H. Geisler: "Phase Transformations in Solids", eds. R. Smoluchowski, J. E. Mayer,and M. A. Weyd (John Wiley and Son, New York, 1951) p. 387.

39. C. S. Smith: Trans. ASM, 1953, vol. 45, p. 533.

40. M. Hillert: Met. Trans., 1975, vol. 6A, p. 5.

41. J. S. Kirkaldy: "Decomposition of Austenite by Diffusional Processes", p. 39 f.f., Interscience Publishers, New York, 1962.

42. J. M. Shapiro: Ph.D. Thesis, McMaster University, 1966.

43. M. Hillert: Met. Trans., 1972, vol. 3, p. 2729.

44. J. W. Cahn: Acta Met., 1960, vol. 8, p. 554.

45. M. Hillert and G. R. Purdy: Acta Met., 1978, vol. 26, p. 333.

46. K. C. Russell: Nucleation in Solids, 1975 (to appear in Nucleation III, ed. A. C. Zettlemoyer, Pub. by Marcel Dekker, New York).

47. G. Wulff, Z. Krystallog., 1901, vol. 24, p. 449.

48. C. Herring: Phys. Rev., 1951, vol. 82, p. 87.

49. D. W. Hoffman and J. W. Cahn: Surface Sci., 1972, vol. 31, p. 368.

50. J. W. Cahn and D. W. Hoffman: Acta Met., 1974, vol. 22, p. 1205.

51. K. C. Russell: Acta Met., 1969, vol. 17, p. 1123.

52. J. Feder, K. C. Russell, J. Lothe and G. M. Pound: Adv. Phys., 1966, vol. 15, p. 111.

53. K. C. Russell, Acta Met., 1968, vol. 16, p. 761.

54. R. B. Nicholson: "Phase Transformations", p. 269, ASM, Metals Park, Ohio, 1970.

55. K. C. Russell and H. I. Aaronson: J. Mat. Sci., 1975, vol. 10, p. 1991.

56. G. R. Purdy: Metallography, 1975, Vol. 7, p. 131.

57. C. Zener: AIME Trans., 1947, vol. 167, p. 550.

58. H. B. Aaron and H. I. Aaronson: Acta Met., 1968, vol. 16, p. 789.

59. A. D. Brailsford and H. I. Aaronson: J. Appl. Phys., 1969, vol. 40, p. 1702.

60. M. Hillert; Jernkontorets Ann., 1957, vol. 141, p. 757.

61. H. I. Aaronson, M. R. Plichta, G. W. Franti and K. C. Russell: Met. Trans. A, 1978, vol. 9A, p. 363.

62. M. McLean: Metal Sci., 1978, vol. 1, p. 113.

63. Lord Rayleigh: Proc. London Math. Soc., 1878, vol. 10, p. 4.

64. F. A. Nichols and W. W. Mullins: Trans. Metal. Soc. AIME, 1965, vol. 233, p. 1840.

65. H. E. Cline: Acta Met., 1971. vol. 19, p. 481.

66. F. A. Nichols and W. W. Mullins: J. Appl. Phys., 1965, vol. 36, p. 1826.

67. F. A. Nichols: J. Mat. Sci., 1976, vol. 11, p. 1077.

68. J. S. Servi and D. Turnbull: Acta Met., 1966, vol. 14, p. 161.

69. J. D. Livingston: Trans. AIME, 1959, vol. 215, p. 566.

70. J. J. Becker: Trans. AIME, 1957, vol. 209, p. 53.

71. W. Klement: Trans. AIME, 1963, vol. 227, p. 965.

72. M. Hansen: "Constitution of Binary Alloys", p. 469, McGraw Hill Book Co., New York, 1958.

73. V. A. Phillips and J. D. Livingston: Phil. Mag., 1962, vol. 7, p. 969.

74. M. F. Ashby and L. M. Brown: Phil. Mag., 1968, vol. 8, p. 1083.

75. M. F. Ashby and L. M. Brown: Phil. Mag., 1963, vol. 8, p. 1649.

76. V. A. Phillips: Acta Met., 1966, vol. 14, p. 271.

77. C. A. Mackliet: Phys. Rev. 1958, vol. 109(6), p. 1964.

78. D. B. Butrymowicz, J. R. Manning and M. E. Read: J. Phys. and Chem. Ref. Data, 1976, vol. 5 (7) p. 110.

79. C. S. Smith and L. Guttmann: Trans. AIME, 1953, vol. 197, p. 81.

80. J. A. Hugo and V. A. Phillips: J. Sci. Instrum., 1963, vol. 40, p. 202.

81. P. B. Hirsch, A. Howie, R. B. Nicholson, D. W. Pashley and M. J. Whelan: "Electron Microscopy of Thin Crystals", Butterworths, London (1967).

82. M. F. Ashby and J. Lewis: Proc. on 15th Sagamore Army Materials Research Conf., Aug. 22, 1967, New York, p. 385.

83. M. F. Ashby, J. Harper and J. Lewis: Trans. AIME, 1969, vol. 245, p. 413.

84. P. Feltham and G. J. Copley: Acta Met., 1958, vol. 6, p. 539.

85. P. Gordon: Trans. AIME, 1955, vol. 203, p . 1043.

86. B. F. Decker and D. Harker: Trans. AIME, 1950, vol. 188, p. 887.

87. D.B. Butrymowicz, J. R. Manning and M.E. Read: J. Phys. and Chem. Ref. Data,1976, vol. 5(1) p. 136.

88. V. Phillips: Trans. AIME, 1966, vol. 236, p. 1302.

89. J. D.Eshelby: Proc. Roy. Soc., 1957, vol. A241, p. 376.

90. J. S. Kirkaldy: Can. J. Phys., 1964, vol. 42, p. 1447.

91. K. Smidoda, W. Gottschalk and H. Gleiter: Acta Met., Vol. 26, 1978, p. 1833.